creative commons

COMMONS DEED

저작자표시-비영리-변경금지 2.0 대한민국

이용자는 아래의 조건을 따르는 경우에 한하여 자유롭게

- 이 저작물을 복제, 배포, 전송, 전시, 공연 및 방송할 수 있습니다.

다음과 같은 조건을 따라야 합니다:

저작자표시. 귀하는 원저작자를 표시하여야 합니다.

비영리. 귀하는 이 저작물을 영리 목적으로 이용할 수 없습니다.

변경금지. 귀하는 이 저작물을 개작, 변형 또는 가공할 수 없습니다.

- 귀하는, 이 저작물의 재이용이나 배포의 경우, 이 저작물에 적용된 이용허락조건을 명확하게 나타내어야 합니다.
- 저작권자로부터 별도의 허가를 받으면 이러한 조건들은 적용되지 않습니다.

저작권법에 따른 이용자의 권리는 위의 내용에 의하여 영향을 받지 않습니다.

이것은 이용허락규약(Legal Code)을 이해하기 쉽게 요약한 것입니다.

Disclaimer

dCollection

Ph.D. DISSERTATION

Efficient Beam-Hardening Correction Algorithm for Metal Artifact Reduction in Computed Tomography

CT 상의 금속 허상물 제거를 위한 효율적인 빔 경화 교정 알고리즘

Jin Hur

FEBRUARY 2021

DEPARTMENT OF ELECTRICAL ENGINEERING AND COMPUTER SCIENCE
COLLEGE OF ENGINEERING
SEOUL NATIONAL UNIVERSITY

Ph.D. DISSERTATION

Efficient Beam-Hardening Correction Algorithm for Metal Artifact Reduction in Computed Tomography

CT 상의 금속 허상물 제거를 위한 효율적인 빔 경화 교정 알고리즘

Jin Hur

FEBRUARY 2021

DEPARTMENT OF ELECTRICAL ENGINEERING AND COMPUTER SCIENCE
COLLEGE OF ENGINEERING
SEOUL NATIONAL UNIVERSITY

Efficient Beam-Hardening Correction Algorithm for Metal Artifact Reduction in Computed Tomography

CT 상의 금속 허상물 제거를 위한 효율적인 빔 경화 교정 알고리즘

지도교수 신 영 길

이 논문을 공학박사 학위논문으로 제출함

2020 년 11 월

서울대학교 대학원

전기 컴퓨터 공학부

허 진

허 진의 공학박사 학위논문을 인준함

2020 년 12 월

위 원 장	김 명 수
부위원장	신 영 길
위 원	서 진 욱
위 원	이 호
위 원	이 정 진

Abstract

Beam hardening in X-ray computed tomography (CT) is an inevitable problem due to the characteristics of CT system that uses polychromatic X-rays and energy-dependent attenuation coefficients of materials. It causes artifacts in CT images as the result of underestimation on the projection data, especially on metal regions. Metal artifact reduction is the process of reducing the artifacts in CT and restoring the actual information hidden by the artifacts. In order to obtain exact CT images for more accurate diagnosis and treatment planning on radiotherapy in clinical fields, it is essential to reduce metal artifacts. State-of-the-art approaches on effectively reducing metal artifact based on numerical methods by iterative reconstruction have been presented. However, it is difficult to be applied in clinical practice due to a heavy computational burden.

In this dissertation, we proposes an efficient beam-hardening estimation model and a metal artifact reduction method using this model to address this computational issue. The proposed model reflects the geometric information of metal objects and physical characteristics of beam hardening during the transmission of polychromatic X-ray through a material. Most of the associated parameters are numerically obtained from an initial uncorrected CT image and CT system without additional optimization. Only the unknown parameter related to beam-hardening artifact is fine-tuned by linear optimization, which is performed only in the reconstruction image domain. Two additional refinement methods are presented to reduce residual artifacts in the result image corrected by the proposed metal artifact reduction method.

The effectiveness of the proposed method was systematically assessed through qualitative and quantitative comparisons using numerical simulations and real data. The proposed algorithm showed significant results in the aspects of accuracy and robustness. Compared to existing methods, it showed improved image quality as well as fast execution time that is clinically applicable. This work may have significant implications in improving the accuracy of diagnosis and treatment planning for radiotheraphy through CT imaging.

Keywords: Metal artifact reduction, beam-hardening correction, CT reconstruction, polychromatic X-ray attenuation coefficient, ray transmission length
Student Number: 2011-20957

Contents

List of Figures

List of Tables

Chapter 1

Introduction

1.1 Background and motivation

X-ray computed tomography (CT) is the most widely and commonly used imaging method to plan treatment in radiotherapy [10]. Most patients receiving radiotherapy possess metal objects near the treatment area, resulting in prominent image artifacts that negatively affect the treatment planning by either causing difficulties to delineate the target volume or reducing the dose calculation accuracy. In current clinical protocols, filtered back projection (FBP) [11] is the most commonly used algorithm in CT reconstruction. The FBP algorithm assumes the X-ray source to be monochromatic to establish the Radon transform [12] between CT projection data and an attenuation coefficient distribution at a fixed energy level. However, CT scanners generally use polychromatic X-rays because of the limitations of actual implementations.

With the presence of high density materials (e.g. metal implants), artifacts

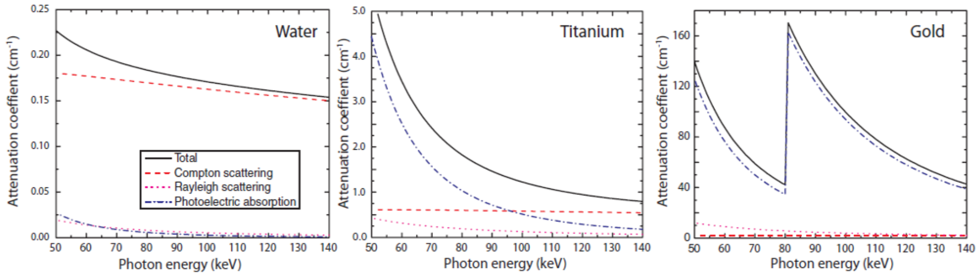

Figure 1.1 Attenuation coefficients of materials. Image courtesy of NIST XCOM database [1].

in CT image occurs due to the following factors: beam-hardening, scattering and noise [13, 14]. During the transmission of polychromatic X-rays through a material, low-energy photons are lost more than high-energy photons (Fig. 1.1). This physical phenomenon increases the mean energy of the X-rays, which is an effect called beam-hardening [15] (Fig. 1.2). As a result, the attenuation coefficient inside the material is reduced when the X-rays pass through. This reduction is more noticeable in high-density materials such as metals than in low-density materials such as soft tissues (Fig. 1.1). Thus, metallic materials create a substantial discrepancy in the Radon transform between the expected projection data and measured projection data. This characteristic is the dominant reason why metal artifacts have streaks and cupping shapes [13,16]. When beam hardening and other scattering effects are combined in the measurements, it leads to dark shadows especially in the CT image for directions where the most attenuation occurs [17].

Numerous metal artifact reduction (MAR) methods have been proposed to suppress such artifacts (Fig. 1.3) [18]. First, most methods categorized under sinogram completion are based on inpainting approaches to repair the metal

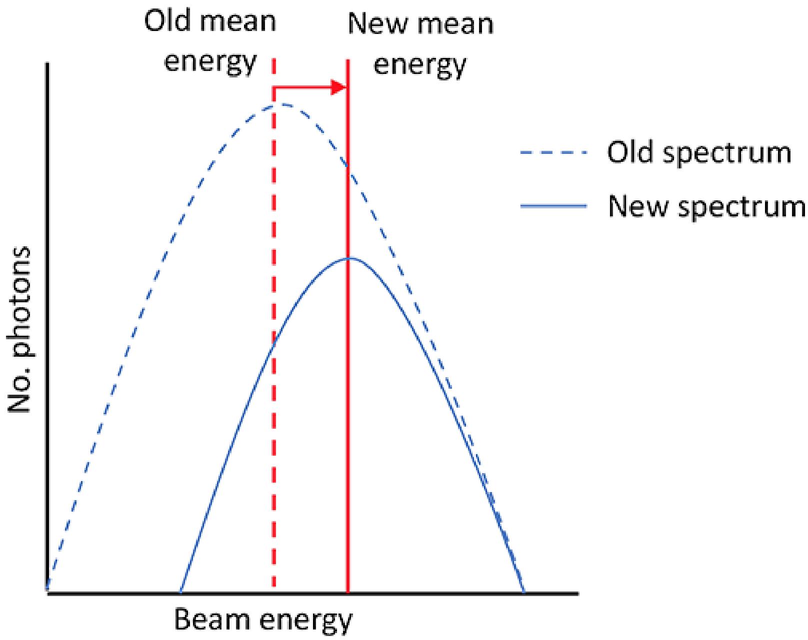

Figure 1.2 Illustration of beam-hardening.

projection part of the projection data using various interpolation and inpainting methods [5–7, 19–32]. Without consideration of X-ray transmission characteristics, inappropriate inpainting can lead to additional artifacts and deteriorate morphological information in regions surrounding the metal [5, 24, 33]. Second, iterative reconstruction methods repeatedly function to minimize the metal artifacts based on physically derived observation models [34–45]. The iterative algorithms use multiple iteration steps to approach the correct solution, consequently a better reconstruction is achieved with a longer calculation time. Third, dual-energy CT [46–50] considers CT reconstruction at different energy levels, which can yield more satisfactory results, but it requires a longer post-processing time and higher radiation dose than single-energy CT [48]. Fourth, several approaches based on deep learning technology have been re-

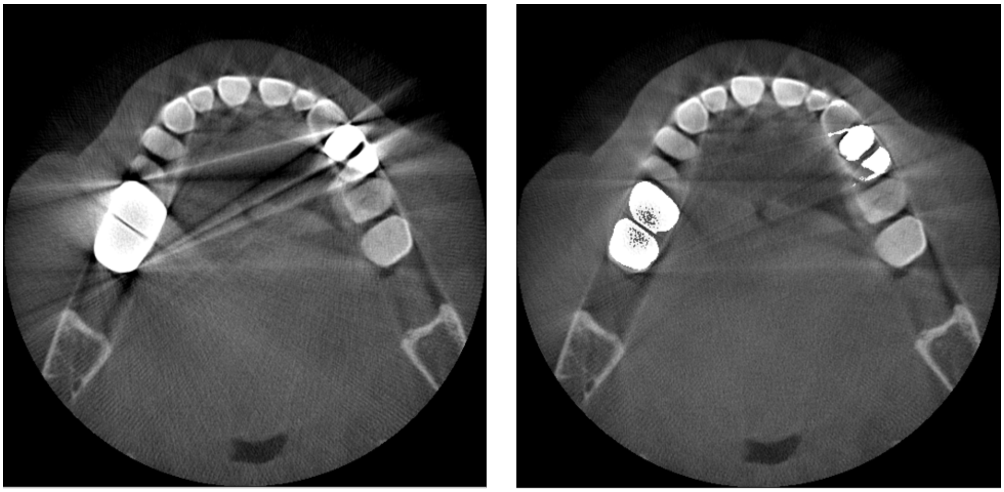

Figure 1.3 Dental CT images before and after performing metal artifact reduction.

ported [51–54]. The deep neural networks (DNN) based methods are supervised learning that requires paired data - one with artifacts and the other without artifacts. For the training data sets, CT images or sinograms are synthesized with simulated CT artifacts [55–57]. The synthesized data do not fully cover realistic artifacts due to the complexity of X-ray transmission, especially in cases of multiple metallic objects. From the need of unsupervised learning, generative adversarial networks (GANs) [58–60] have been recently researched to solve the MAR problem as unsupervised image-to-image translation [61–65]. However, the GAN-based MAR methods remain to be clear when the networks are trained with real CT images suffered from artifacts due to multiple metallic objects [66].

1.2 Scope and aim

Among the various research for MAR, there have been studies that metal artifacts can be effectively reduced via a mathematical correction of the beam-hardening factors [8,9,67–71]. Park et al. [8] proposed a beam-hardening corrector (BCMAR) based on the analysis of the geometric characteristics of beam-hardening artifacts. Shi et al. [9] proposed a synthetical geometry projection that uses a feature of attenuation properties of metals with similar shapes but different sizes. The tremendous computational cost due to the iterative reconstruction structure hampers the practical application of these methods although both studies showed effective results for beam-hardening reduction. To the best of our knowledge, there has been no sinogram-correction based approach for practical usage in the clinical field.

Our work focuses on developing a novel MAR method based on an efficient beam-hardening correction for getting closer to clinical usage of the correction-based MAR. The conventional approach to beam-hardening correction is to apply a water beam-hardening correction. This approach compensates for the beam-hardening effects in water and soft tissues, but it is insufficient for metals because the energy dependence of attenuation in metals is very different from that in water. The energy dependence of attenuation needs to be additionally considered for metals.

1.3 Main contribution

The major contribution of this study is that we propose a constrained beam-hardening estimator (CBHE) that represents the underestimated error between the expected and calculated reconstruction images, and it needs no iterative reconstruction to be calculated. The proposed estimator is derived from a polychromatic X-ray attenuation model with respect to the X-ray transmission length, avoiding dependencies on the X-ray spectrum and material attenuation coefficients. It maximizes the accuracy of correction of beam-hardening artifacts by analyzing the change in the attenuation coefficient level while polychromatic X-rays pass through a homogeneous metallic material.

The entire process (Fig. 1.4) is completed by a linear combination of two images reconstructed only once, leading to faster computation. The estimator-associated parameters are numerically calculated from an uncorrected CT image and metal-only forward projection. The only unknown parameter to minimize the beam-hardening artifact is fine-tuned by solving linear optimization on the reconstruction image domain without forward and backward projection transformations. The effectiveness of this method is comparable to that of other beam-hardening correction methods in terms of the optimization speed and MAR quality.

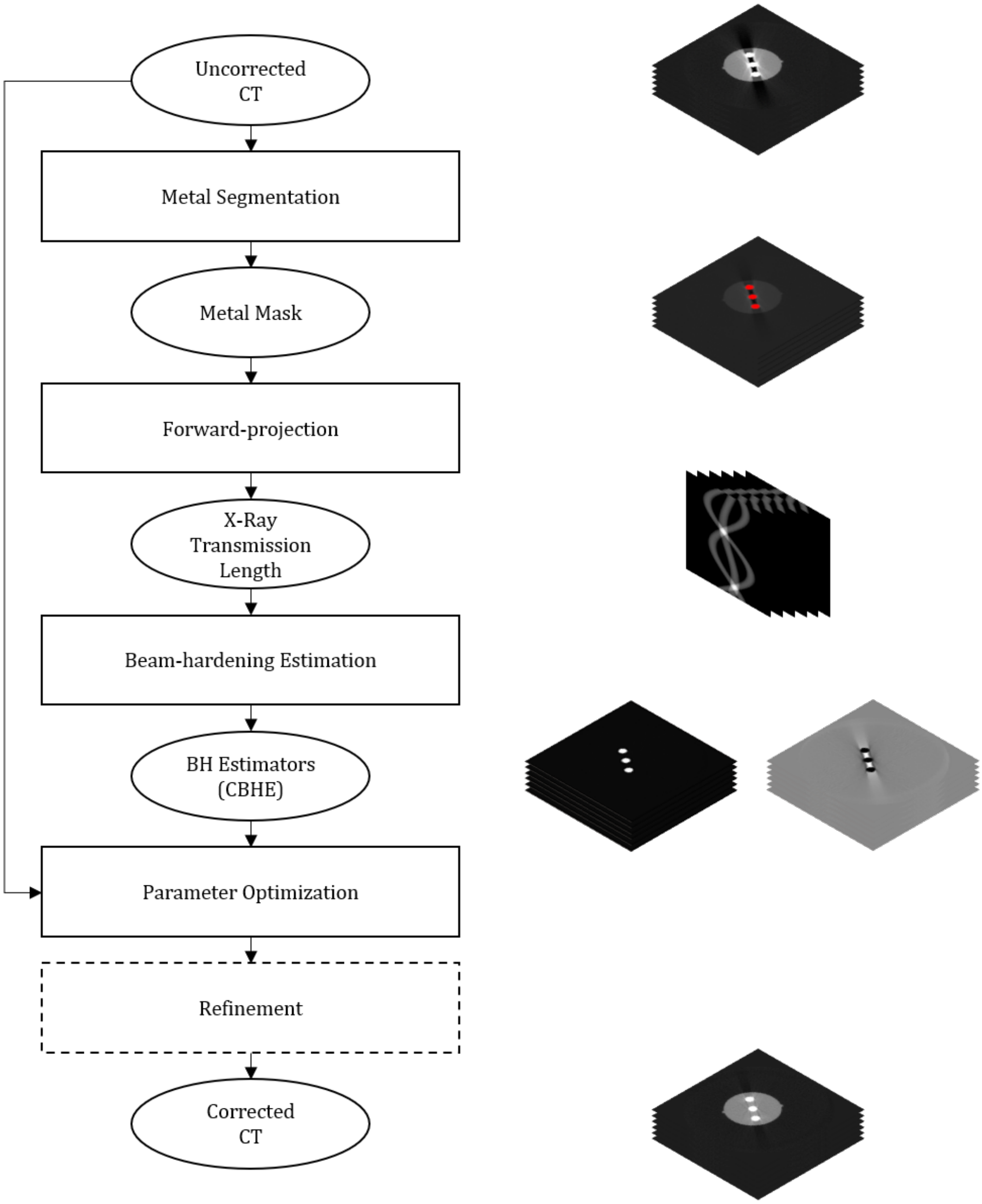

Figure 1.4 Process of the proposed MAR method

1.4 Contents organization

The remainder of this dissertation is organized as follows: Chapter 2 presents a brief background of CT reconstruction, CT artifacts, and metal artifact reduction methods; Chapter 3 describes the proposed constrained beam-hardening estimator from analysis of the characteristics of polychromatic X-ray; The entire process of the proposed MAR method is illustrated in Chapter 4; And chapter 5 shows the experimental results of verification and evaluation of the proposed method compared to other MAR methods; Finally, we summarize and conclude this dissertation in Chapter 6.

Chapter 2

Related Works

The causes of metal artifacts are greatly related to the principles of the CT system. CT artifacts arise from inconsistencies between properties of X-ray which is the core of CT device and CT reconstruction algorithm. This chapter briefly introduces principles of CT and MAR. We explain physical characteristics of CT in Section 2.1 and examine CT artifacts according to their causes in Section 2.2. The previous approaches to reduce metal artifacts are analyzed from purposes to limitations in Section 2.3.

2.1 CT physics

We explain CT reconstruction to understand the metal artifact deeply in this section. From the fundamentals of X-ray and the algorithm of CT reconstruction, we infer the reasons why metal artifact occurs.

2.1.1 Fundamentals of X-ray

X-ray is electromagnetic waveform just like microwaves, infrared, visible light, ultraviolet, and radio waves. The X-ray has the wavelength that ranges from a few picometers to a few nanometers [2]. X-ray photons are produced when high-speed electrons bombard a substance. The following three types of interactions are involved in the production of X-ray photon. The first type of interaction is that an electron has loss of radiation when it comes close to a nucleus of an atom ((a) in Fig. 2.1). Bremsstrahlung radiation is generated when the electric field of the nucleus decelerates a high-speed electron. The second type of interaction happens when one of the electrons of the atom is hit and ejected by a high-speed electron ((b) in Fig. 2.1). An electron in outer-shell of the atom fills in the vacant shell and it emits characteristic X-ray. The last type of interaction is that an electron hit a nucleus directly and its total energy is transformed to bremsstrahlung ((c) in Fig. 2.1).

For medical CT, typical X-ray spectrum generated is approximately between 20 keV and 140 keV. In this spectrum, there are three ways of how X-ray interacts with substances: photoelectric effect, Compton effect, and coherent scattering. The photoelectric effect appears when an energy of a X-ray photon is higher than an energy that binds an electron, and the incident photon hands over its whole energy to free the electron in the deep shell of the atom. The Compton effect is that an incident photon of X-ray hits an electron and liberates the electron from the atom. Unlike the photoelectric effect, the incident X-ray photon is scattered or deflected with partial loss of the initial energy. The last way in which X-ray interacts with substances is the coherent scattering (or known as Rayleigh scattering). It is least important to researchers in clinical CT

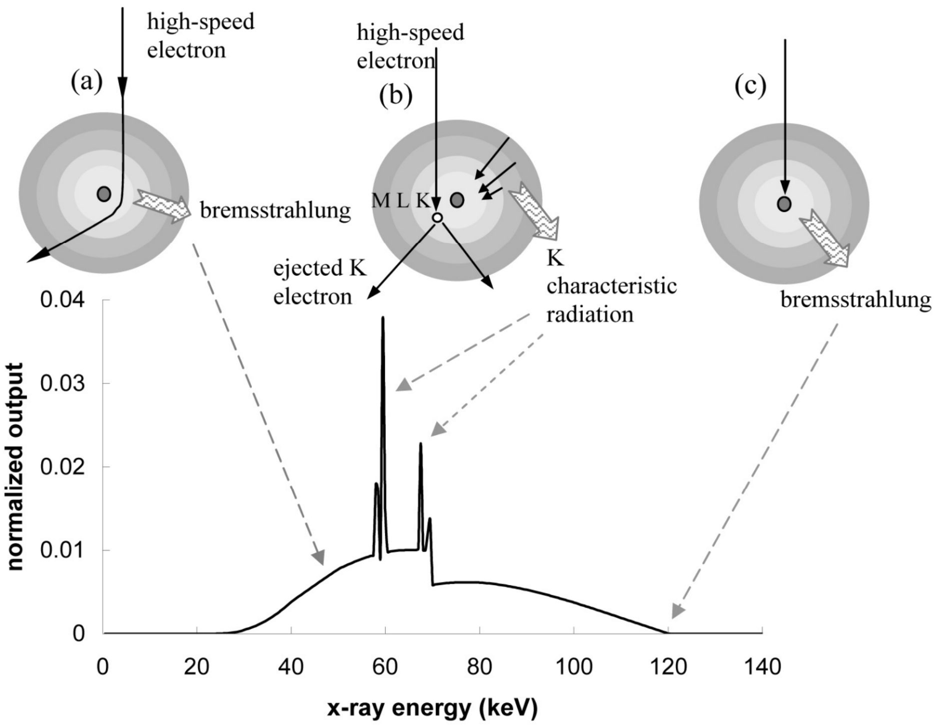

Figure 2.1 Illustration of electron interaction with a target and its relationship to the x-ray tube energy spectrum. Image courtesy of J. Hsieh [2].

since an energy of a photon is not converted into kinetic energy and no ionization occurs. The process is same as what happens in transmitter of radio station. Electrons in an atom is set into momentary vibration by an electromagnetic wave with an oscillating electric field. The oscillating electrons emit a radiation with the same wavelength of the electromagnetic wave. The interaction is called coherent scattering because of the cooperative phenomenon.

These interactions (photoelectric effect, Compton effect, and coherent scattering) has a net effect that some of X-ray photons are scattered or absorbed. In other words, photons of a X-ray are attenuated as the X-ray penetrates a

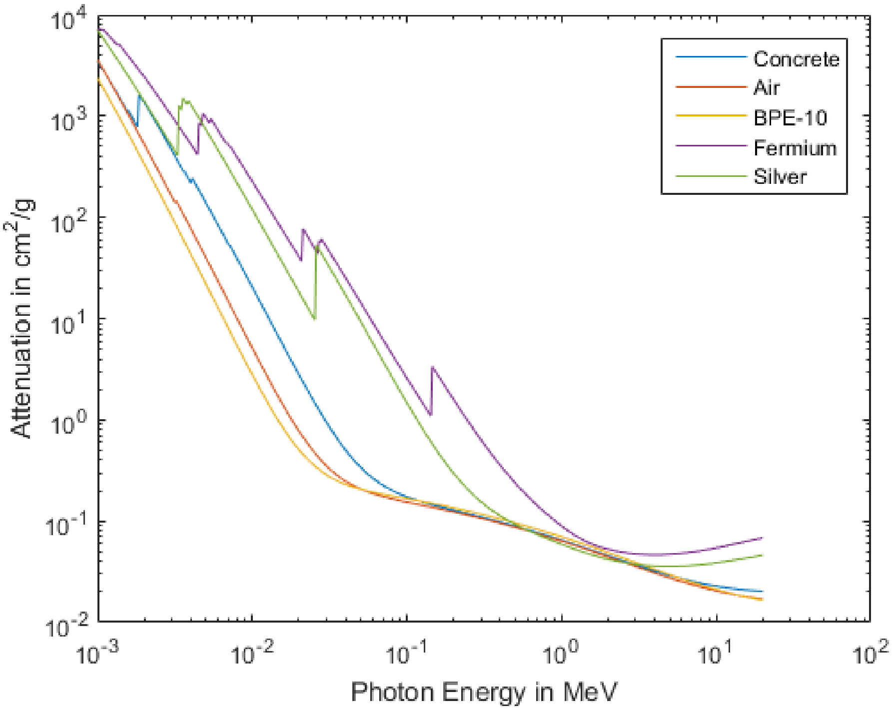

Figure 2.2 Linear attenuation coefficients for different materials. The data of attenuation coefficients is obtained from NIST [3].

substance. The attenuation is expressed as an exponential relationship to a monoenergetic (monochromatic) X-ray and a substance of a uniform density:

$$I = I_0 \times e^{-(\tau+\sigma+\sigma_r)L}, \tag{2.1}$$

where I is the incident X-ray intensity; I_0 is the transmitted X-ray intensity; L is the thickness of the substance; and τ, σ and σ_r are the attenuation coefficients of the photoelectric, Compton, and coherent scattering interactions of the substance respectively. (2.1) is simplified as

$$I = I_0 \times e^{-\mu L}. \tag{2.2}$$

where μ is the linear attenuation coefficient of the substance, and this equation is called the Beer-Lambert law. Clearly, μ is a function of an incident X-ray photon energy (Fig. 2.2).

2.1.2 CT reconstruction algorithms

Analytical reconstruction algorithm

The filtered back-projection (FBP) is one of the most widely used analytical reconstruction algorithms [2, 10]. The formula of the FBP algorithm is a combination of filtering and back-projection operators. Before getting to know the FBP, we shall know the theory that governs tomographic reconstruction, which is known as Fourier slice theorem (also known as the central slice theorem). For the ease of explanation in the following, $f(x, y)$ denotes a object being reconstructed, and $p(t, \theta)$ denotes a parallel projection of $f(x, y)$ taken at angle θ (Fig. 2.3). The Fourier slice theorem is that a Fourier transform of a parallel projection of $f(x, y)$ obtained at angle θ equals a line in a 2D Fourier transform of $f(x, y)$ taken at the same angle [2]. With the Fourier slice theorem, a Fourier transform of a projection is a sampled line in a 2D Fourier transform of $f(x, y)$. If sufficient projections with the range from 0 to π are achieved, the Fourier space grid of the object can be filled fully. $f(x, y)$ can be reconstructed by the inverse Fourier transform of the grid.

Although the Fourier slice theorem gives a direct solution for tomographic reconstruction, it contains some challenges to implement actually. The most important one of the challenges is that the pattern of sampling in the Fourier space is not Cartesian. By the Fourier slice theorem, it is stated that a Fourier transformed projection is a sampled line segment passing through the origin in

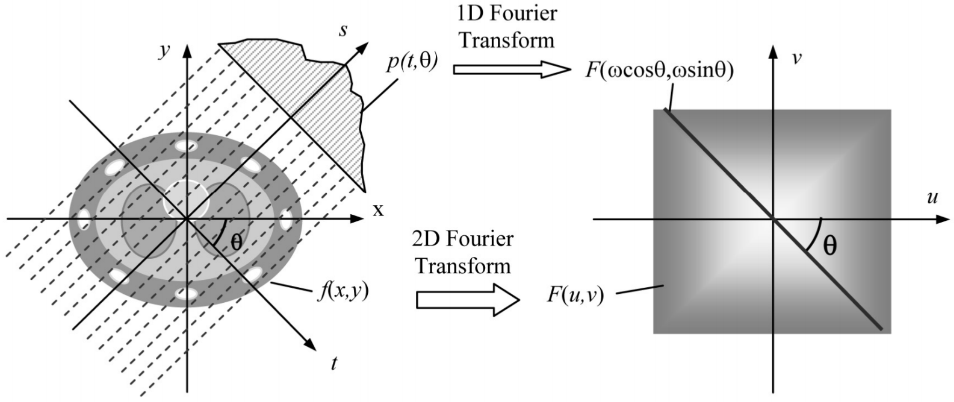

Figure 2.3 Illustration of the Fourier slice theorem. Image courtesy of J. Hsieh [2].

2D Fourier space. Samples from projections fall on positions in Polar coordinate grid (Fig. 2.4). To perform a 2D inverse Fourier transform, these values must be interpolated to a Cartesian coordinate grid. Interpolation in frequency domain is not as straightforward as interpolation in the spatial domain. In the spatial domain, an interpolation error is localized to the small region where the pixel is located. However, this property does not apply to interpolation in the frequency domain since each sample in 2D Fourier space represents a specific spatial frequency (horizontal and vertical directions). An error generated from a single sample in Fourier space affects the shape of the entire image (after inverse Fourier transform).

It is advisable to explore an alternative implementation of the Fourier slice theorem, and the most widely used implementation is the FBP algorithm. We start with the obvious fact that relationship between Fourier transform and inverse Fourier transform is conjugate. The image f(x,y) can be achieved from

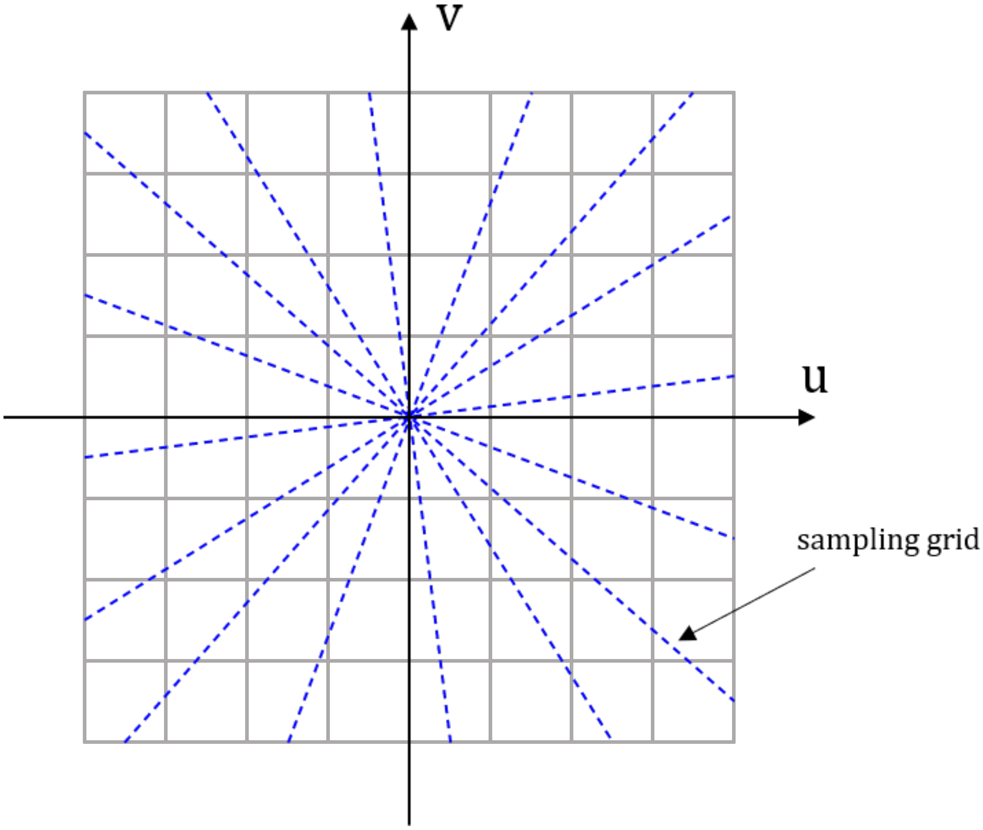

Figure 2.4 Sampling pattern in Fourier space based on the Fourier slice theorem.

its Fourier transform F(u, v) by performing the inverse Fourier transform:

$$f(x,y) = \int_{-\infty}^{\infty}\int_{-\infty}^{\infty} F(u,v)e^{j2\pi(ux+vy)}dudv. \tag{2.3}$$

From (2.3), we can obtain the following relationship [2]:

$$f(x,y) = \int_{0}^{\pi}\int_{-\infty}^{\infty} P(\omega,\theta)|\omega|e^{j2\pi\omega t}d\omega d\theta. \tag{2.4}$$

$P(\omega,\theta)$ is the Fourier transform of the projection at angle θ and the inside integral term is the inverse Fourier transform of the $P(\omega,\theta)|\omega|$. In the real space, it represents a projection filtered by a function whose response is $|\omega|$ in Fourier space.

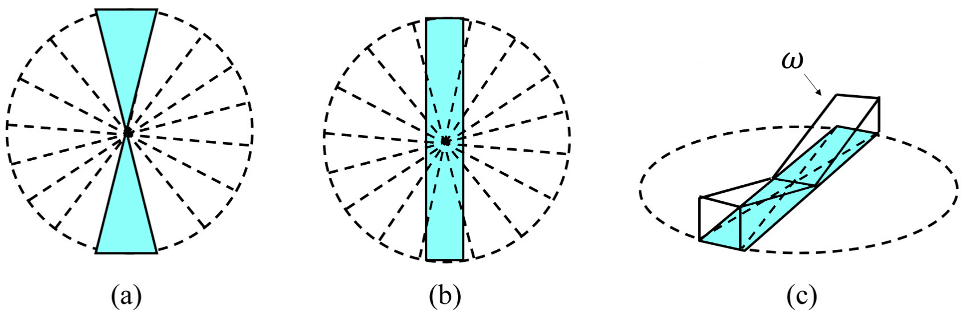

Figure 2.5 Illustration of the filtered back-projection concept.

The meaning of the FBP approach can be easily explained based on the Fourier slice theorem. Ideally, if we assume that a Fourier transform of a projection is shaped as a sliced pie (shown in Fig. 2.5 (a)), we can put each fan slice into its proper position to get a 2D Fourier transform of the object without difficulties. Unfortunately, in frequency domain, a Fourier transform of each projection is shaped as a plate (shown in Fig. 2.5 (b)). If we accumulate the Fourier transform of each projection that are uniformly spaced over 2π, the center region is intensively overvalued and the outer regions are undervalued. To approximate the pie-shaped region with the plate-shaped regions, we can perform filtering to the plate-shaped Fourier transform with a function that has a lower value near the center and a higher value near the both ends (shown in Fig. 2.5 (c)).

Iterative reconstruction algorithm

Despite its simplicity and fast performance, the CT system developed using the FBP algorithm is less realistic. To overcome the drawback of the analytical solution, a technique called iterative reconstruction (IR) is used [72]. To explain IR simply, our target will be limited to a 2D object and its projections (it can be easily extended to 3D). A 2D vector f denotes the scanned object and p denotes its projections. A relationship between the object f and its projections p is established by the following:

$$p = Af + e, \tag{2.5}$$

where A is a system matrix and e is an error vector.

For an object and its projections in ideal cases, e should be zero and A's elements contain only the contribution of a specific object pixel to a specific projection. For real cases, A may be determined with the system geometry, detector response, shape of focal spot, and lots of other physical factors of the CT system. The error e contains any bias of measurement and additional noise. The iterative reconstruction is used to estimate f with a given p, and is formulated in the Bayesian structure of maximizing the posterior probability $Pr(f|p)$:

$$\hat{f} = argmax_f \Big(Pr(f|p) \Big), \tag{2.6}$$

where $\hat{f}$ is the optimal estimation of f based on p. With the Bayes rule, $Pr(f|p)$ can be expressed as:

$$Pr(f|p) = \frac{Pr(p|f)Pr(f)}{Pr(p)}, \tag{2.7}$$

Without a priori information for the measure projection, (2.6) is equivalent to

$$\hat{f} = argmax_f \Big(log(Pr(p|f)) + log(Pr(f)) \Big). \tag{2.8}$$

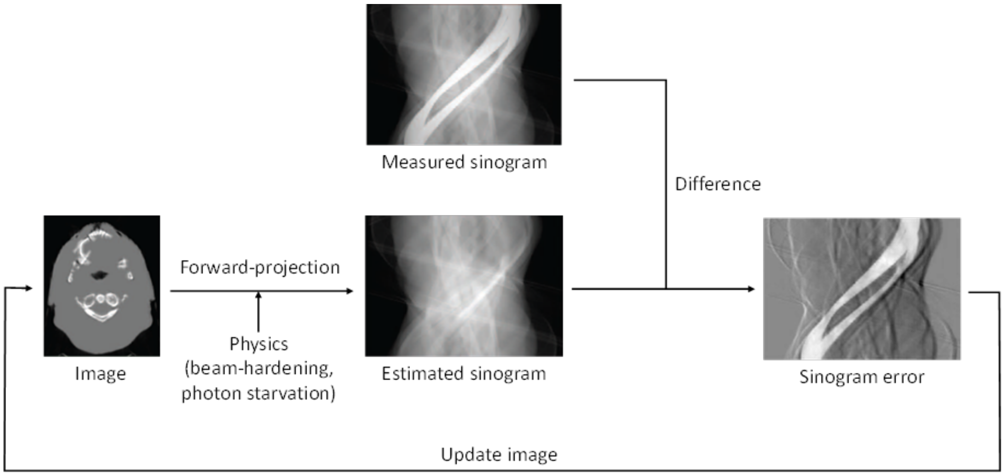

Figure 2.6 General process of the iterative reconstruction.

The optimization process begins by maximizing the first term of (2.8). The estimation of f is an iterative process to converge to $\hat{f}$. For a particular angle, the estimated projection is obtained with forward projection on the estimated image. The estimated projection is then compared to the actual measurement p, and the estimation f' is refined by using the difference. The entire procedure is repeated until certain criteria is satisfied. The iterative process is illustrated by Fig. 2.6 and this iterative algorithm is called as the algebraic reconstruction technique (ART).

2.2 CT artifacts

In computed tomography (CT), the artifact indicates any systematic discrepancy between the ideal attenuation coefficients of the object and the CT values in the reconstructed image. CT images are inherently more susceptible to artifacts than conventional radiographs. The reason is that the image is reconstructed from about a million independent detector measurements. Reconstruction techniques assume that all the measurements are consistent, so errors in the measurements are usually reflected as errors in the reconstructed image.

2.2.1 Physics-based artifacts

Beam-hardening

A polychromatic X-ray consists of independent photons with an energy spectrum. As the X-ray passes through a substance, it becomes beam-hardened, that is to say its mean energy goes up because the lower energy photons are absorbed more fast than the higher-energy photons. Several types of artifact can result from this effect: cupping artifacts in an homogeneous material, dark shadows or streaks between dense substances in the reconstructed CT image.

Cupping artifacts

X-rays passing through the middle part of a uniform object are harder than X-rays passing through the edges of the object because they pass through more. As the X-ray gets harder, the attenuation rate decreases, so the X-ray gets stronger when it reaches the detector than when the X-ray had not been hardened. The result of attenuation profile differs from the ideal profile that is obtained with no beam-hardening. A profile of the CT values through the object displays a cupped shape.

Streaks and dark shadows

In a heterogeneous cross section, dark shadows or streaks may occur between two dense objects (e.g. bone, metal) in the CT image. They appear because the portion of the X-ray passing through one of the objects at a certain angle is less hardened than passing several objects at other angle.

Photon starvation

A potential cause of severe streak artifacts is photon starvation, which can happen in highly attenuating regions. When the X-ray is transmitted horizontally, the largest attenuation occurs and insufficient photons reach the detector. As a result, very noisy projections are measured at these angles. The reconstruction process has the effect of greatly scaling the noise up, resulting in horizontal streaks in the CT image. Increasing the tube current during the scan overcomes the problem of photon starvation, but the patient receives an unnecessary dose as the X-ray passes through less attenuating regions. Clinically, there are two solutions: adaptive filtering and tube current (mA) modulation. First, the regions in which the attenuation exceeds a specified level are smoothed before undergoing backprojection. Second, the tube mA can be varied with the gantry rotation.

Partial volume effect

Partial volume effect is due to the fact that highly dense structures (e.g. bones) are only partially included in the slice, resulting in high contrast errors. Such artifacts are prevented from occurrence by selecting a thinner slice since high contrast structures are less frequently partially included. However, this inherently increases the noise level, degrading contrast resolution.

2.2.2 Patient-based artifacts

Metal artifact

The metal produces a beam-hardening and photon starvation artifact. This can also happen with other high attenuation materials such as iodinated contrast. Metal artifact reduction algorithm minimizes these artifacts in conjuction with analytical reconstruction or iterative reconstruction. Megavoltage CT imaging can be considered, but it has a low contrast compared to kilovoltage CT imaging.

Patient motion

If a patient or structure moves even a little as the gantry rotates, the object will be detected as being in several positions and represented in the image, such as patient swallowing, breathing, pulsatility of heart and vessels, and patient movement. Clinical solution is to adjust scan parameters to shorten scan time. The other considerations are to use a breath hold immobilization tool, lead to comfortable patient position, and tell patient to stay.

Helical artifact

The gantry is moving in the z-axis as it rotates. Any object that changes in position or size along the z-axis has possibility to be distorted as they will be in different positions for different projections. This artifact is rare as scanners have a large number of detectors and pitch is less than 1.

2.3 Metal artifact reduction

In this section, we review previous works on metal artifact reduction. Sinogram means a pile of projections along the scanned angle axis. The projections can be varied from 1-dimensional images to 2-dimensional images depending on the CT system - fan-beam CT (FBCT) or cone-beam CT (CBCT). Fig. 2.7 shows the differences on the image acquisition between fan-beam CT and cone-beam CT. In most cases, sinogram means a set of projections only, not a shape of it (2D or 3D).

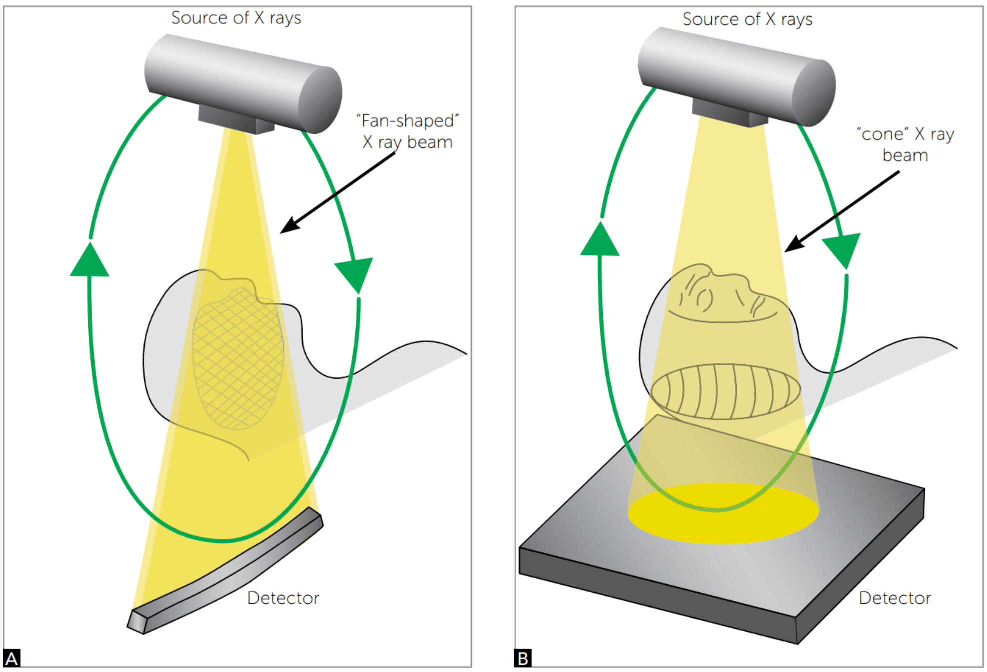

Figure 2.7 Illustration of differences on the scanning between fan-beam CT (A) and cone-beam CT (B). Image courtesy of Silva et al. [4].

The general process of MAR can be explained by Fig. 2.8. At first, a sino-

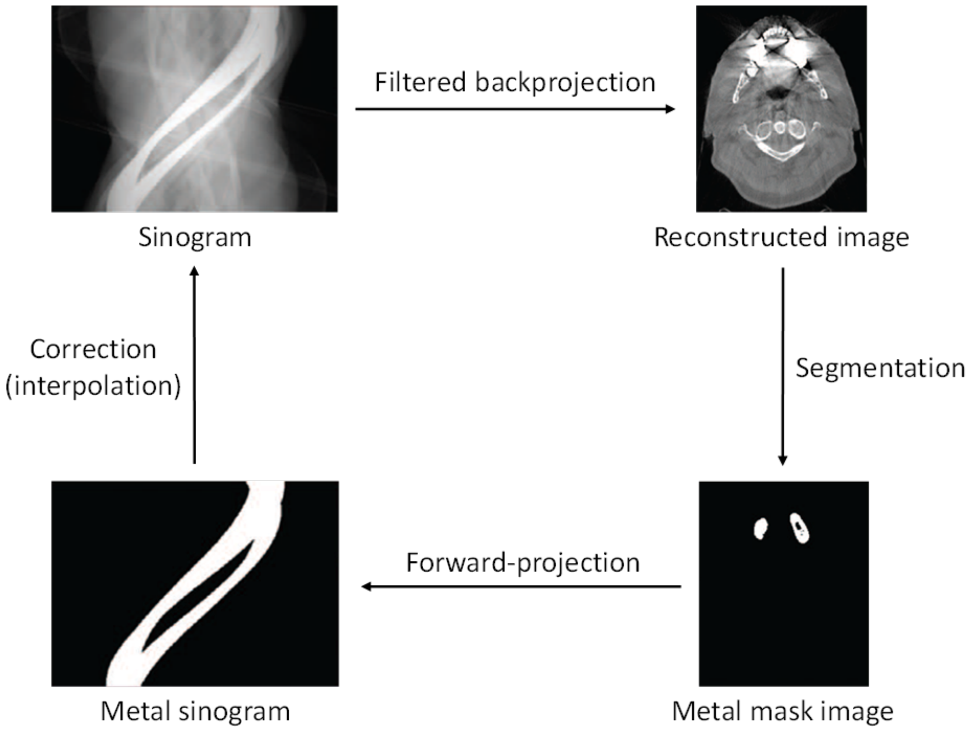

Figure 2.8 General process of metal artifact reduction.

gram is obtained from CT scanner and used to reconstruct CT image by using FBP (Feldkamp et al. [73] is mostly used). On the reconstructed CT image, metal object region is obtained by several segmentation methods. The metal region on the sinogram is obtained by using forward-projection with the same geometry of the ST scanner. After additional processes are conducted in the metal region and FBP is performed again, a metal artifact reduced image is obtained. This entire process can be iterated until it obtains a satisfied result.

Depending on what kind of processing is conducted in the metal region, MAR is classified into the following categories:

- Sinogram-completion based MAR

- Iterative reconstruction based MAR

- Deep-learning based MAR

The next subsections explain main concept of these categories and show representative research.

2.3.1 Sinogram-completion based MAR

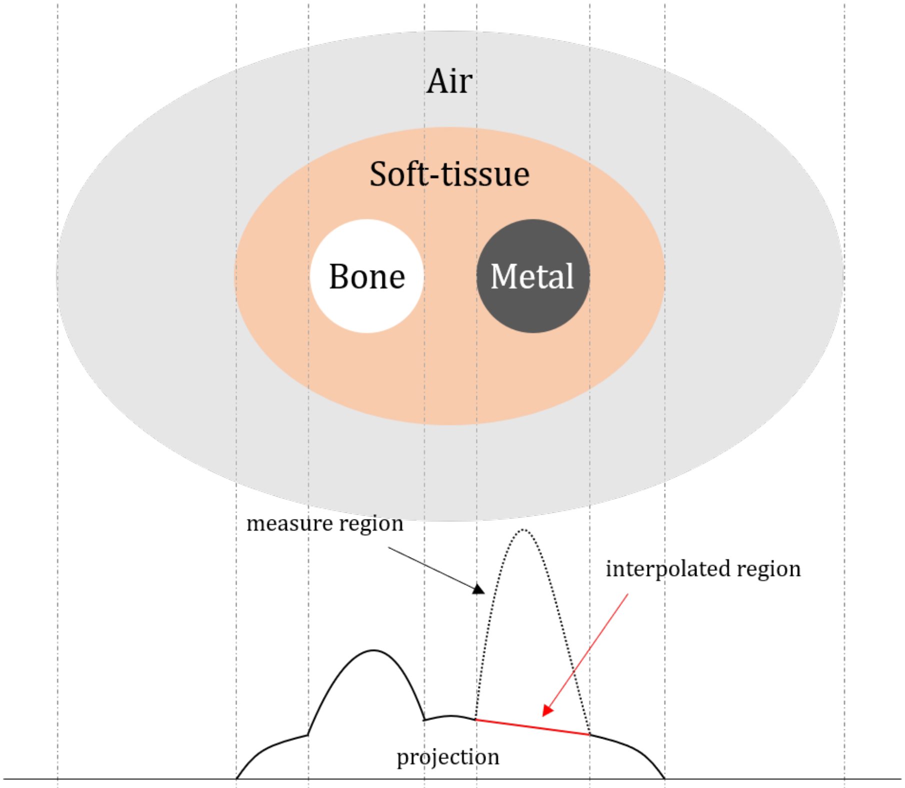

Figure 2.9 Schematic drawing of linear interpolation on projection.

The sinogram-completion based methods are based on regarding metal regions on projection data as missing or corrupted data. These methods have focused on estimating proper values for the metal region practically. The first study to guide these methodologies was Kalender et al. [20]. In this paper, the main idea was to replace metal regions with surrounding information (Fig. 2.9). To fill inside the metal region, linear interpolation was used with both end values of the metal region in each projection. This paper was also the first paper which introduced a *interpolation-based MAR* method. This method guarantees fastness and robustness if segmentation of metal region is well conducted. After this paper, several approaches based on interpolation schemes have been proposed.

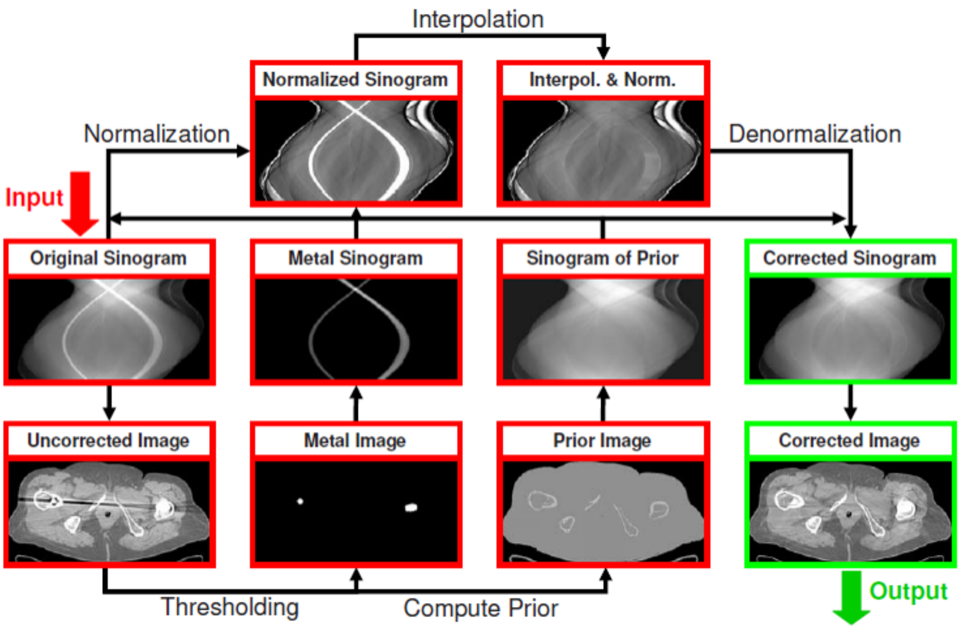

Figure 2.10 The entire process of normalized MAR. Image courtesy of Meyer et al. [5].

There were researchers who thought that naive-interpolation had a problem that all edge information lying on the X-ray passing through metal objects was lost. So they proposed with the primary objective of better preserving edge and contrast information, and thereby reducing secondary artifacts in final result [5, 24, 33]. Meyer et al. [5] proposed to use a prior image as a structural information preserver. Main contribution of this study was *normalization by prior image* to preserve structural information of entire object (Fig. 2.10).

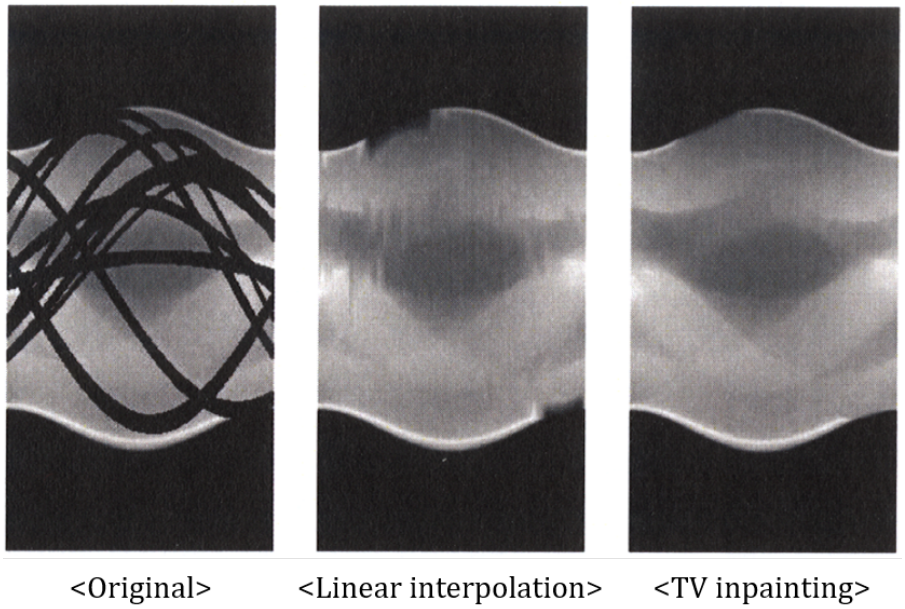

Figure 2.11 Total variation inpainting. Image courtesy of Duan et al. [6]

While the interpolation-based techniques have been used as common, image inpainting techniques also have been successfully implemented. Duan et al. [6] employed *total variation inpainting*, which is the well-known image restoration method [74]. It had some conditions to use, nevertheless it showed better quality on completion compared to interpolation based methods (Fig. 2.11).

Li et al. [7] combined *nonlocal inpainting* and the linear interpolation.

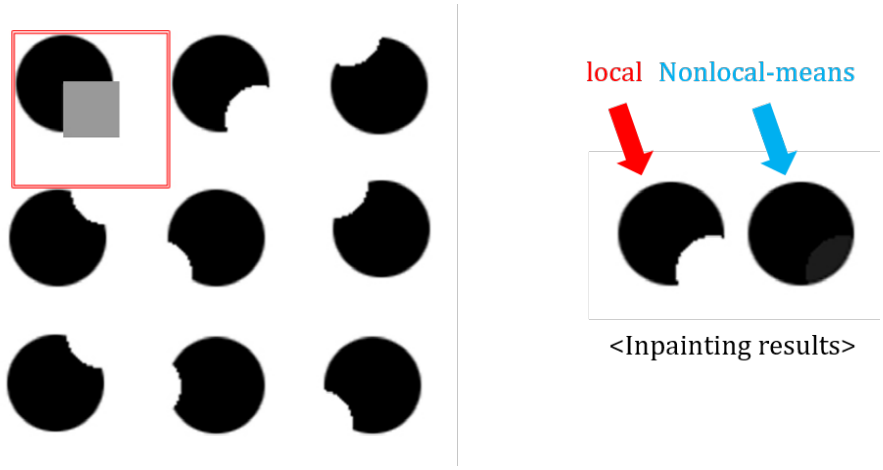

Figure 2.12 Illustration of nonlocal-means inpainting. Image courtesy of Li et al. [7]

Nonlocal-means techniques was a way to use global information on completing region. Fig. 2.12 shows the main concept of nonlocal-means techniques - local means vs. nonlocal means.

2.3.2 Sinogram-correction based MAR

Unlike the sinogram-completion based methods, the model-based methods compute the error on sinogram and correct it based on the mathematical analysis of characteristics of the X-ray. These methods are based on iterative reconstruction structure and therefore show relatively slow, but more effective results. Hsieh et al. [67] proposed a polynomial error model with some assumptions. The error model was approximated by a relatively simple form and it reduced the computational complexity of error estimation from the others at that time. With a well designed phantom, it showed the robustness and effectiveness in the case that various metal objects were inside together. In the first iteration, artifacts around low metal were reduced but artifacts around high metal still remained. After the second iteration, it showed that these artifacts also reduced more. The paper demonstrated that two iterations were typically sufficient to deal with a very wide range of densities.

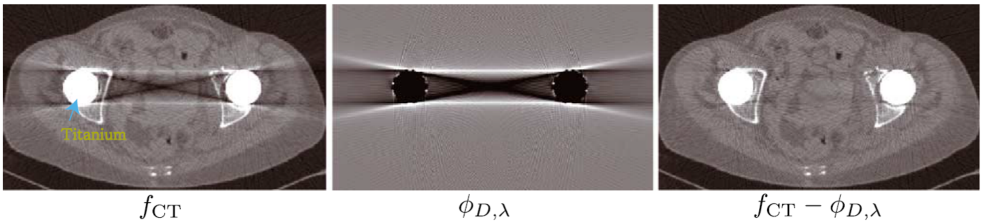

Figure 2.13 Metal artifact reduction based on a beam-hardening corrector (BC-MAR). Image courtesy of Park et al. [8].

In 2016, Park et al. [8] proposed a beam-hardening corrector that reflected the characteristics of beam-hardening well. Fig. 2.13 shows the the proposed corrector presents the artifacts in CT satisfactorily. They proved its performance with numerical simulations and phantom experiments. However, with the presence of several high density metals, the metal regions in sinogram are often severely corrupted and the performance of the method is limited.

Another recent study has a characteristic perspective. Shi et al. [9] analyzed the variation of attenuation coefficient of several materials on energy level and discovered that these attenuation coefficients showed similar shape of variation with only scale difference (Fig. 2.14). From this point, they proposed a synthetical geometry projection that combined each material in the projection with an scaled material.

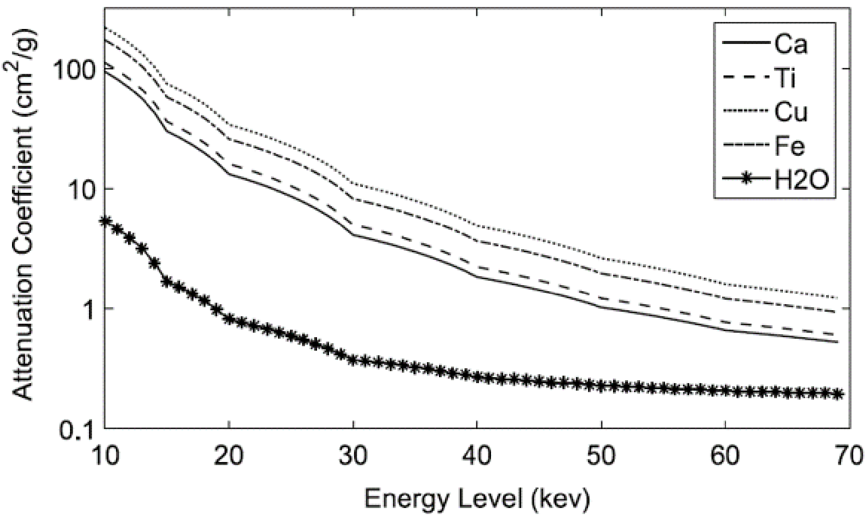

Figure 2.14 Illustration of variations of attenuation coefficients. Image courtesy of Shi et al. [9].

2.3.3 Deep-learning based MAR

Deep learning has been studied to have great successes in image processing and pattern recognition. Deep neural networks (DNNs) have been applied to achieve artifact-reduced medical images for low-dose CT. Park et al. [75] applied a U-net [76] to correct errors due to beam-hardening in the projection domain. Gjesteby et al. [52,77] employed convolutional neural networks (CNNs) to refine the result of NMAR for achieving fine correction in CT image regions by learning in the projection and image domain respectively. While the experiments showed that NMAR can be effectively improved further by CNN, there are still considerable artifacts remaining.

All the DNN-based methodologies needs to be trained by supervised learning that requires a pair of anatomically identical CT image pairs with and without metal artifacts. Since acquiring these image pairs is clinically impractical, most supervised methods rely on synthesized CT image with metal artifacts. However, the real artifacts may not be regenerated accurately by the synthesized artifacts because of the complexity of physical phenomena during X-ray transmission.

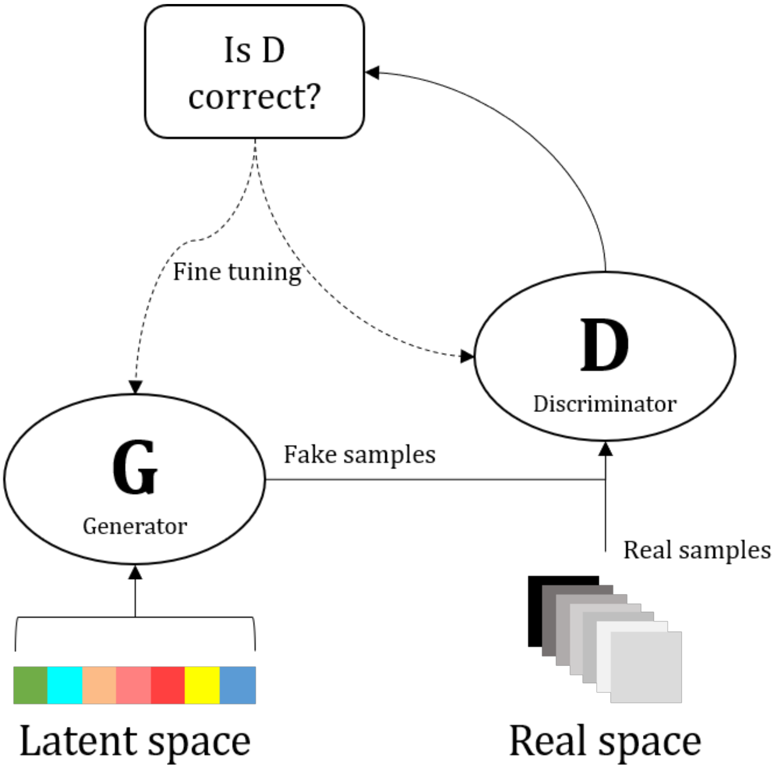

Figure 2.15 Illustration of generative adversarial network (GAN).

Recently, adversarial training [58] (Fig. 2.15) which is an superb strategy to train neural networks has been studied extensively as a new way for image-to-image translation. The application of GAN to metal artifact reduction has technical difficulties that a variety of low-quality images affected by severe metal artifacts are present in clinical CT images. Image correction in MAR should focus on corrupted regions and recover the hidden features by metal artifact, while preserving the other regions with the native anatomical structures of the patients. However, these GAN-based methods tend to degrade on unaffected regions by metal artifact as the training data hardly cover the various artifacts patterns.

Isola et al. [78] suggest a conditional GAN (CGAN) that has shown generalizability in various problems of image processing but is relatively new yet to CT problems [79]. The proposed CGAN is composed of two networks: a generator network for performing image-to-image translation and a discriminator network for disentanglement of artifacts from CT. Because training networks with a mean-square error loss function has shown over-smoothed images in results [80], they present a traditional loss coupled with an adversarial loss working great overall for image-to-image translation tasks.

Liao et al. [64] proposed a CycleGAN-based artifact disentanglement network that separate the metal artifacts and normal tissues from CT images in the latent space. It was the first unsupervised method to CT and showed quantitative evaluation results against other supervised/unsupervised MAR methods with synthesized data. However, this method may not effectively separate metal artifacts in corrupted CT images due to the complexity of metal artifact.

2.4 Summary

We have exhibited CT physics, CT artifacts, and previous MAR methods in this chapter. It was possible to understand the gap between the CT algorithm and the CT device by examining the physical characteristics of CT system. CT artifacts were examined from the perspectives of physics and patients respectively. The research flow was identified with representative methodologies of sinogram-completion based MAR, sinogram-correction based MAR, and deep-learning based MAR. In the following chapters, we introduce our MAR method improved in performance by analyzing the examined MAR methods above.

Chapter 3

Constrained Beam-hardening Estimator for Polychromatic X-ray

The sinogram-correction based MAR methods effectively reduce artifacts from CT images, which is of great help not only for diagnosis but also treatment planning for radiotheraphy. However, due to the complexity of the model and the tremendous amount of computation that comes from the structural limitations of iterative reconstruction to find parameters in the model, its practical usage is greatly limited. In this chapter, we present a novel model CBHE that more accurately estimates the beam-hardening error while deviating from these structural limitations. The main idea of the proposed model is to simplify the computation of the artifact by beam hardening. Since attenuation coefficient of polychromatic X-ray decreases when the ray penetrates an irradiated object, the accumulation of the reduced amounts of the polychromatic X-ray attenuation coefficient causes underestimation of attenuation in projections and it results in the metal artifact. The proposed model is derived through the following steps:

1. Describe the polychromatic X-ray attenuation coefficient with respect to the X-ray transmission length.

2. Derive the projection error - the underestimated amount - in the projections from the polychromatic X-ray attenuation coefficient.

3. Establish the constrained beam-hardening estimator by approximating the projection error.

3.1 Characteristics of polychromatic X-ray

Photons emitted from an X-ray tube do not all have the same energy. As the energy spectrum is shifted and narrowed to higher energies when polychromatic X-ray photons penetrate an irradiated object, the attenuation coefficient of the polychromatic X-rays changes depending on the ray transmission length. Let $\hat{\mu}_s(l)$ be the polychromatic X-ray attenuation coefficient with the ray transmission length l. In terms of the Radon transform, the measured X-ray projection data of the polychromatic X-ray source, denoted by P, can be formulated as

$$P = \int_0^l \hat{\mu}_s(l')dl'. \tag{3.1}$$

The attenuation information in accordance with the transmission length is required to describe $\hat{\mu}_s(l)$. The attenuation of the X-ray intensity is derived by the Beer-Lambert law. $I(E)$, which represents the intensity at energy level E after passing through a homogeneous material s of length l, is usually expressed as

$$I(E) = I_0(E) \times \exp\{-\mu_s(E)\, l\}. \tag{3.2}$$

To indicate the change in intensity over the transmission length, (3.2) can be modified to

$$I(E,l) = I(E,0) \times \exp\{-\mu_s(E)\, l\}. \tag{3.3}$$

By taking logarithm, P is also derived as

$$\begin{aligned} P &= -\ln \frac{\int I(E,l)dE}{\int I(E,0)dE} \\ &= -\ln \frac{\int I(E,0) \times \exp\{-\mu_s(E)\, l\}dE}{\int I(E,0)dE}. \end{aligned} \tag{3.4}$$

$\hat{\mu}_s(l)$ can be formulated through (3.1) and (3.4):

$$\begin{aligned} \hat{\mu}_s(l) &= \frac{dP}{dl} \\ &= \frac{d}{dl}\left(-\ln \frac{\int I(E,0) \times \exp\{-\mu_s(E)\, l\}dE}{\int I(E,0)dE}\right) \\ &= -\frac{\int I(E,0) \times \exp\{-\mu_s(E)\, l\} \times (-\mu_s(E))dE}{\int I(E,0) \times \exp\{-\mu_s(E)\, l\}dE} \\ &= -\frac{g_s'(l)}{g_s(l)}, \end{aligned} \tag{3.5}$$

where

$$\begin{aligned} g_s(l) &= \int I(E,0) \times \exp\{-\mu_s(E)\, l\}dE, \\ g_s'(l) &= \int I(E,0) \times \exp\{-\mu_s(E)\, l\} \times (-\mu_s(E))dE. \end{aligned}$$

3.2 Constrained beam-hardening estimator

The increase in X-ray energy due to beam-hardening causes attenuations in the projections to be underestimated. The underestimated error in the projections is the accumulation of reduced amounts of the polychromatic X-ray attenuation coefficient (3.5) along the transmission length. The polychromatic X-ray attenuation coefficient $\hat{\mu}_s(l)$ decreases from $\hat{\mu}_s(0)$ and converges to $\mu_s(E_M)$ as

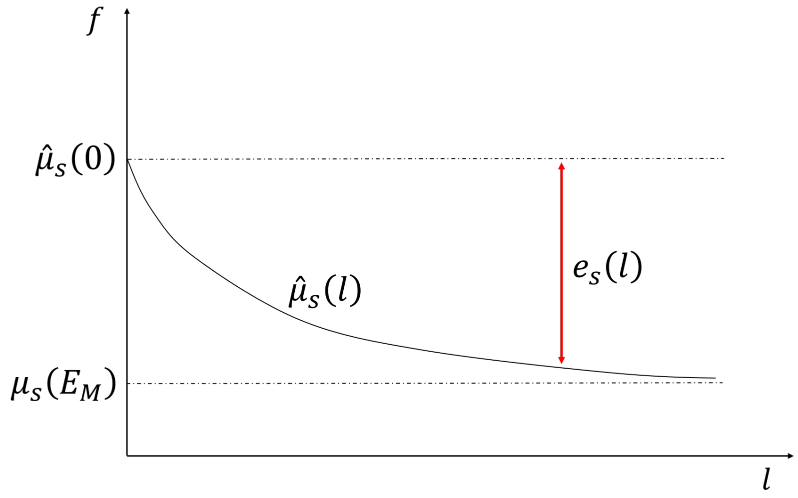

Figure 3.1 Illustration of $\hat{\mu}_s(l)$ and $e_s(l)$. f means the attenuation coefficient (mm^{-1}).

the transmission length l increases, where $E \in [E_m, E_M]$ (Fig. 3.1). $\hat{\mu}_s(0)$ is the initial value of $\hat{\mu}_s(l)$ and can be calculated as

$$\hat{\mu}_s(0) = \int_{E_m}^{E_M} \eta(E, 0) \times \mu_s(E) dE, \tag{3.6}$$

where $\eta(E, 0) = I(E, 0) / \int_{E_m}^{E_M} I(E, 0) dE$ indicates the normalized energy spectrum of the polychromatic X-ray. The reduced amount $e_s(l)$ is defined by the difference between $\hat{\mu}_s(0)$ and $\hat{\mu}_s(l)$:

$$e_s(l) = \hat{\mu}_s(0) - \hat{\mu}_s(l) = \hat{\mu}_s(0) + \frac{g_s'(l)}{g_s(l)}. \tag{3.7}$$

The beam-hardening error (BHE), denoted by $\psi_s(l)$, is the integral of $e_s(l)$ with respect to the transmission length l:

$$\psi_s(l) = \int_0^l e_s(l') dl' = \hat{\mu}_s(0)\, l + \ln \frac{g_s(l)}{g_s(0)}, \tag{3.8}$$

where

$$\ln \frac{g_s(l)}{g_s(0)} = \ln\Big(\int_{E_m}^{E_M} \eta(E,0) \times \exp\{-\mu_s(E)\, l\} dE\Big) \tag{3.9}$$

$\ln \frac{g_s(l)}{g_s(0)}$ depends on the X-ray spectrum $\eta(E,0)$ and the material attenuation coefficients $\mu_s(E)$. These dependencies make direct computations difficult and computationally complex. To avoid them, we solve the problem through a constrained approximation because partial problems may be terminated by approximation. Let $\ln \frac{g_s(l)}{g_s(0)}$ be transformed to

$$\begin{aligned}
&\ln \frac{g_s(l)}{g_s(0)} \\
&= \ln\Big(\int_{E_m}^{E_M} \eta(E,0) \times \exp\{-\mu_s(E)\, l\} dE\Big) \\
&= \ln\Big(\int_{E_m}^{E_M} \eta(E,0) \times \exp\{-\big(\mu_s(E) - \mu_s(E_M) + \mu_s(E_M)\big)\, l\} dE\Big) \\
&= -\mu_s(E_M)\, l + \ln\Big(\int_{E_m}^{E_M} \eta(E,0) \times \exp\{-\big(\mu_s(E) - \mu_s(E_M)\big)\, l\} dE\Big) \\
&= -\mu_s(E_M)\, l + \ln\Big(\int_{E_m}^{E_M} \eta(E,0) \times \exp\{-(E - E_M) \times \frac{\mu_s(E) - \mu_s(E_M)}{E - E_M}\, l\} dE\Big).
\end{aligned} \tag{3.10}$$

We consider $E \in [E_h, E_H]$ satisfying $E_m \leq E_h < E_H \leq E_M$. As the integral value of the second term in (3.10) is always positive, we can derive that there is an $\alpha > 0$ that satisfies the following approximation:

$$\begin{aligned}
&\int_{E_m}^{E_M} \eta(E,0) \times \exp\{-(E - E_M) \times \frac{\mu_s(E) - \mu_s(E_M)}{E - E_M}\, l\} dE \\
\approx &\Big(\int_{E_h}^{E_H} \eta(E,0) \times \exp\{-(E - E_H) \times \frac{\mu_s(E) - \mu_s(E_H)}{E - E_H}\, l\} dE\Big)^{\alpha}.
\end{aligned} \tag{3.11}$$

The key to the proposed estimator is to minimize the error in the model while simplifying the structure of (3.10). For $\eta(E,0)$, by choosing an appropriate number $k \in R$, it is possible to observe the following approximation [8]:

$$\int_{E_h}^{E_H} (\eta(E,0) - \frac{k}{E_H - E_h}) \times \exp\{-(E - E_H) \times \frac{\mu_s(E) - \mu_s(E_H)}{E - E_H}\, l\} dE \approx 0. \tag{3.12}$$

Through trial and error, the most meaningful results were found when the value $\frac{\mu_s(E)-\mu_s(E_H)}{E-E_H}$ was assumed to be a constant and $\mu_s(E_H) = \hat{\mu}_s(0)$. Based on this knowledge, the following assumptions are made:

$$\mu_s(E_h) = 2\mu_s(E_H) = 2\hat{\mu}_s(0) \text{ and } \frac{\mu_s(E) - \mu_s(E_H)}{E - E_H} \approx C. \tag{3.13}$$

Since the value of k is almost one and is not important for the result, it can be replaced with '1'. By applying the above approximations, (3.10) can be derived as

$$\begin{aligned}
&\ln \frac{g_s(l)}{g_s(0)} \\
&= -\mu_s(E_M)\, l + \ln\biggl(\int_{E_m}^{E_M} \eta(E,0) \times \exp\{-(E - E_M) \times \frac{\mu_s(E) - \mu_s(E_M)}{E - E_M}\, l\} dE\biggr) \\
&\approx -\mu_s(E_M)\, l + \ln\biggl(\Bigl(\int_{E_h}^{E_H} \frac{1}{E_H - E_h} \times \exp\{-(E - E_H)\, C\, l\} dE\Bigr)^{\alpha}\biggr) \\
&= -\mu_s(E_M)\, l + \alpha \ln\biggl(\frac{1 - \exp\{-\mu_s(E_H)\, l\}}{\mu_s(E_H)\, l}\biggr).
\end{aligned} \tag{3.14}$$

This constrained approximation makes it possible to avoid dependencies in (3.9), leading to a faster computation. Finally, the estimated projection error $\tilde{\psi}_s(l)$, the constrained beam-hardening estimator, can be derived in the following linear form:

$$\tilde{\psi}_s(l) = \beta\, \tilde{\psi}_{s,1}(l) + \alpha\, \tilde{\psi}_{s,2}(l), \tag{3.15}$$

where

$$\beta = \hat{\mu}_s(0) - \mu_s(E_M),$$

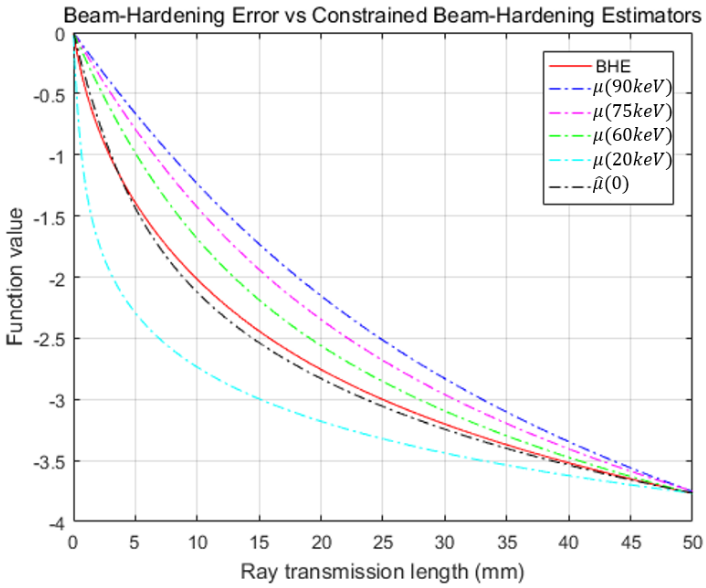

Figure 3.2 Relationship between BHE and CBHEs with E_H at 90, 75, 60, 20 keV, and CBHE with $\hat{\mu}(0)$ for Titanium.

$$\tilde{\psi}_{s,1}(l) = l,$$
$$\tilde{\psi}_{s,2}(l) = \ln\left(\frac{1 - \exp\{-\mu_s(E_H)\, l\}}{\mu_s(E_H)\, l}\right). \tag{3.16}$$

Fig. 3.2 shows the relationship between the beam-hardening error $\psi(l)$ and the constrained beam-hardening estimator $\tilde{\psi}(l)$. To show the shape of $\tilde{\psi}_2(l)$ according to the value of $\mu(E_H)$, $\psi(l) - \beta\tilde{\psi}_1(l)$ is compared to each $\alpha\,\tilde{\psi}_2(l)$ with E_H at 90, 75, 60, and 20 keV, and $\alpha\,\tilde{\psi}_2(l)$ with $\mu(E_H)$ as $\hat{\mu}(0)$. These profiles are generated with an X-ray source spectrum at an energy range of 20-90 keV provided by a CBCT system supplier (Ray Co., Korea), and with attenuation coefficients found by experiments [3]. As shown in Fig. 3.2, $\alpha\,\tilde{\psi}_2(l)$ with $\hat{\mu}(0)$ is highly congruent with $\psi(l) - \beta\tilde{\psi}_1(l)$. The proximity of the constrained beam-hardening estimator to the beam-hardening error with various metal types can

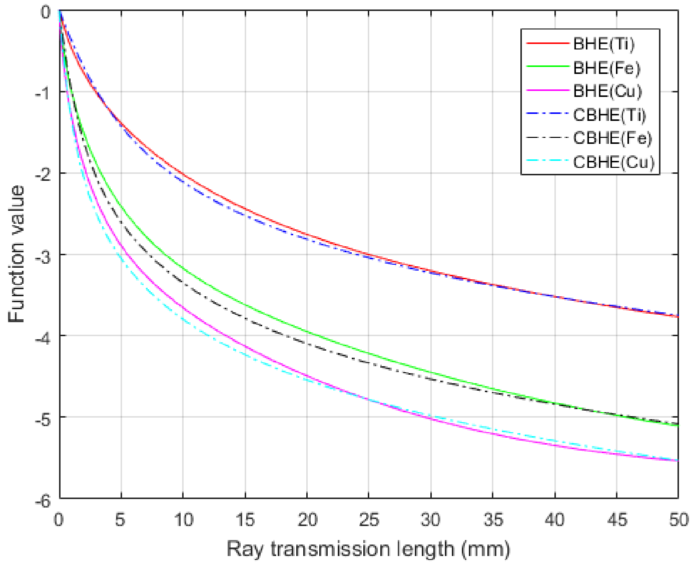

Figure 3.3 Relationship between BHE and CBHE for Titanium (Ti), Iron (Fe), and Copper (Cu).

be shown in Fig. 3.3. These plots are calculated with the same conditions of Fig. 3.2 except for metal types.

Fig. 3.4 shows the characteristics of each term in (3.15) after reconstruction ($\Re^{-1}$ indicates the filtered back-projection operator). $\Re^{-1}(\tilde{\psi}_{s,2}(l))$ has the shape of a metal artifact turned upside down. It is directly related to the correction of the streak artifact around the metal region and the cupping artifact inside the metal region. $\Re^{-1}(\tilde{\psi}_{s,1}(l))$ has the shape of a homogeneous metal region and compensates for the intensity reduced by $\Re^{-1}(\tilde{\psi}_{s,2}(l))$ in the metal region. It has the same geometric size and shape as the metal segmentation mask. The segmentation mask consists of a binary image in which the metal area is filled only with the value one, whereas $\Re^{-1}(\tilde{\psi}_{s,1}(l))$ has an unspecified real value

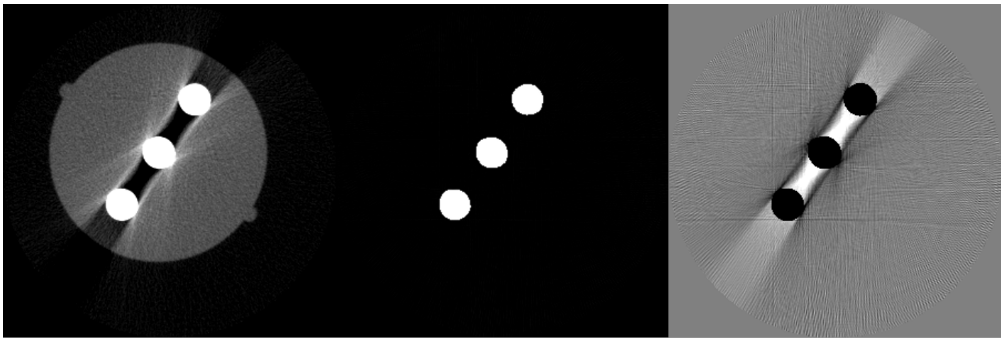

(a) (b) (c)

Figure 3.4 The shapes of each term in CBHE. (a) the uncorrected f_{CT} (b) $\Re^{-1}(\tilde{\psi}_1(l))$ (c) $\Re^{-1}(\tilde{\psi}_2(l))$.

calculated through the forward/backward projection process.

3.3 Summary

In this chapter, we have presented a novel beam-hardening estimator (CBHE) to reduce the computational burden of approximating metal artifacts. The most parameters of CBHE are decided from the CT system and experiments. The only unknown parameter to find out is α and it is not related to the reconstruction process. CBHE approximates beam-hardening error without iterative reconstruction and loss of accuracy (evaluations in the chapter 5). The entire process of the metal artifact reduction method with CBHE (3.15) is described in the next chapter 4.

Chapter 4

Metal Artifact Reduction with Constrained Beam-hardening Estimator

To reduce metal artifacts in CT images, there are other things to consider for estimating exact beam-hardening error. Our MAR method is based on the sinogram-correction approach. However, the proposed method does not perform correction on each projection unlike other methods based on the sinogram correction due to the non-iterative structure of CBHE. Since the parameters to be calculated or optimized can be decided regardless of the reconstruction step, the optimization of the parameters via iterative reconstruction is not needed.

The MAR method consists of two major steps: 1) calculate the transmission length of X-ray through the metal region, 2) estimate the metal artifact. In the following sections, we describe the details of each step and the extension of the algorithm to more general cases where several types of metal exist. For further improved results, two refinement methods are presented additionally.

4.1 Metal segmentation

Except for some metal artifact reduction methods, most methods go through the process of identifying metal regions. The accuracy of the identified metal region determines the actual performance of metal artifact reduction methods. Metal regions can be segmented in projections or CT images. Most of MAR methods perform the segmentation task in the projection domain except for some methods that use information of CT images for correction [81].

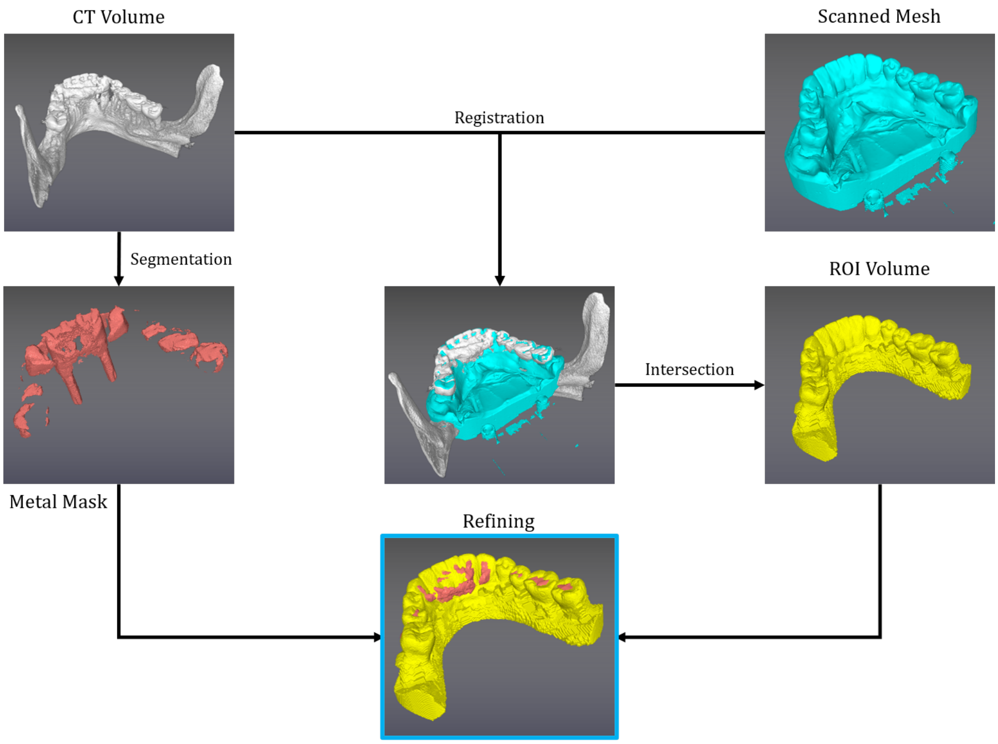

Figure 4.1 Example of metal segmentation by matching a scanned model

Since the proposed model in this study uses information on the transmission length of X-ray through the metal region, the segmented metal region on the

CT image is required. For metal segmentation on CT images, a threshold-based technique is typically used [5,39,82]. Metal artifacts appear in the form of white streaks or dark shadows extending radially around the metal region. There are usually points that separate these artifacts from the metal region values, and the metal region is separated by specifying a threshold. Adaptive filtering [24] or mean-shift technique [83] to weaken the streaks can be applied additionally since there are some cases that it is difficult to distinguish between artifacts and metal regions.

In the cases that the thresholding technique has difficulty in distinguishing metals from artifacts, it may be helpful to use other information that is relatively obtainable, for example, a scanned data for the metal region. During dental treatment process, scanned models are often obtained. In this cases, refined metal regions are identified through Boolean operations between the incomplete metal regions and the scanned models aligned to CT images. Fig. 4.1 shows an example of metal segmentation with a scanned model. In this study, we used only a threshold-based technique to ensure the robustness of metal segmentation.

4.2 X-ray transmission length

X-ray transmission length for metal area in each projection is calculated by using the segmented metal region. The segmented metal region is converted into a binary mask, and the CT scan geometry for each projection is required.

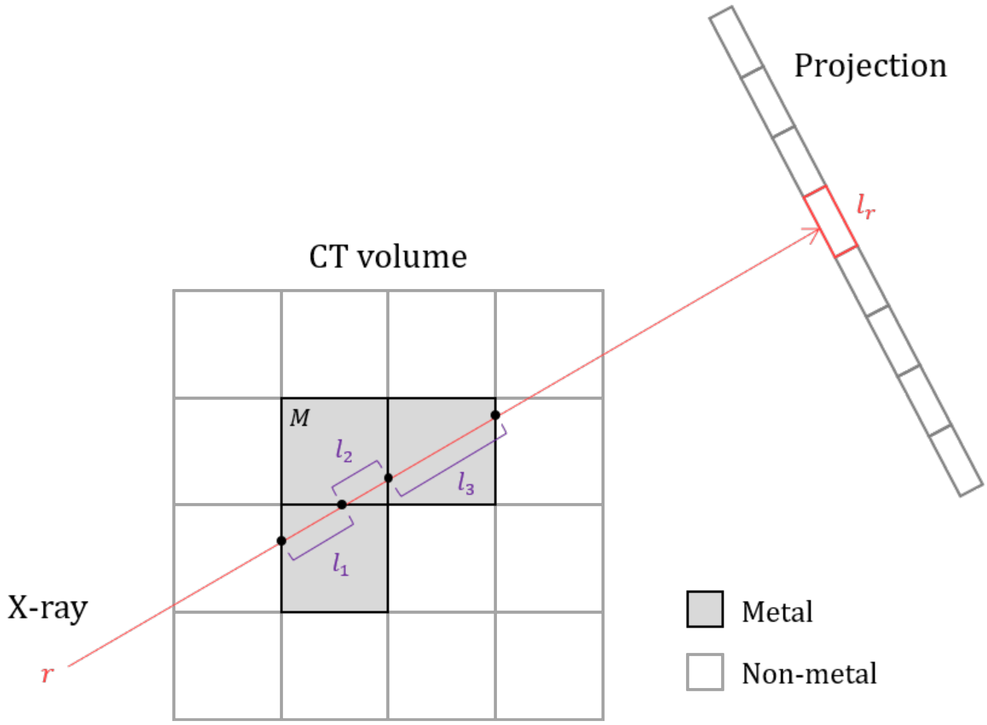

Figure 4.2 Calculation of X-ray transmission length

The process of calculating the X-ray transmission length for each pixel on the projection is very similar to a pixel-driven ray-casting of volume rendering process [84]. The intersection lengths between each line r from a position of X-ray source to pixels on the projection P and each voxel of the metal region in the CT volume are calculated and accumulated (Fig. 4.2). Since the CT value in the voxel of the metal region is not considered, the entire process can be

Algorithm 1 Calculation of X-ray transmission length

1: Prepare a binary mask M for the metal region

2: For each ray r for each pixel in a projection P, each intersection l_i between r and M is calculated by using Siddon's method [85]

3: Accumulate the intersection lengths to l_r

transformed into line integrals for the binary mask of the metal region (Alg. 1):

$$l_r = \sum_{i=1}^{n} l_i = \int_r M\,ds, \tag{4.1}$$

where M is a binary mask consisting of 1 for metal voxels and 0 for non-metal voxels.

4.3 Artifact reduction with CBHE

4.3.1 Artifact estimation for a single type of metal

Fig. 4.3 shows the entire process of the proposed method for the case of containing single metal type. With the X-ray transmission length calculated through metal segmentation and the proposed constrained beam-hardening estimator, the corrected projection can be expressed as $P + \tilde{\psi}_s(l)$. Because the filtered back-projection has linearity, the corrected CT image can be expressed as

$$\begin{aligned} \Re^{-1}(P + \tilde{\psi}_s(l)) &= \Re^{-1}(P) + \Re^{-1}(\tilde{\psi}_s(l)) \\ &= f_{CT} + \beta\, \Re^{-1}(\tilde{\psi}_{s,1}(l)) + \alpha\, \Re^{-1}(\tilde{\psi}_{s,2}(l)), \end{aligned} \tag{4.2}$$

where $\Re^{-1}(P)$ is the uncorrected CT (f_{CT}), and $\Re^{-1}(\tilde{\psi}_s(l))$ denotes the constrained beam-hardening estimator.

The reconstructions for $\Re^{-1}(\tilde{\psi}_{s,1}(l))$ and $\Re^{-1}(\tilde{\psi}_{s,2}(l))$ are performed once in the entire process. These are used to alleviate the beam-hardening effect on f_{CT} in accordance with (4.2). To satisfy the assumption condition (3.13), it is recommended to calculate $\hat{\mu}_s(0)$ precisely, but it is difficult to obtain additional information about the X-ray spectrum and the material attenuation properties (e.g. X-ray mass attenuation coefficient table [3]). Empirically, the lowest value of the metal region in the CT image before HU conversion is close to $\hat{\mu}_s(0)$, hence it can be an alternative. β only participates in compensating for the entire metal region with the same value, and its value is irrelevant as long as β makes $\Re^{-1}(\tilde{\psi}_{s,1}(l))$ larger than the maximum amount reduced by $\Re^{-1}(\tilde{\psi}_{s,2}(l))$. α is the unknown coefficient that minimizes the beam-hardening artifact. This condition can be obtained by solving the problem of minimizing the following

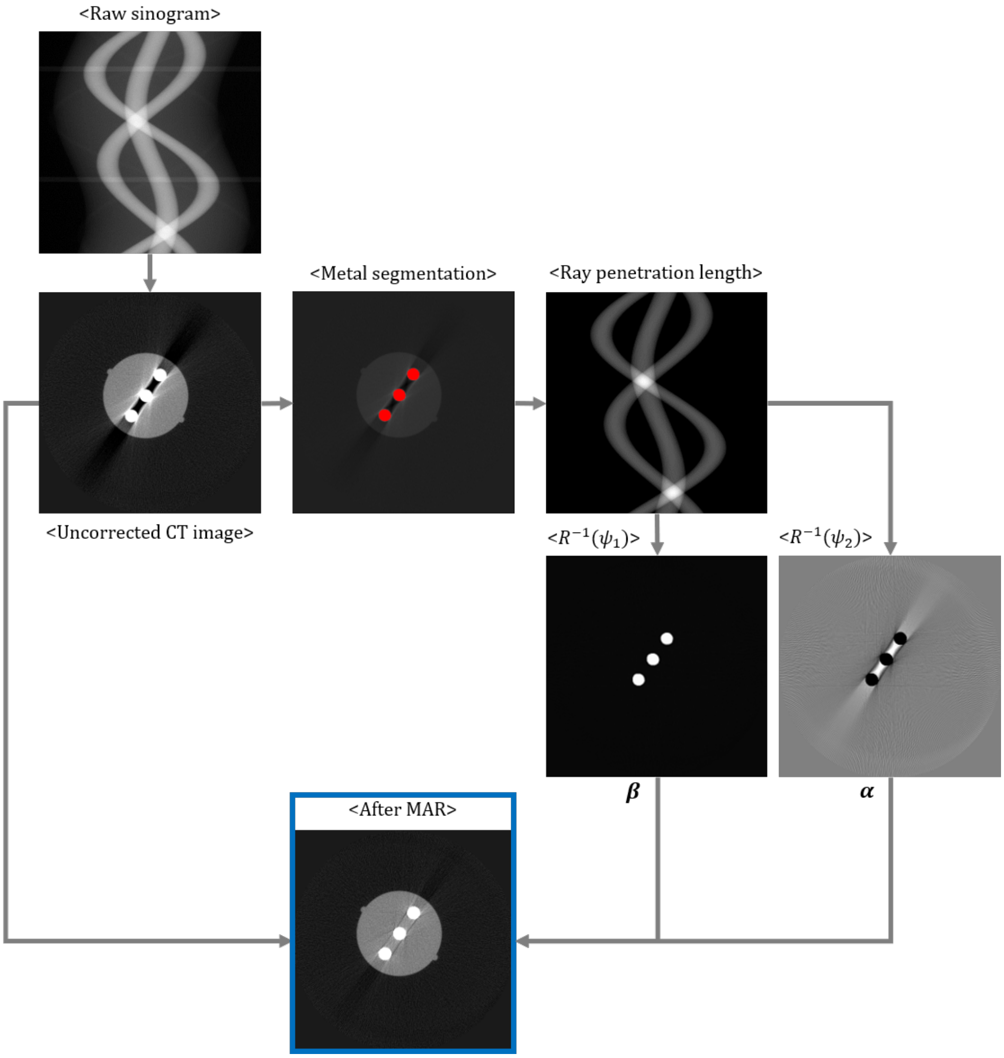

Figure 4.3 Example of the entire process of the proposed method for a case of containing single type of metal objects.

function:

$$argmin_{\alpha}\Big(SD\big(f_{CT}(x) + \alpha\,\Re^{-1}(\tilde{\psi}_{s,2}(l))(x)\big)\Big) \text{ for } M(x) > 0, \qquad (4.3)$$

where SD indicates the standard deviation operator and $M(x)$ is the mask

Algorithm 2 MAR with CBHE for Single Type of Metal

1: Reconstruct a CT image f using FDK [73]

2: Segment the entire metal region M from f

3: Generate the projections $\tilde{\psi}_1(l)$ by computing the ray transmission length along M through forward-projection

4: Generate the projections $\tilde{\psi}_2(l)$ by (3.16) using the ray transmission length

5: Reconstruct $\Re^{-1}(\tilde{\psi}_1(l))$ and $\Re^{-1}(\tilde{\psi}_2(l))$ using FDK

6: Find out the unknown coefficient α of (4.2) by solving the minimization problem for the energy function defined as (4.3)

7: Generate the final CT image by (4.2)

image representing the metal region. This function represents the extent of the cupping artifact inside the metal region. [8] proposed an energy function with a focus on streak minimization. The overall flow of the proposed metal artifact reduction method is described in Alg. 2.

4.3.2 Artifact estimation for multiple types of metal

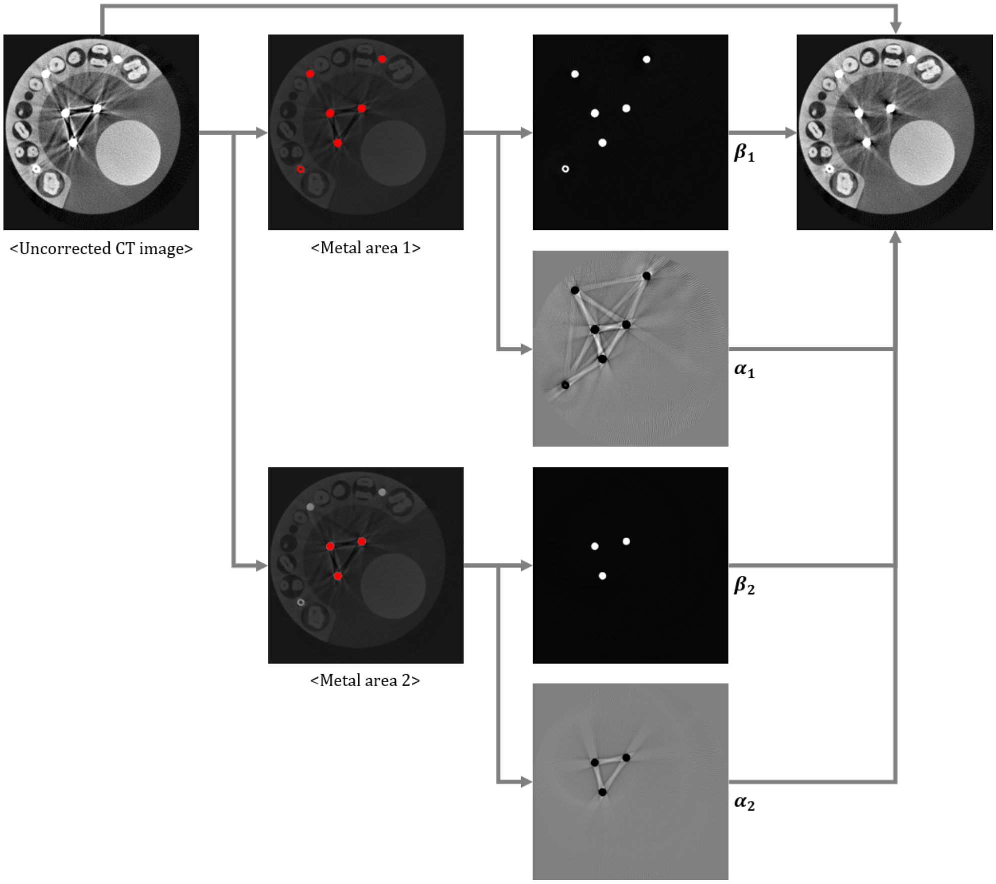

Figure 4.4 Example of the entire process of the proposed method for a case of containing two types of metal objects (Aluminum and Titanium).

Since the proposed constrained beam-hardening estimator is defined for a single metal, the proposed method also assumes a case of a single type of metal involved only. However, there are many cases in which several types of metals are contained in scanned area (Fig. 4.4). By analyzing the variation of attenuation coefficients of several materials according to energy level, the attenuation coefficients showed similar shape of change with only different scales [9]. In the idea that it is possible to replace some of the artifacts caused by the high density metal with the artifacts caused by the low density metal, the MAR algorithm needs little modification in the part of metal segmentation. The MAR method is performed sequentially from the lowest density metal to the highest density metal in the entire metal area. For each step of metal segmentation, the metal area contains not only the area of the current metal but also the area of the higher density metals (Fig. 4.4). In this manner, the proposed method can mitigate artifacts not only between the same metals but also between different metals. The corrected CT image for the general case is expressed as

$$\begin{aligned}\Re^{-1}(P + \sum_{k=1}^{n} \tilde{\psi}_{s_k}(l)) &= \Re^{-1}(P) + \Re^{-1}(\sum_{k=1}^{n} \tilde{\psi}_{s_k}(l)) \\ &= f_{CT} + \sum_{k=1}^{n} \beta_k \, \Re^{-1}(\tilde{\psi}_{s_k,1}(l)) + \sum_{k=1}^{n} \alpha_k \, \Re^{-1}(\tilde{\psi}_{s_k,2}(l)),\end{aligned} \tag{4.4}$$

and the detailed process is stated in Alg. 3.

Algorithm 3 MAR with CBHE for Multiple Types of Metal

1: Reconstruct a CT image f using FDK [73]

2: Segment the entire metal region M from f

3: Identify the types of the contained metals $S = (s_1, s_2, ..., s_n)$ and the area $M_i \in M$

4: Choose the metal s_k of the lowest density in S

5: Generate $\tilde{\psi}_{s_k,1}(l)$ projection data by computing the ray transmission length along M through forward-projection

6: Generate $\tilde{\psi}_{s_k,2}(l)$ projection data by (3.16) using the ray transmission length

7: Reconstruct $\Re^{-1}(\tilde{\psi}_{s_k,1}(l))$ and $\Re^{-1}(\tilde{\psi}_{s_k,2}(l))$ using FDK

8: Find out the unknown coefficient α_{s_k} of (4.2) by solving the minimization problem for the energy function defined as (4.3)

9: Remove s_k from S and M_k from M

10: If S is not empty, then goto 4:

11: Generate the final CT image by (4.4)

4.4 Refinement methods

4.4.1 Collaboration with ADN

Although the proposed MAR method may recover the information corrupted by the beam-hardening artifacts, it is not perfect for artifacts caused by factors other than the beam-hardening. Image-domain MAR methods focus on identifying and directly removing artifacts on CT image. In research on image processing techniques as a post-processing strategy, MAR methods based on deep-learning have recently been studied, and especially, studies based on GAN [58] are quite effective [65]. However, as the complexity of metal artifact noise (e.g., streaking artifact, dark shadow artifact and salt-and-pepper noise) increases, the performance of GAN-based MAR methods decreases [66].

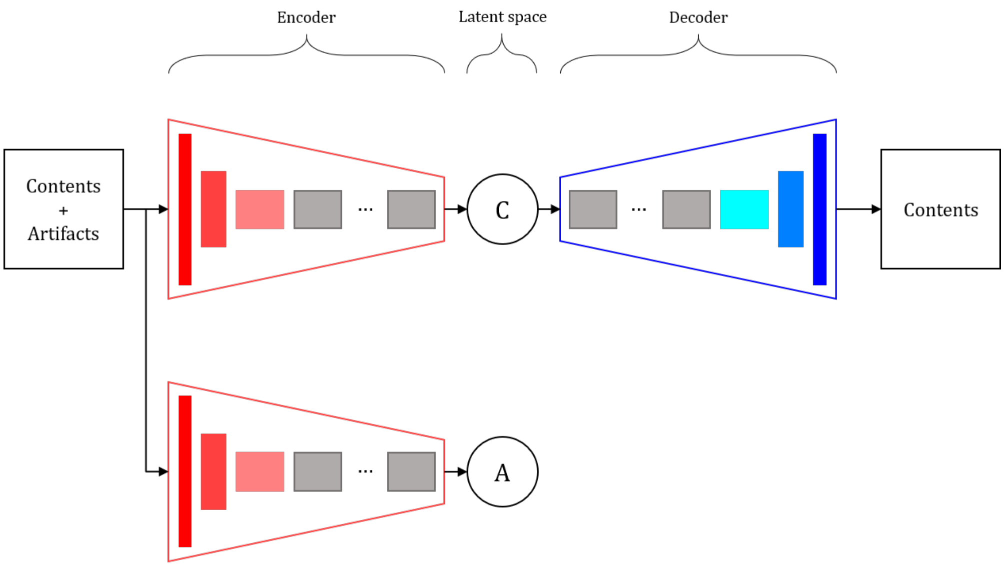

Figure 4.5 MAR process of the ADN network

Among the GAN-based MAR methods, Liao et al. [64] proposed an artifact disentanglement network (ADN) that shows better performance on MAR than other supervised/unsupervised MAR methods. The author transformed the metal artifact problem to a disentanglement problem. ADN is a disentanglement network to separate uncorrupted content components in CT images from artifact components. The authors assumed that two components can be disentangled in latent space. ADN consists of encoders for artifacts and contents separately and decoders for contents (Fig. 4.5). ADN supports an unsupervised training way where no paired CT images are required.

The proposed MAR method and ADN have features that can complement each other's shortcomings. Through the proposed MAR method, the artifact complexity on CT image can be rapidly reduced, and the remaining artifacts can be effectively reduced through ADN. We propose a collaboration method to improve results of the proposed MAR method through a cooperation with ADN. The overall process is illustrated in Fig. 4.6. As the ADN network takes a normalized image in a range of [-1, 1] as a input, data normalization is performed to load the MAR result from the proposed MAR method. The normalization range should contain contents from air to bone regions unaffected by artifacts. After the preparation, an artifact-free image is generated through ADN. The metal region in the artifact-free image has been replaced by values in bone or soft-tissue regions. Therefore, it is necessary to blend the metal regions obtained in the previous process of the proposed MAR method.

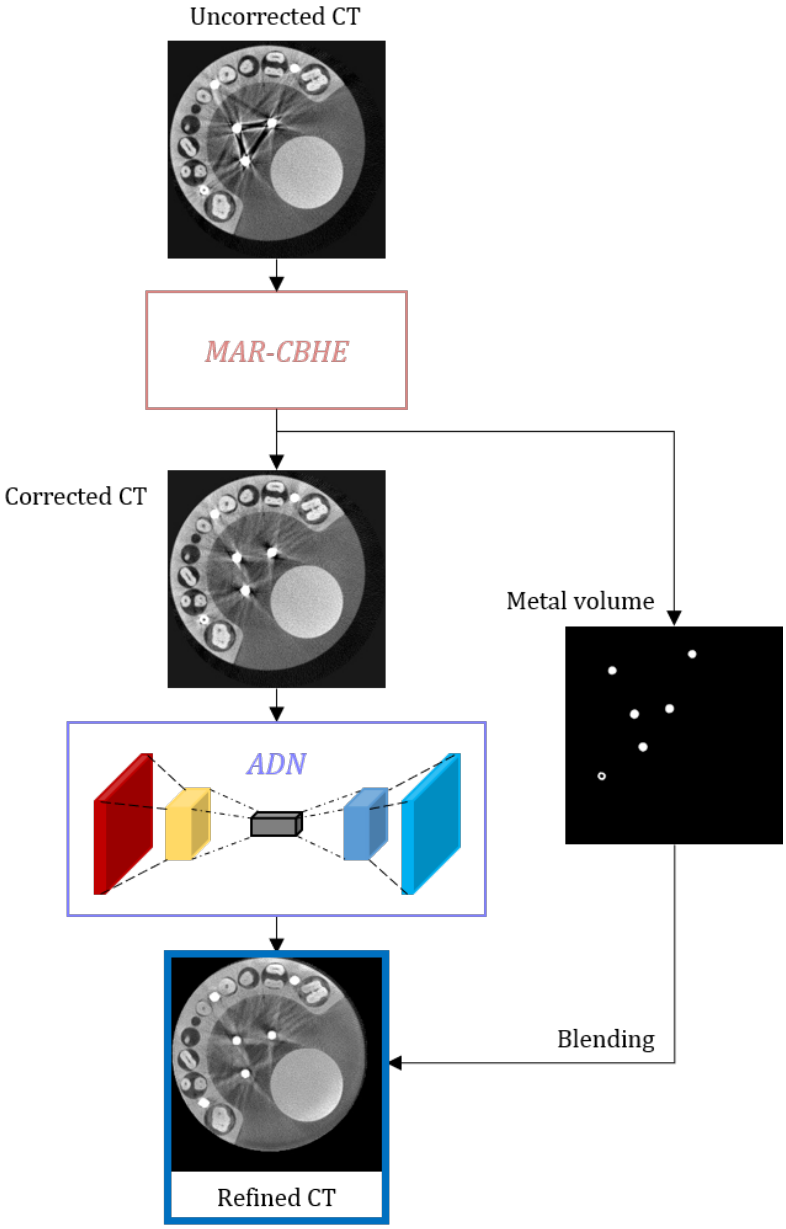

Figure 4.6 Example of post-processing with ADN

4.4.2 Application of CBHE to bone

Although the proposed MAR method limited the beam-hardening for metal only, artifacts due to beam-hardening occur when the transmission length is not short even for a material with a fairly high density such as bone. There are cases where artifacts such as metal artifacts remain after performing MAR 4.7. By considering the material as a low-density metal and applying the proposed model, the residual artifacts can be reduced effectively.

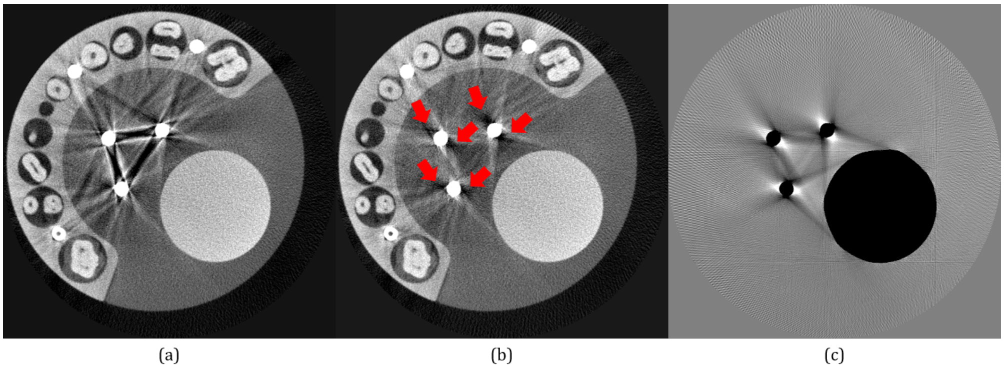

Figure 4.7 Example of residual artifacts due to beam-hardening by bone. (a) the uncorrected (b) proposed (c) CBHE with bone area

The overall process is illustrated in Fig. 4.8. After performing the proposed MAR on metal regions first, generate a mask for the target bone and metal area from the MAR result by segmentation techniques. The remaining process is equivalent to the process of the artifact reduction for a single type of metal.

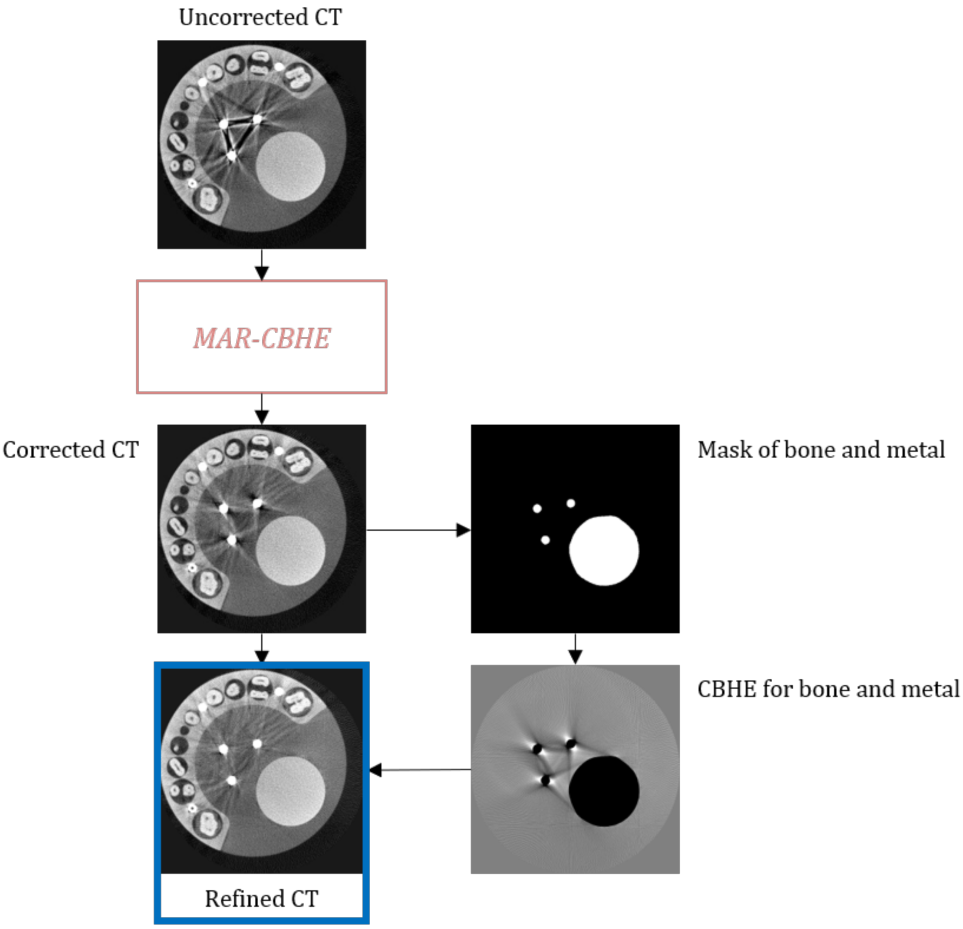

Figure 4.8 Example of post-processing with CBHE to bone.

4.5 Summary

In this chapter, we have described the entire process of the MAR method with CBHE. Our method estimates the artifacts in CT by non-iterative optimization. The method is extended to general cases of containing several types of metal. The corrected result is further refined by two refinement methods - collaborating with ADN model and applying CBHE to bone.

Chapter 5

Experimental Results

The proposed method was verified in various simulation environments about metal type and length for its accuracy and robustness. Two numerical simulation phantoms (JawSimulationPhantom1 and JawSimulationPhantom2) and twi hardware phantoms (TriTiPhantom and JawEquivPhantom) were used to evaluate the performance of the method qualitatively and quantitatively by comparison with those of the conventional sinogram-inpainting methods (LI-MAR and NMAR) [5, 20] and the recent model-based method (BCMAR) [8]. Two refinement methods were compared to the proposed method to show improvement of each method. All experiments are achieved on a Windows machine with Intel i7-6700 3.4GHz CPU, 32GB RAM, and NVIDIA GeForce GTX 1080.

5.1 Data preparation and quantitative measures

For the numerical simulation, projections were generated using the attenuation coefficients given in [3] and considering beam-hardening and Poisson noise. The CT system was a fan-beam with a projection width of 1024 and a source spectrum with a peak voltage of 90 keV provided by a CBCT system supplier (Ray Co., Korea). The source spectrum consisted of bins from 20 keV to 90 keV in 5 keV increments. The JawSimulationPhantom1 (Fig. 5.1) was designed with a neck bone, 12 teeth, and 2 metallic implants (specifically, Cu, Fe, and Ti for each case). The JawSimulationPhantom2 (Fig. 5.2) was designed with a neck bone, 8 teeth, and 4 metallic implants (Cu). This phantom was intended for experiments with various X-ray transmission lengths of less than 50 mm. The attenuation coefficients of all materials except metals were assumed to be constant. The beam-hardening effect of the metal region was expressed as the sum of the residuals for each bin after decreasing with the ray transmission length.

For real data, the TriTiPhantom containing three titanium rods was scanned by a CBCT system (Ray Co., Korea) with a peak voltage of 90 keV (Fig. 5.3). The resolution of the projection was 786 x 960 (width x height) and the resolution of the reconstructed image was 300 x 300 x 256. The JawEquivPhantom was made similarly to the mandibular structure includes bone, teeth, three aluminum rods on the outer circle and three titanium rods on the inner circle (Fig. 5.4) and it was also scanned by the same CBCT system. The water correction was not applied to either the numerical simulation or the two phantoms before performing the proposed MAR method.

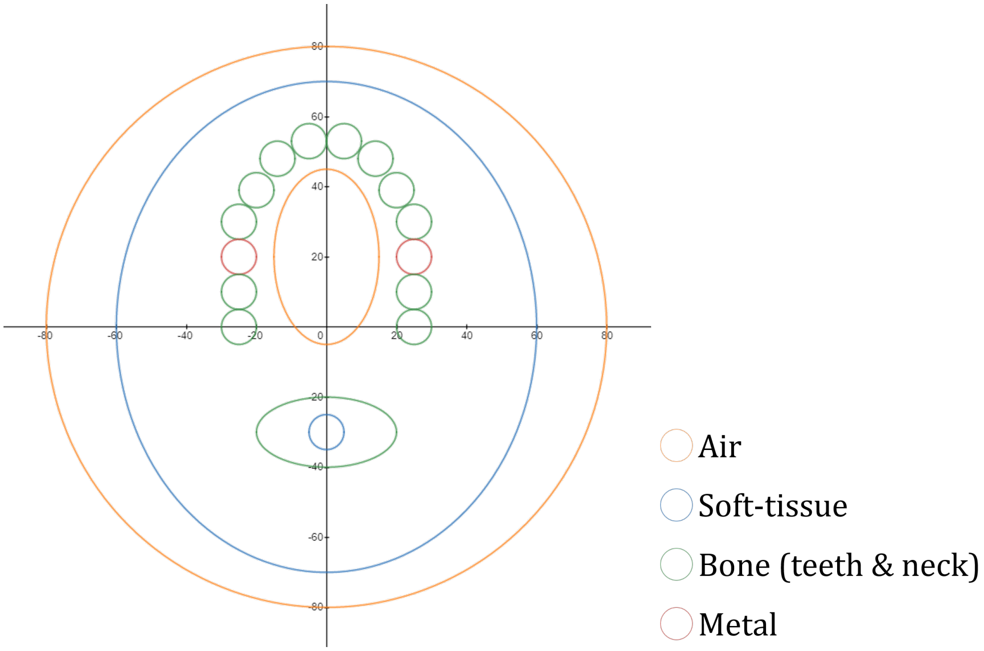

Figure 5.1 Design of JawSimulationPhantom1.

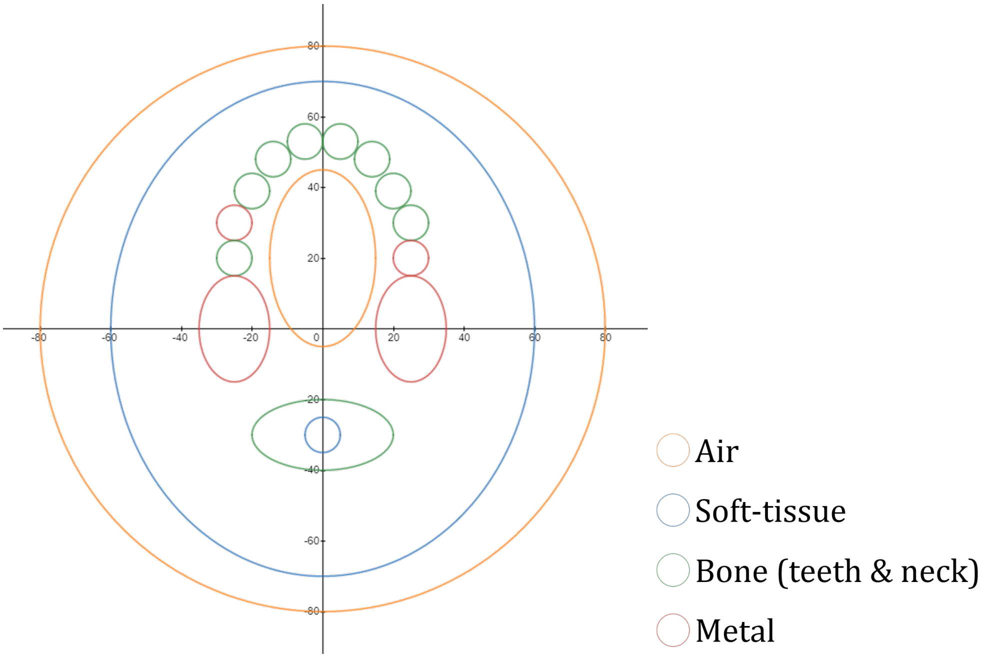

Figure 5.2 Design of JawSimulationPhantom2.

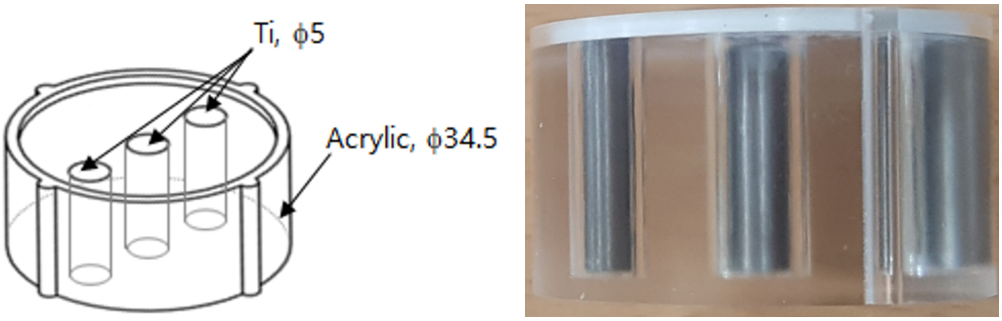

Figure 5.3 Design and photo of TriTiPhantom. Image courtesy of Ray Co., Korea

Figure 5.4 Photo of JawEquivPhantom. Image courtesy of Ray Co., Korea

To evaluate quantitatively, three metrics were employed as criteria: normalized root mean square difference (NRMSD), mean absolute deviation (MAD) [32], and contrast-to-noise ratio (CNR) [86]. For the numerical simulation, the NRMSD between the corrected and reference images was computed on the outside part of the metal area. For the hardware phantoms, because of the lack of reference images, MAD was computed on the outside part of the metal area in regions of interest (ROIs) by referencing the homogeneous region of the uncorrected image. CNR was computed on two selected regions. One is a metal area, and the other is a nearby area.

$$NRMSD(\%) = 100 * \sqrt{\frac{\sum_{i \in ROI}(x_i^{MAR} - x_i^{True})^2}{\sum_{i \in ROI}(x_i^{True})^2}} \tag{5.1}$$

$$MAD(HU) = \frac{1}{N} * \sum_{i \in ROI} |x_i^{MAR} - x_i^{True}| \tag{5.2}$$

$$CNR = \frac{2|M_A - M_B|}{\sqrt{\sigma_A^2 + \sigma_B^2}} \tag{5.3}$$

where x_i^{MAR} and x_i^{True} denote the i-th HU value of the ROI in the corrected and the reference images respectively, and N is the total number of selected ROIs. M_A and M_B denote the mean value of each region A and B in the CT. σ_A and σ_B are standard deviations.

5.2 Verification on constrained beam-hardening estimator

5.2.1 Accuracy

We conducted comparative analyses to validate the proposed model. First, each model was plotted to compare the correspondence of CBHE and BCMAR to BHE curve with the same conditions of the attenuation coefficients and the source spectrum for the numerical simulation. In clinical situations, because the ray transmission length of the metal rarely exceeds 200 mm (especially rarely exceeds 50 mm in dental CT), the two sections of less than 50 mm and less than 200 mm were chosen. Each model's parameter was optimized by minimizing the sum of differences between each model's curve and BHE's curve. In order to confirm the difference according to the degree of attenuation, three metals with different densities - Titanium, Iron, and Copper - and Cortical bone were considered.

Figures 5.5, 5.6, 5.7, and 5.8 show the comparison between CBHE and BCMAR compared to BHE for Titanium, Iron, Copper, and Cortical bone. Each model was calculated excluding $\tilde{\psi}_1(l)$ to focus on non-linearity of each model. In the case of less than 50 mm, it is shown that the curve of CBHE matches to the curve of BHE better than the curve of BCMAR model. However, in the case of less than 200 mm, CBHE shows better matching only for Titanium and Cortical bone. For Iron and Copper, CBHE shows steady divergence even after BHE converges sufficiently while BCMAR shows a better match.

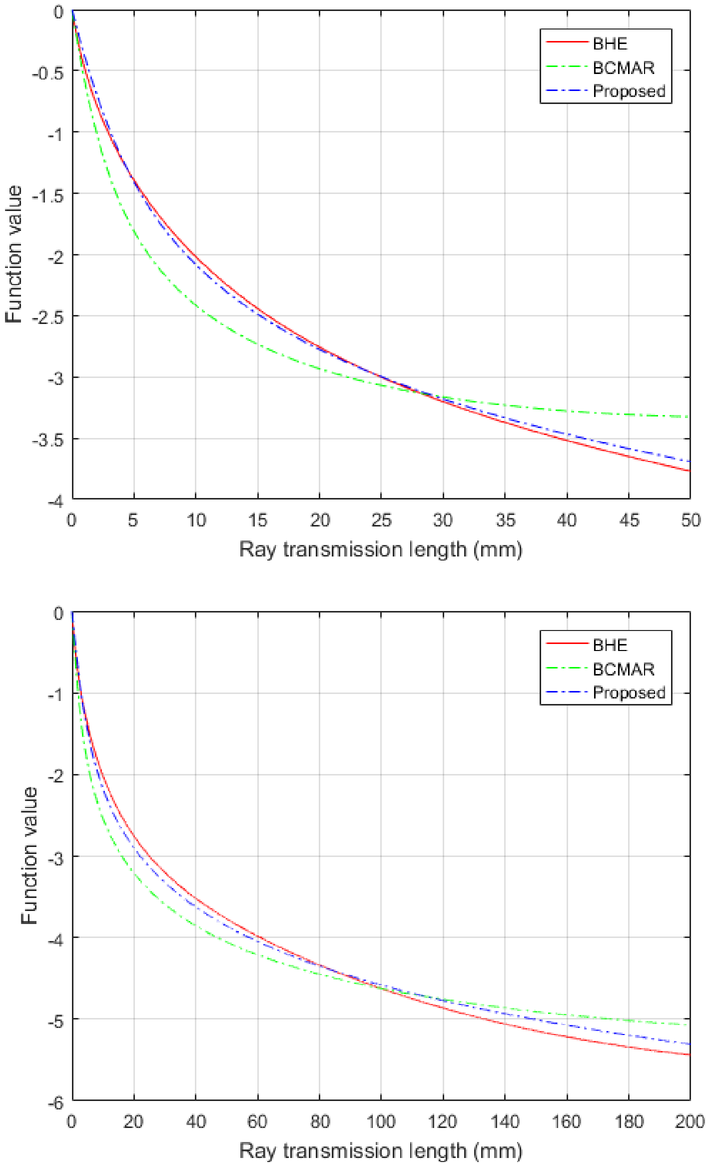

Figure 5.5 Comparison between BHE, BCMAR, and proposed model when the ray transmission length is less than 50 mm (top) and 200 mm (bottom) for Titanium (Ti).

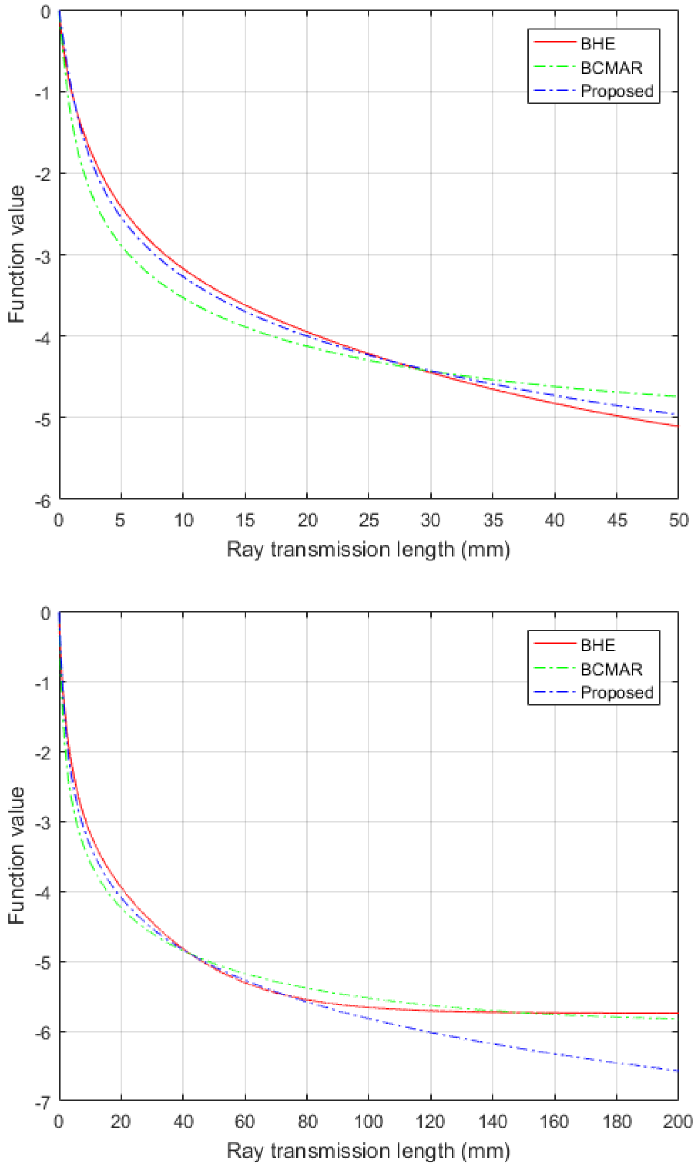

Figure 5.6 Comparison between BHE, BCMAR, and proposed model when the ray transmission length is less than 50 mm (top) and 200 mm (bottom) for Iron (Fe).

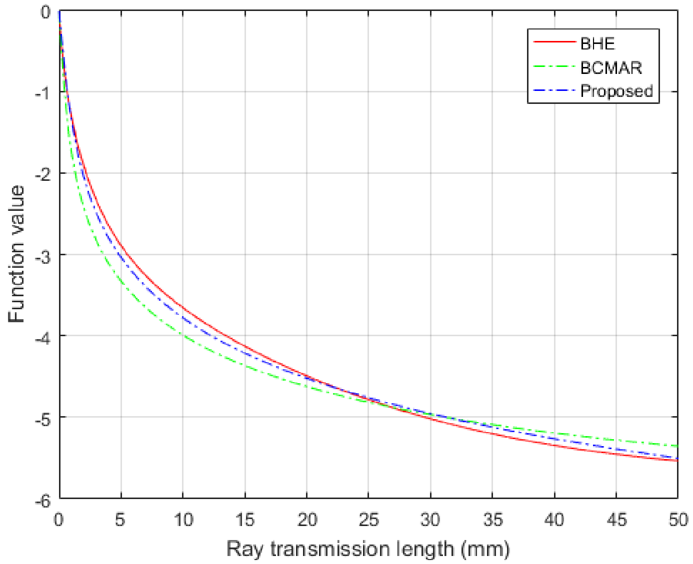

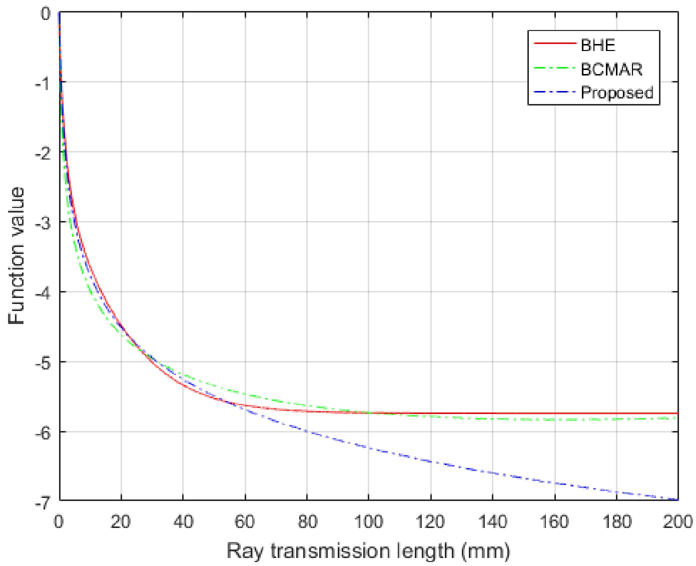

Figure 5.7 Comparison between BHE, BCMAR, and proposed model when the ray transmission length is less than 50 mm (top) and 200 mm (bottom) for Copper (Cu).

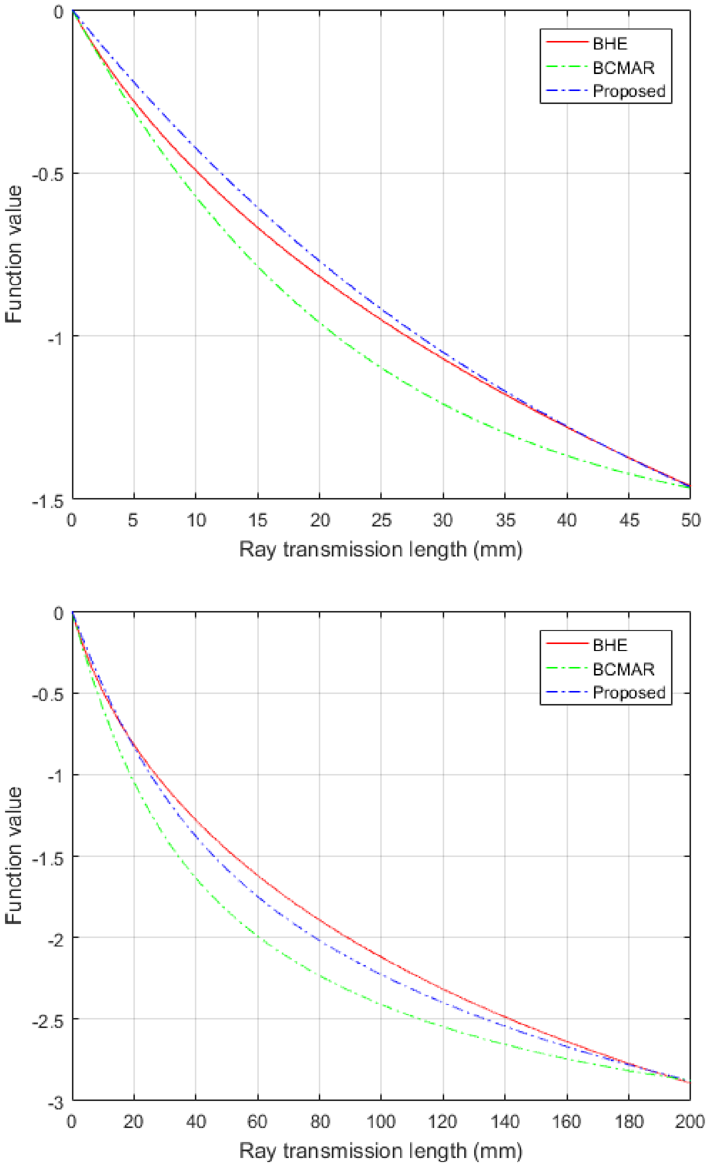

Figure 5.8 Comparison between BHE, BCMAR, and proposed model when the ray transmission length is less than 50 mm (top) and 200 mm (bottom) for Cortical bone.

5.2.2 Robustness

The proposed method was applied to two software phantoms: JawSimulationPhantom1 and JawSimulationPhantom2. Fig. 5.9 and 5.10 show the results of the metal artifact reduction for each phantom with Cu, Fe, and Ti. For comparison, we generated ground-truth images as reference (Fig. 5.9 and 5.10, first column). From top, the ground-truth with only teeth, the phantom with copper implants, the phantom with iron implants, and the phantom with titanium implants are shown. The first column shows the uncorrected images, and the second column shows the corrected images. All the results show that the artifacts with white streaks and dark shadow bands are clearly removed and the morphological information obscured by the artifacts is fully revealed.

The proposed method was also applied to two hardware phantoms: TriTiPhantom and JawEquivPhantom. Figs. 5.11 and 5.12 are 3D rendered images of the each metal region and these were blended with the each transparent overall volume. The metal regions were segmented by the thresholding technique. Figs. 5.13 and 5.14 show the results obtained using the proposed method. Since JawEquivPhantom consists of two types of metals, $\Re^{-1}(\tilde{\psi}_1)$ and $\Re^{-1}(\tilde{\psi}_2)$ show the summed image of each metal's. From left, each column shows the uncorrected image and the corrected image in top row, $\Re^{-1}(\tilde{\psi}_1)$ and $\Re^{-1}(\tilde{\psi}_2)$ in bottom row. It shows that the estimator $\Re^{-1}(\tilde{\psi}_1)$ and $\Re^{-1}(\tilde{\psi}_2)$ each appropriately express the artifacts caused by beam-hardening. However, it can be seen that artifacts were generated not only by metals, but also by a large bone in the results of JawEquivPhantom.

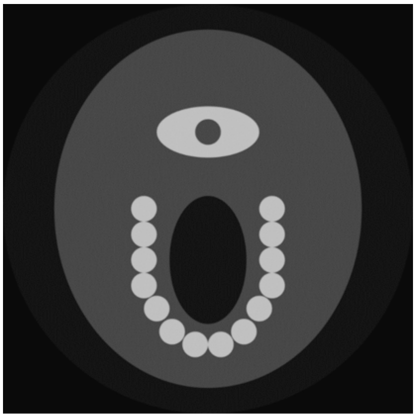

(a)

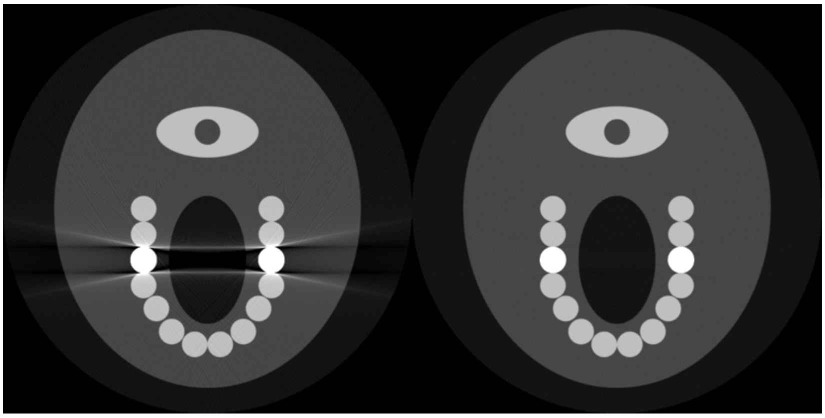

(b)

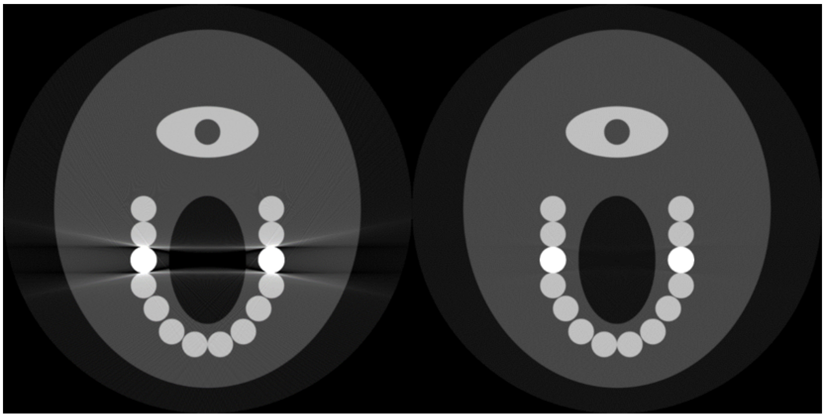

(c)

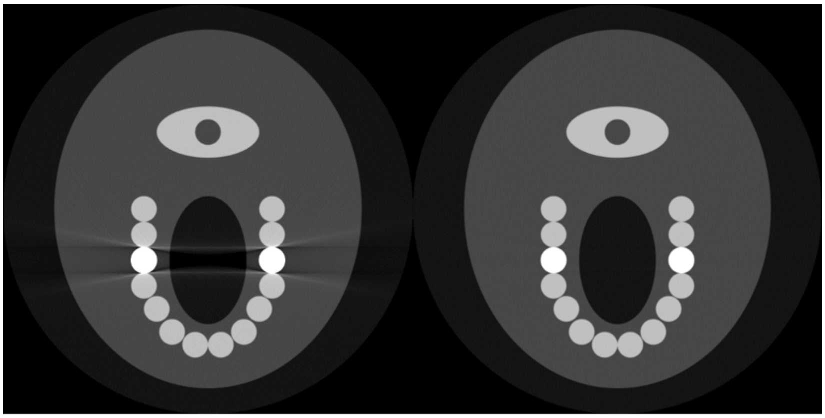

(d)

Figure 5.9 Numerical simulation phantom (JawSimulationPhantom1) with 2 metallic implants. (a) No metal (b) Cu (c) Fe (d) Ti. These images are displayed at window (center and width) settings of (750, 2500) HU.

(a)

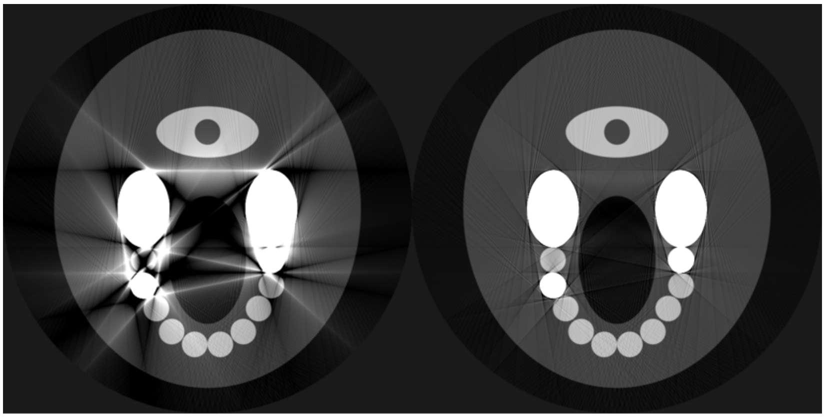

(b)

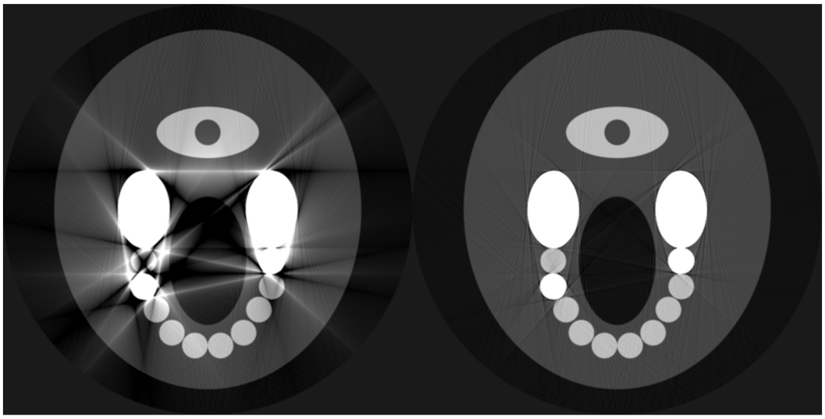

(c)

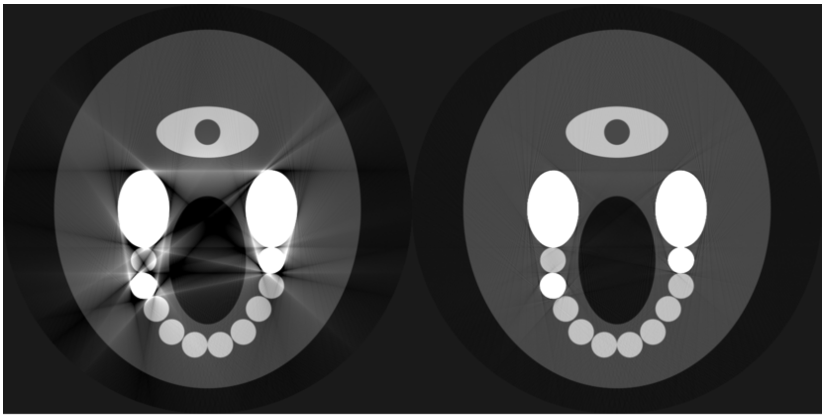

(d)

Figure 5.10 Numerical simulation phantom (JawSimulationPhantom2) with 4 metallic implants. (a) No metal (b) Cu (c) Fe (d) Ti. These images are displayed at window (center and width) settings of (750, 2500) HU.

Figure 5.11 3D visualization of the segmented metal volume for TriTiPhantom. It is blended with the transparent overall volume.

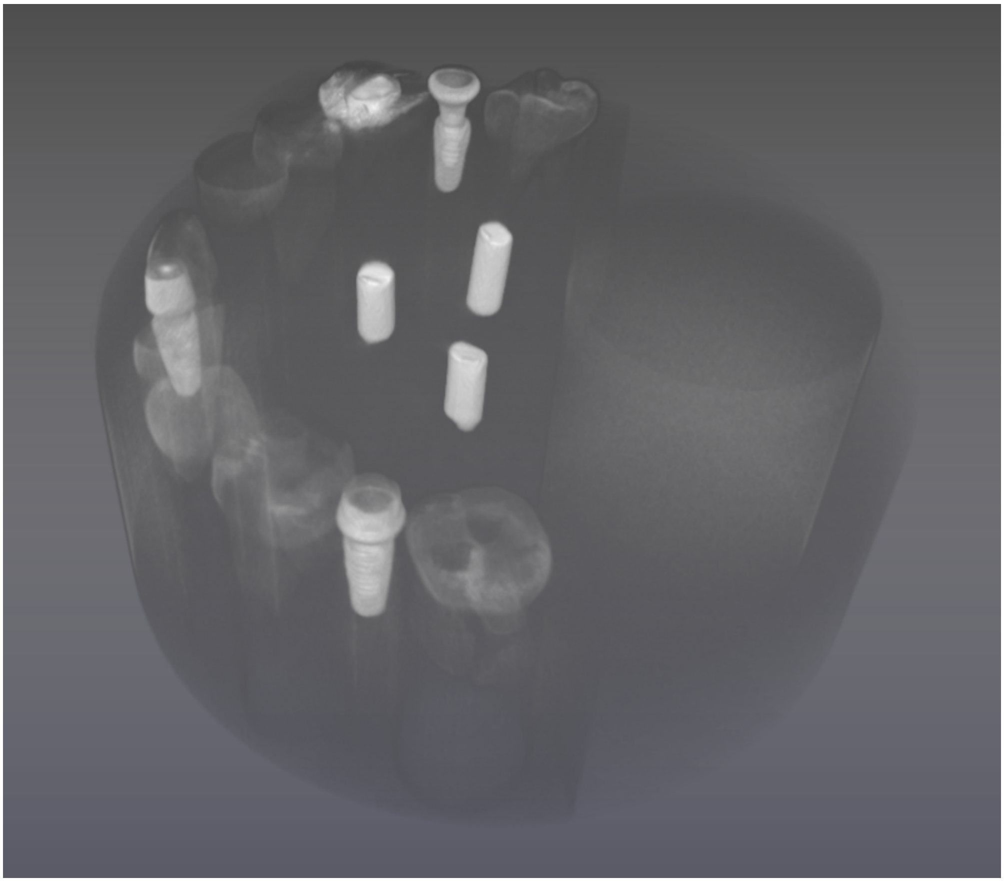

Figure 5.12 3D visualization of the segmented metal volume for JawEquivPhantom. It is blended with the transparent overall volume.

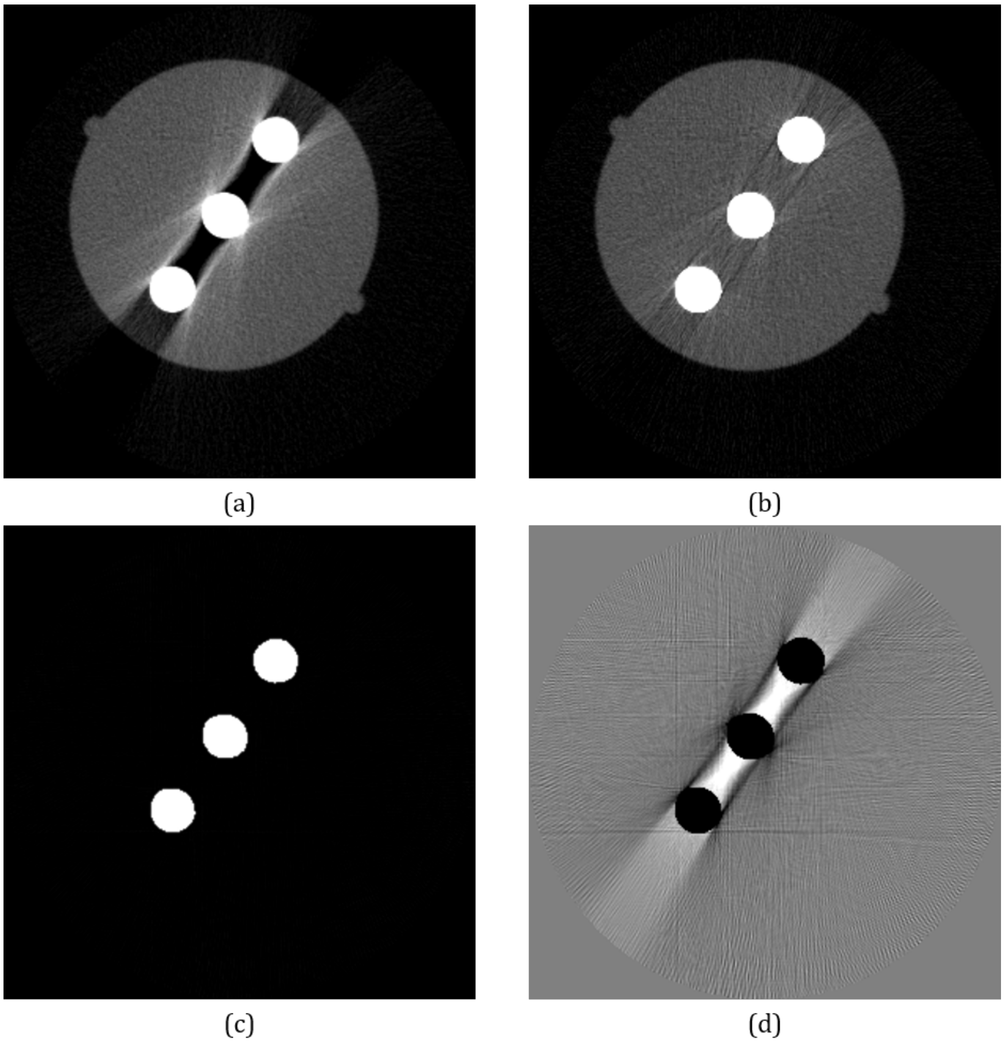

Figure 5.13 TriTiPhantom (a) Uncorrected (b) Corrected (c) $\Re^{-1}(\tilde{\psi}_1)$ (d) $\Re^{-1}(\tilde{\psi}_2)$. These images are displayed at window (center and width) settings of (500, 2000) HU.

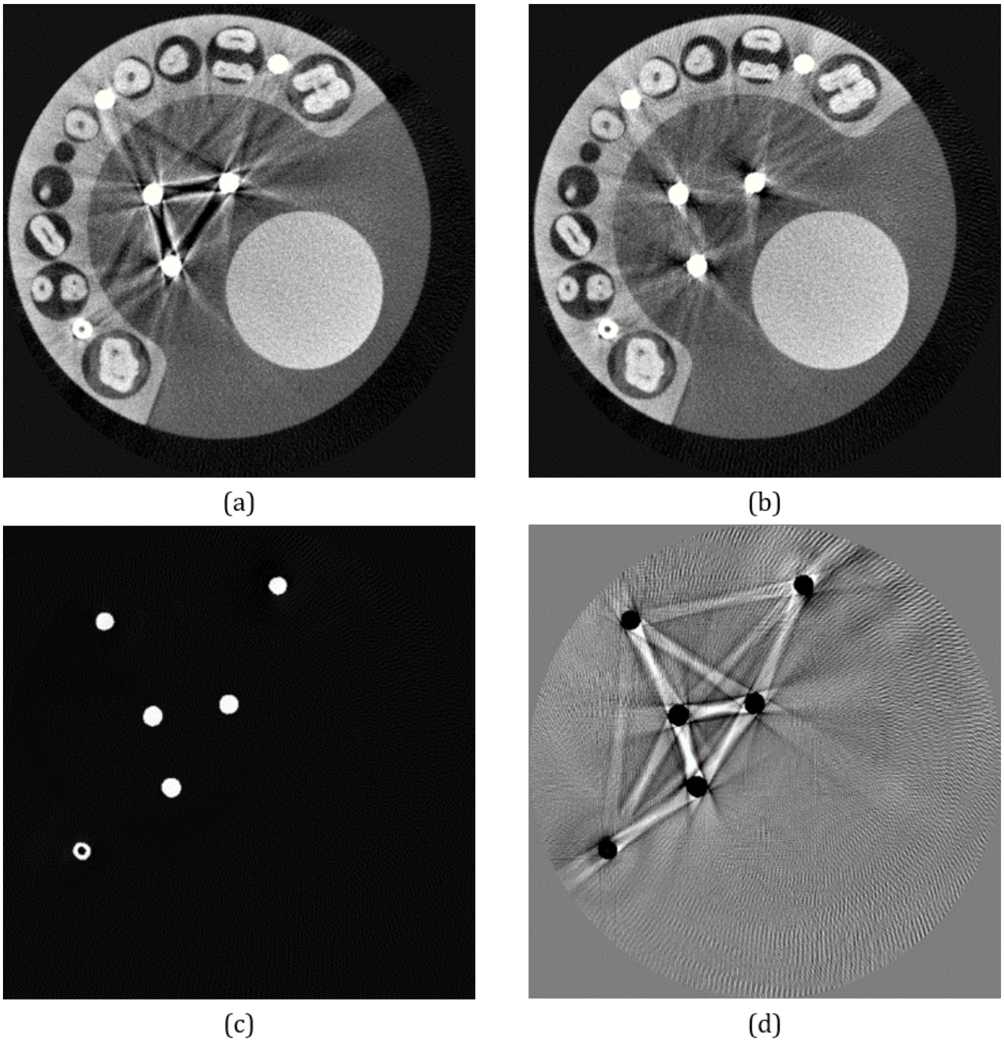

Figure 5.14 JawEquivPhantom (a) Uncorrected (b) Corrected (c) $\Re^{-1}(\tilde{\psi}_1)$ (d) $\Re^{-1}(\tilde{\psi}_2)$. These images are displayed at window (center and width) settings of (500, 2000) HU.

5.3 Performance evaluations

5.3.1 Evaluation with simulated phantoms

Figs. 5.15 and 5.16 compares LIMAR, NMAR, BCMAR, and the proposed method for the JawSimulationPhantom1 and the JawSimulationPhantom2 with Cu implants. From top, the uncorrected image, LIMAR result, NMAR result, BCMAR result, and the result of the proposed method are shown. The first column shows the results of each method, and the second column shows the difference images for each result with respect to the ground-truth. The reconstruction images are displayed at window (center and width) settings of (125, 1000) HU and the difference images are displayed at window (center and width) settings of (125, 250) HU. All methods except FDK reduced the beam-hardening artifacts shown in the uncorrected image. However, in the case of LIMAR, it lost morphological information around the metal region, and secondary artifacts are newly introduced. The artifacts were significantly suppressed in images reconstructed by NMAR, which uses the prior image for normalization and denormalization along with pure interpolation as in LIMAR. Tables 5.1 and 5.2 list the quality (NRMSD) and speed (time) of each method. NMAR yielded a lower NRMSD compared to LIMAR and BCMAR. Additionally, because NMAR requires projection data of the prior image, it incurs additional computational costs over LIMAR. The proposed method shows the best quality and better speed than BCMAR, owing to the lower number of iterations of FBP.

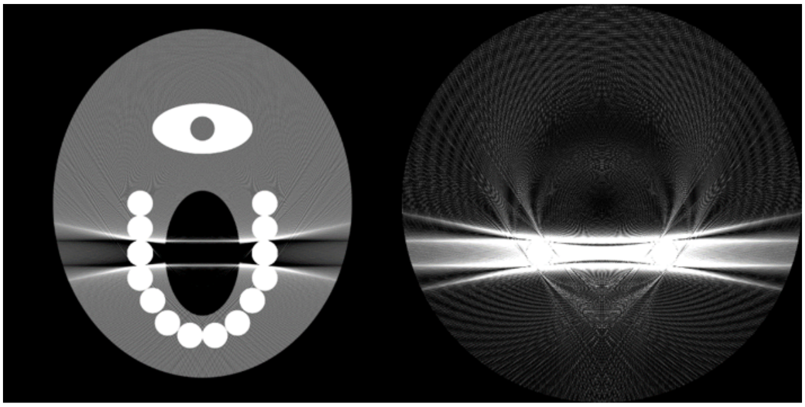

(a)

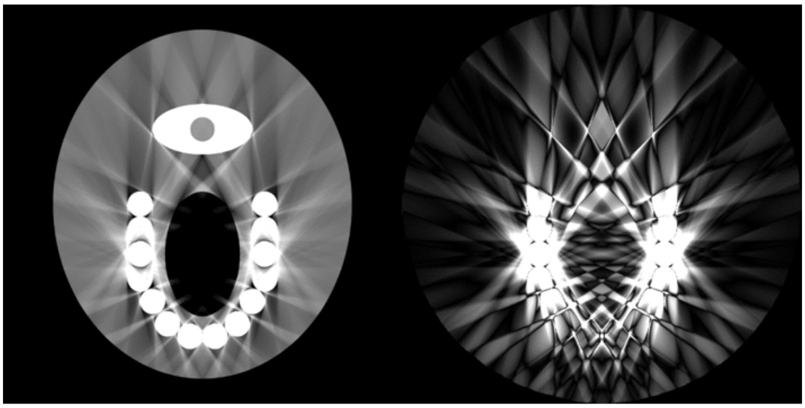

(b)

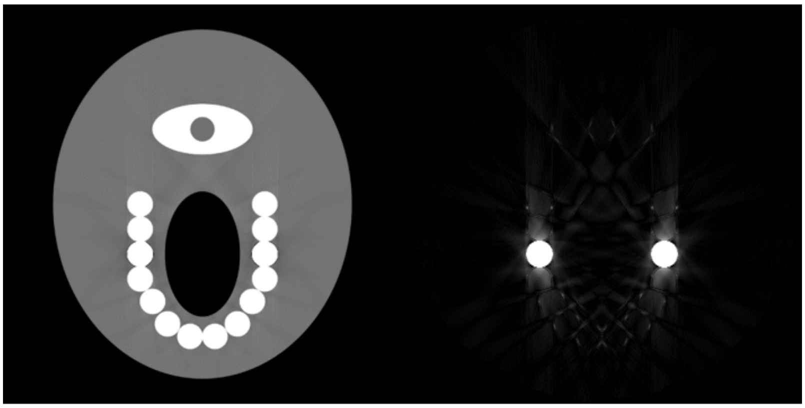

(c)

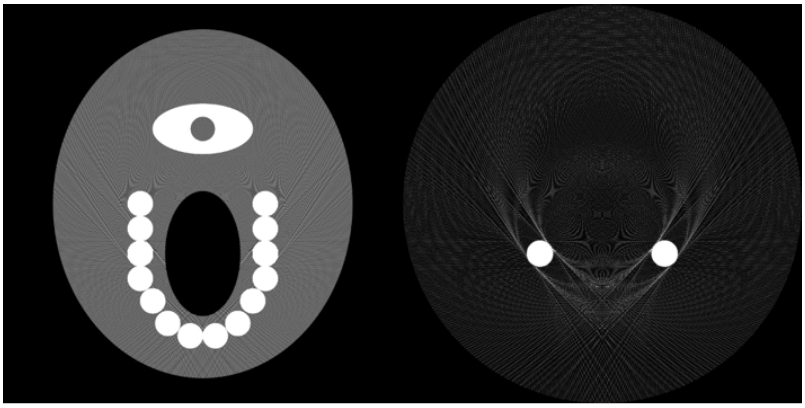

(d)

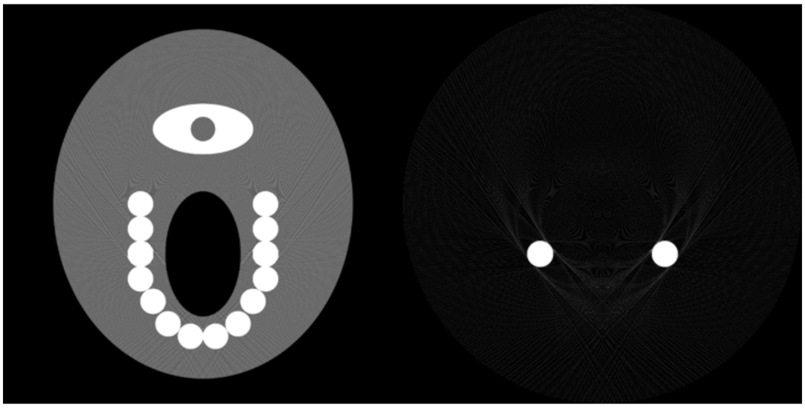

(e)

Figure 5.15 Comparison among LIMAR, NMAR, BCMAR, and the proposed method for the JawSimulationPhantom1 (Cu). (a) Uncorrected (b) LIMAR (c) NMAR (d) BCMAR (e) Proposed. The left is the result image of each method and the right is the difference image from the ground-truth. The left images are displayed at window (center and width) settings of (125, 1000) HU and the right images are displayed at window settings of (125, 250) HU.

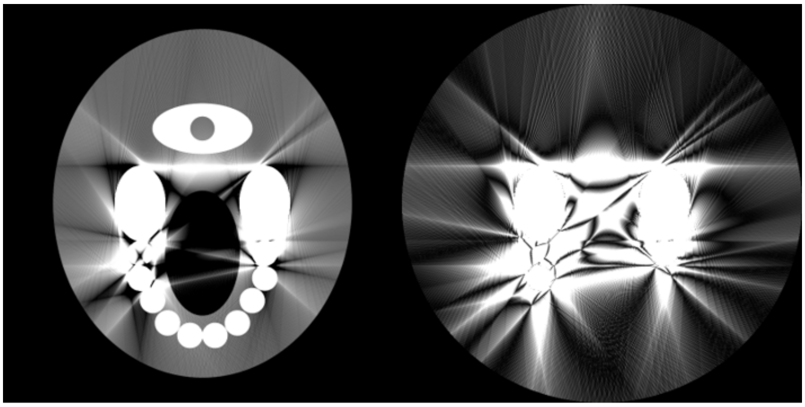

(a)

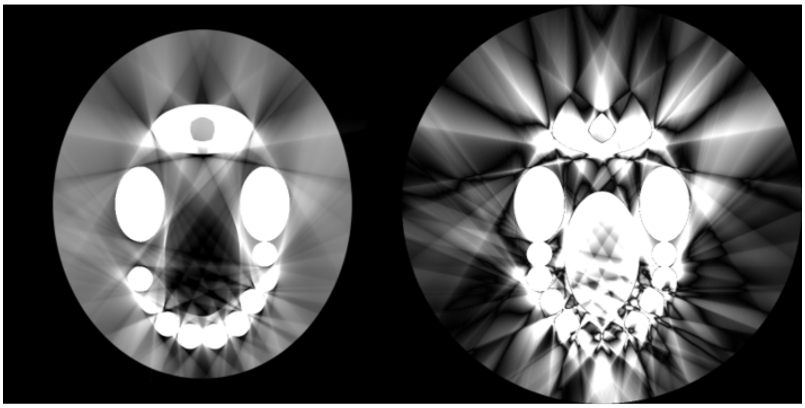

(b)

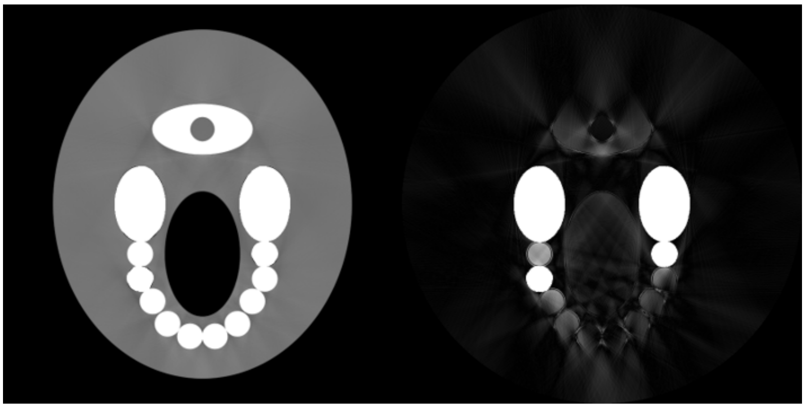

(c)

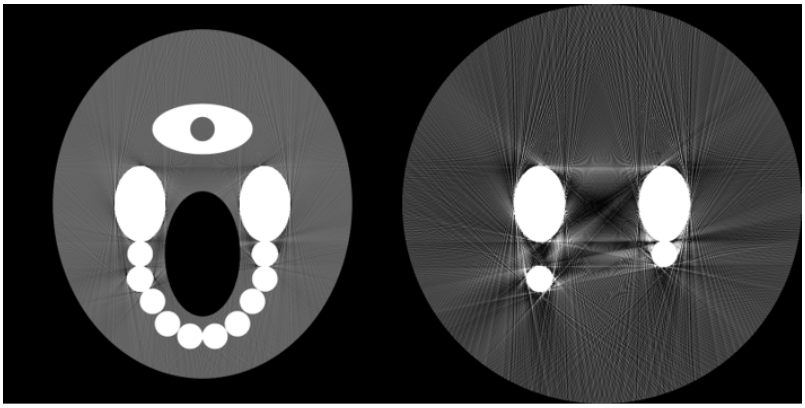

(d)

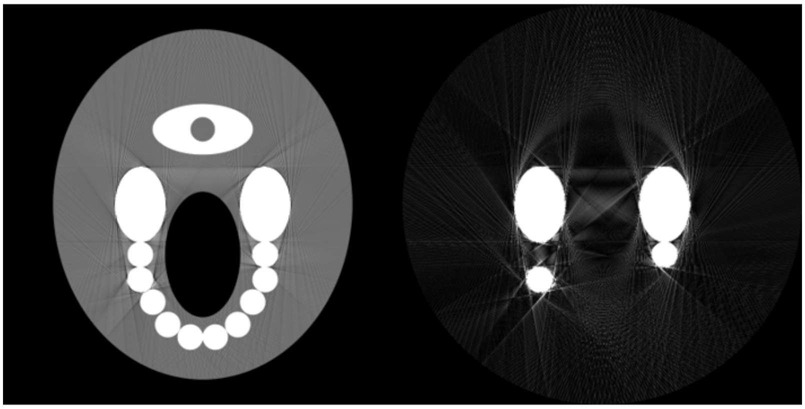

(e)

Figure 5.16 Comparison among LIMAR, NMAR, BCMAR, and the proposed method for the JawSimulationPhantom2 (Cu). (a) Uncorrected (b) LIMAR (c) NMAR (d) BCMAR (e) Proposed. The left is the result image of each method and the right is the difference image from the ground-truth. The left images are displayed at window (center and width) settings of (125, 1000) HU and the right images are displayed at window settings of (125, 250) HU.

Methods	Uncorrected	LIMAR	NMAR	BCMAR	Proposed
NRMSD (%)	23.40	20.39	8.81	14.39	3.13
Time (sec)	2.62	5.39	5.86	35.57	8.73
# of FBP	1	2	2	11	3

Table 5.1 Quantitative evaluation of the MAR methods for ROI of JawSimulationPhantom1

Methods	Uncorrected	LIMAR	NMAR	BCMAR	Proposed
NRMSD (%)	34.78	32.77	13.39	16.60	6.10
Time (sec)	2.83	5.53	5.97	39.34	8.86
# of FBP	1	2	2	12	3

Table 5.2 Quantitative evaluation of the MAR methods for ROI of JawSimulationPhantom2

5.3.2 Evaluation with hardware phantoms

Figs. 5.17 and 5.18 show the results of comparison among LIMAR, NMAR, BCMAR, and the proposed method for TriTiPhantom and JawEquivPhantom respectively. Top row shows the uncorrected image, middle row shows the results of LIMAR and NMAR, and bottom row shows the results of BCMAR and the proposed method. Tables 5.3 and 5.4 list the quantitative results of each method as other metrics. MAD was calculated on the ROI (the red box in Figs. 5.17 and 5.18) by referring to the homogeneous rROI of the uncorrected image (the yellow box in Figs. 5.17 and 5.18). In both results, the proposed method shows a slightly better quality than BCMAR. CNR was calculated on the red and blue circles in Fig. 5.19 (the blue box in Fig. 5.18). The results of LIMAR and NMAR showed lower MAD values than BCMAR and the proposed method. On the other hand, the CNR values for LIMAR and NMAR were lower than that of the uncorrected CT. As the number of metal types involved increased, the number of FBP operations to be performed increased, leading to an increase in the execution time of BCMAR and the proposed method.

Methods	Uncorrected	LIMAR	NMAR	BCMAR	Proposed
MAD (HU)	469.99	48.24	52.20	109.60	97.89
Time (sec)	3.91	8.63	9.17	43.41	10.49
# of FBP	1	2	2	11	3

Table 5.3 Quantitative evaluation of the MAR methods for ROI of TriTiPhantom

Methods	Uncorrected	LIMAR	NMAR	BCMAR	Proposed
MAD (HU)	482.16	121.69	131.80	326.24	325.37
Time (sec)	4.43	12.03	12.85	134.31	32.56
# of FBP	1	2	2	21	5
CNR	13.69	7.05	6.04	15.28	15.75

Table 5.4 Quantitative evaluation of the MAR methods for ROI of JawEquivPhantom

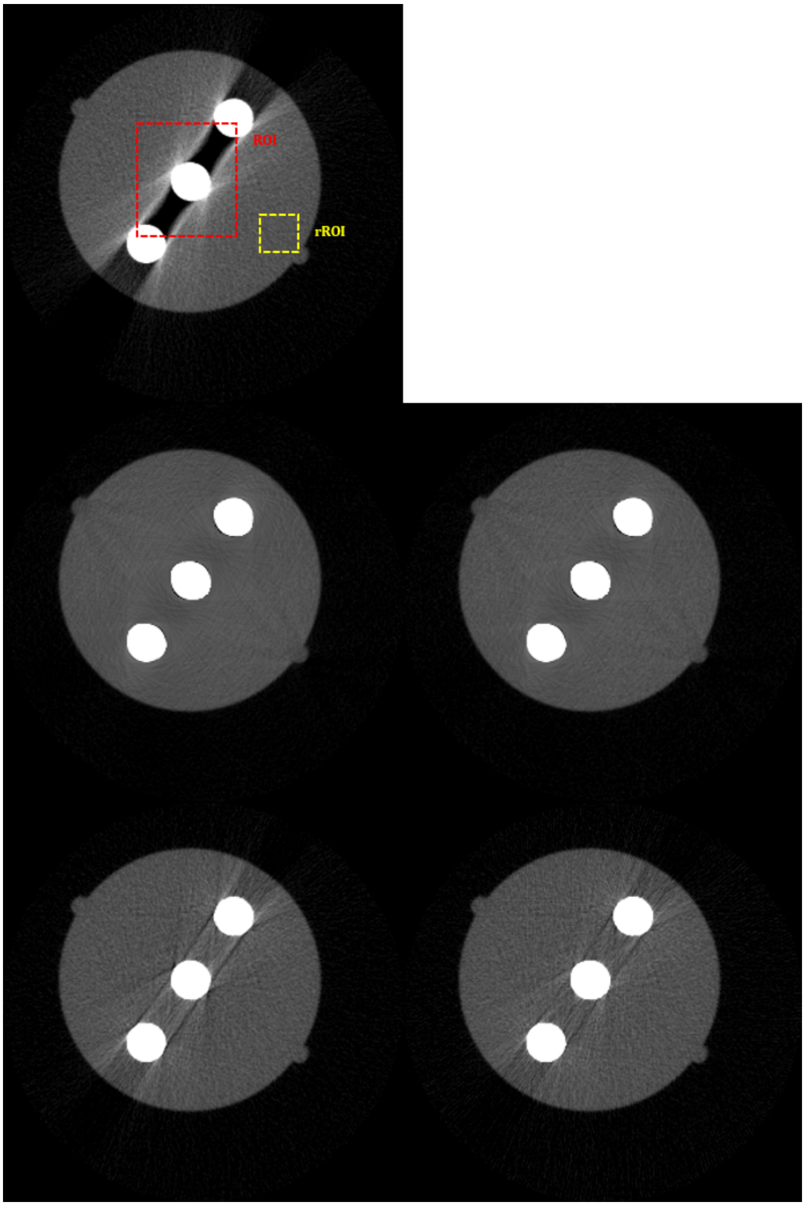

Figure 5.17 Comparison among LIMAR, NMAR, BCMAR, and the proposed method for TriTiPhantom. These images are displayed at window (center and width) settings of (500, 2000) HU.

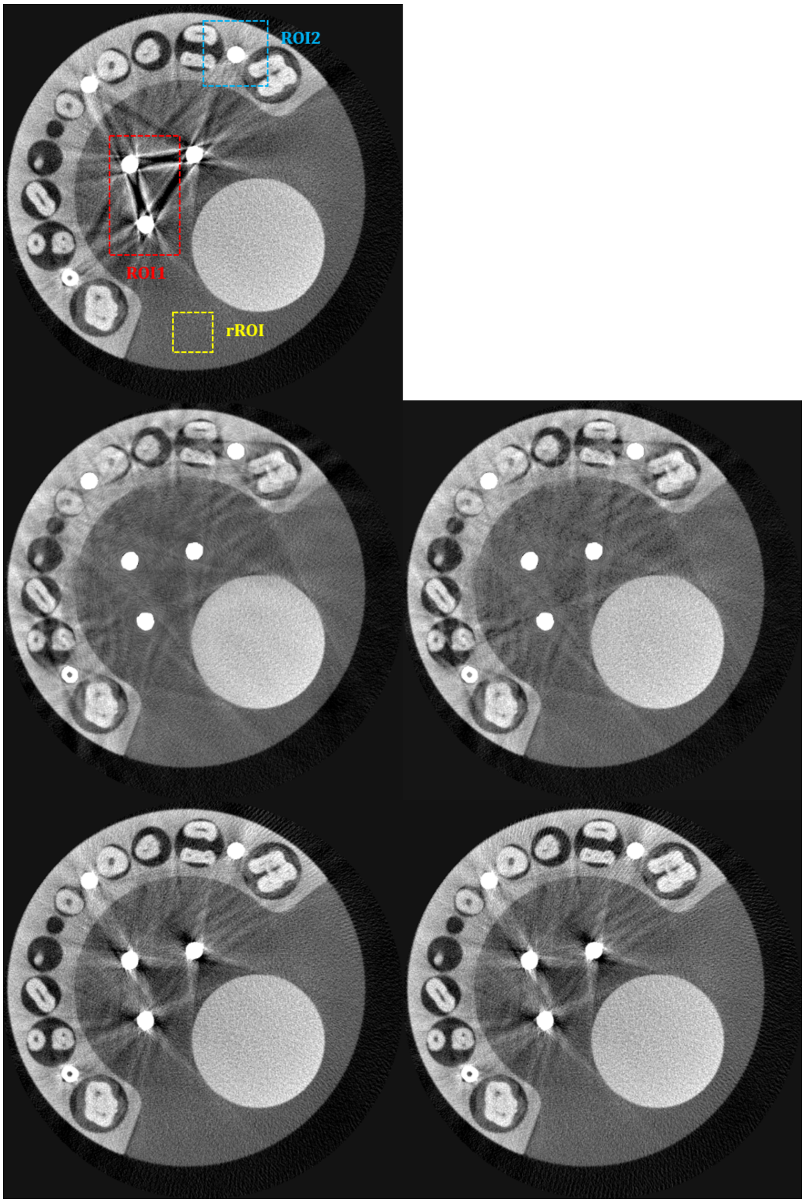

Figure 5.18 Comparison among LIMAR, NMAR, BCMAR, and the proposed method for JawEquivPhantom. These images are displayed at window (center and width) settings of (500, 2000) HU.

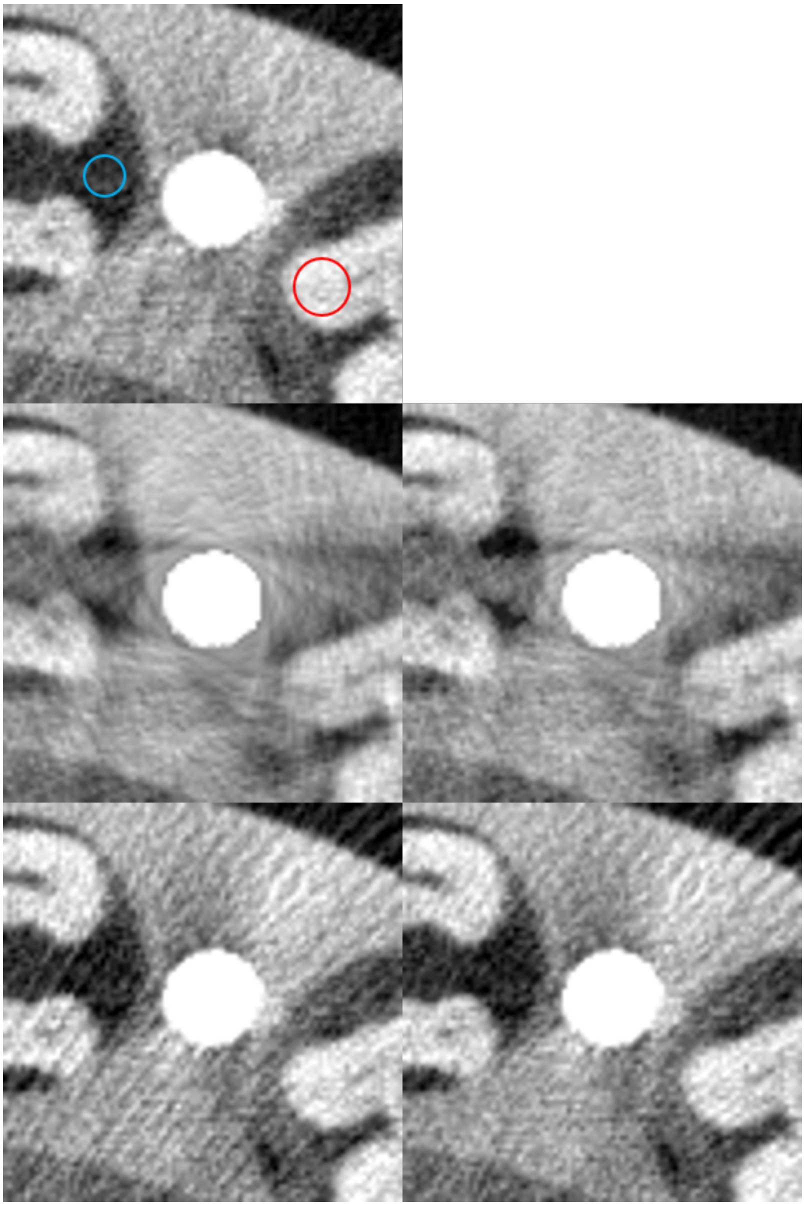

Figure 5.19 Zoomed images for the ROI2 (the blue box) of JawEquivPhantom. These images are displayed at window (center and width) settings of (500, 2000) HU.

5.3.3 Evaluation on refinement methods

Fig. 5.20 shows results of the collaboration between the proposed MAR method and ADN. As shown in Fig. 5.21 (b) and (c), only a very small amount of artifacts were reduced by ADN compared to the proposed MAR method and the metal regions were eroded slightly. The cooperation of the two methods (Refinement1) shows a significantly improved result. As compared to the result of the proposed MAR method (5.21 (c)), the dark shadows and some white streaks around the metal in the center were reduced greatly (Fig. 5.21 (d)), but it also shows the erosion in metal regions. Fig. 5.22 shows the result of CBHE application to bone area (Refinement2) that has been much improved than any previous results.

Methods	Uncorrected	ADN	Proposed	Refinement1	Refinement2
MAD (HU)	482.16	408.37	325.37	180.72	165.49
# of FBP	1	1	5	5	6
CNR	13.69	12.74	15.75	15.54	15.04

Table 5.5 Quantitative evaluation on the refinement methods - Refinement1 and Refinement2 - for ROI of JawEquivPhantom

The quantitative results are provided in Table 5.5. The Refinement1 shows a 44.5% improvement over the proposed MAR method and a 55.7% improvement over the ADN method in terms of MAD. The Refinement2 has a 49.1% improvement over the proposed MAR method. On the other hand, the CNR was worse compared to the proposed method. It was reduced by 1.3% for Refinement1 and 4.5% for Refinement2. Consequently, adding a refinement process to the proposed CBHE method led to less residual artifacts around the metal.

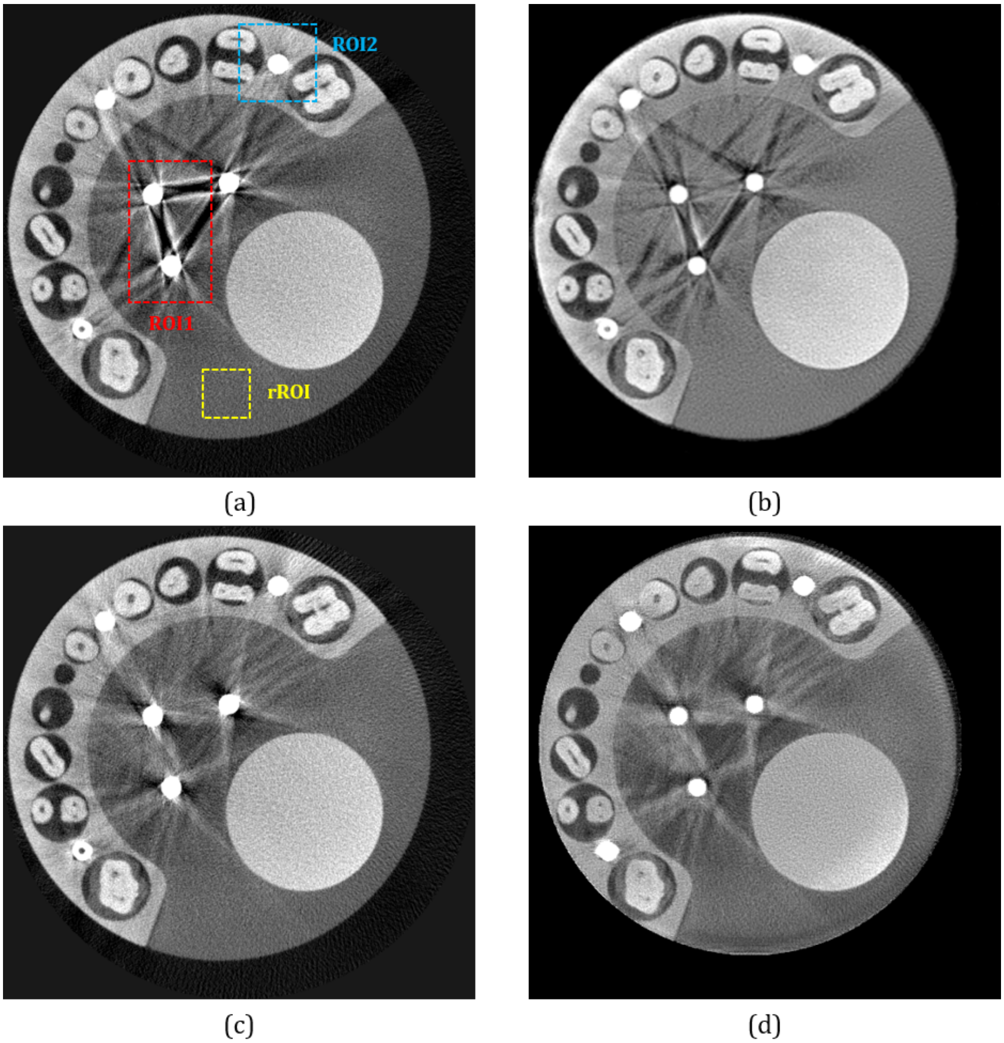

Figure 5.20 Comparison among ADN, the proposed, and the collaboration with ADN for JawEquivPhantom. (a) Uncorrected (b) ADN (c) Proposed (d) Refinement1.

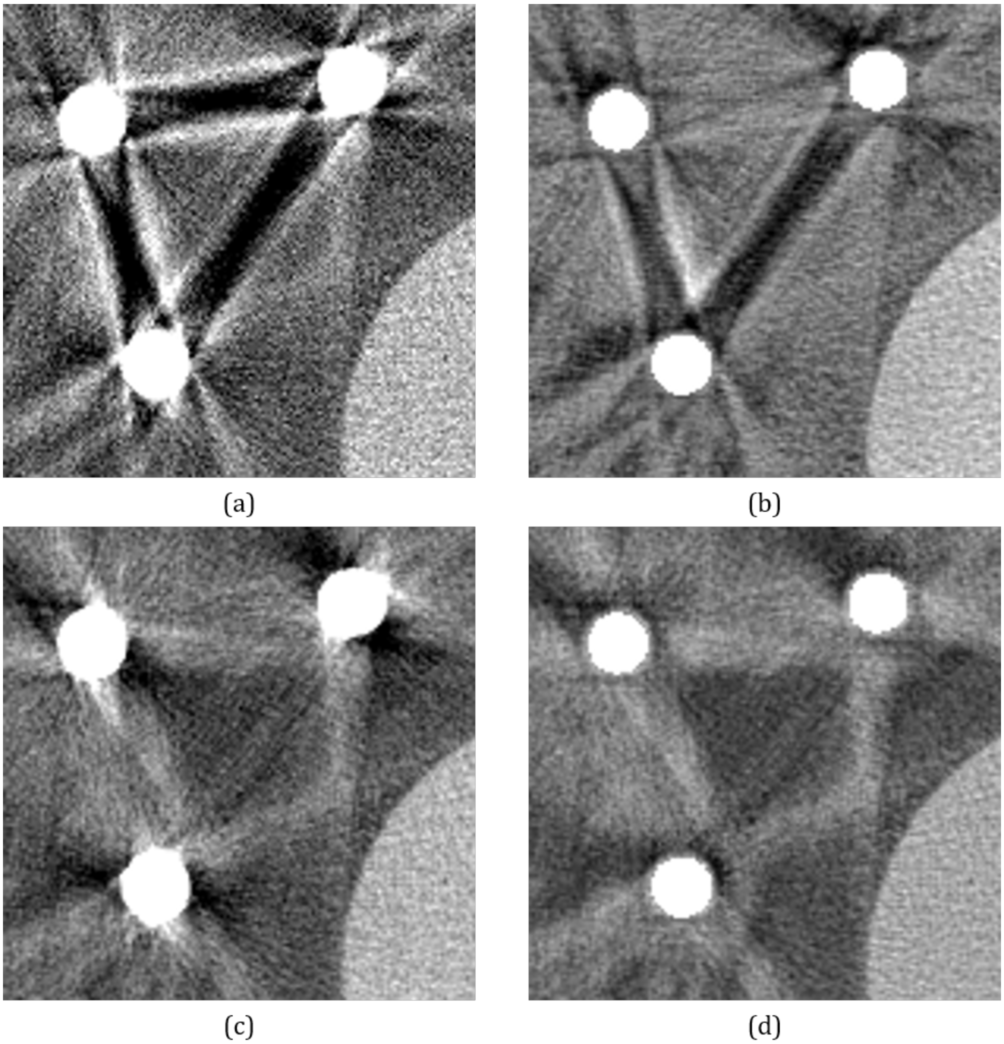

Figure 5.21 Zoomed images of Fig. 20. (a) Uncorrected (b) ADN (c) Proposed (d) Refinement1.

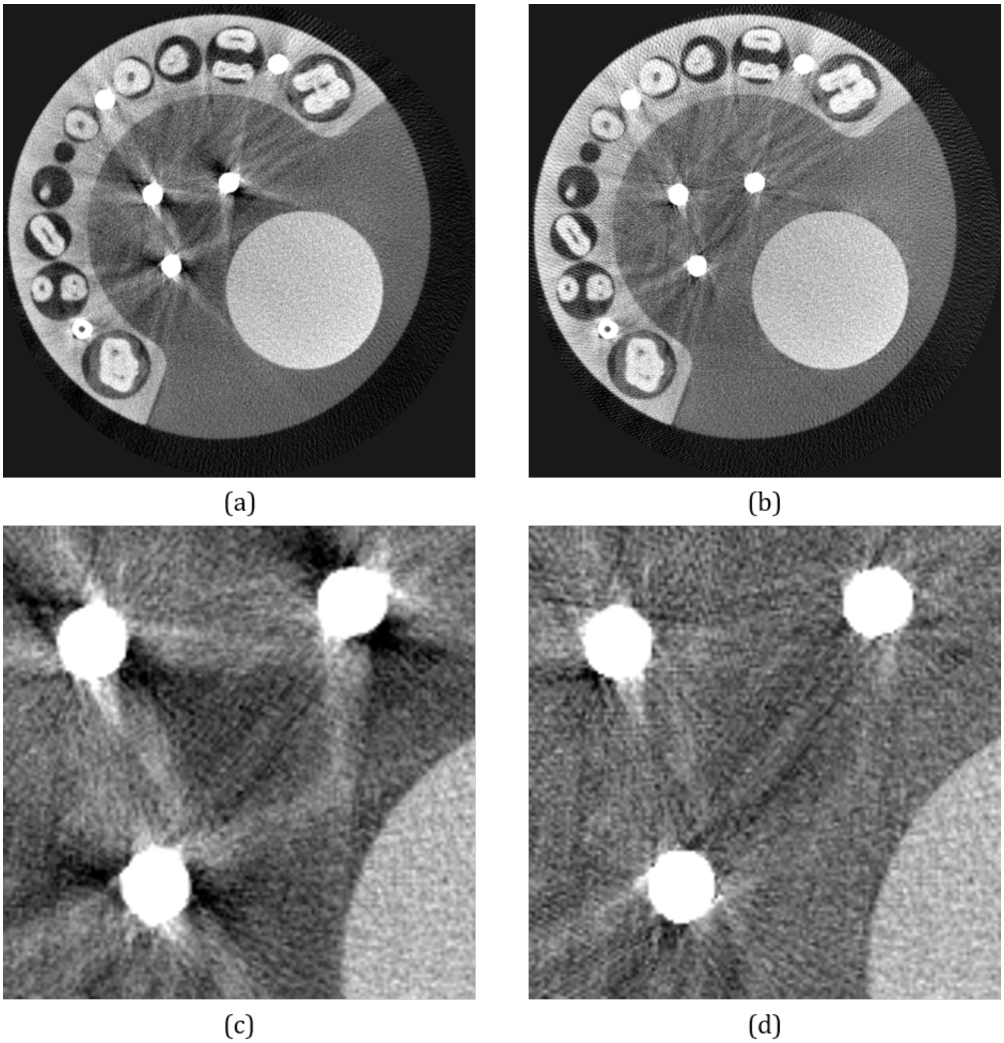

Figure 5.22 Comparison among the proposed and the application of CBHE to bone for JawEquivPhantom. (a) Proposed (b) Refinement2 (c) Zoomed image of Proposed (d) Zoomed image of Refinement2.

Chapter 6

Conclusion

This study proposed an efficient numerical solution based on the constrained beam-hardening estimator with X-ray transmission length. This estimator reflects the geometry of metal objects and the physical characteristics of beam-hardening during the transmission of polychromatic X-rays through a material. Numerical methods have been proposed for effectively reducing metal artifacts through a mathematical correction model of beam-hardening. However, because they are based on the iterative reconstruction framework to find model-associated unknown parameters via an analysis of the mismatch between measured and expected sinograms, they incur a heavy computation burden. In contrast, the proposed method identifies the model-associated unknown parameter α using linear optimization, which is performed only on the reconstruction image domain without forward and backward projections. This computational structure achieves a linear combination of two images reconstructed only once during the entire process, thereby reducing time-consuming loops on the projection domain. This finding is in sharp contrast to previous numerical works and is important for practical use in clinical applications.

The type of metal is not explicitly addressed in our method. Reconstructions for JawEquivPhantom demonstrated that the proposed beam-hardening estimator can be applied to cases containing metallic objects of several types by performing MAR separately for each metal. In the proposed method, K-edge characteristics associated with the sudden attenuation increase in the energy spectrum were not considered because the effect was insignificant. Experimenting with a variety of metal materials showed that there were no issues in the spectrum including K-edge characteristics.

The image quality of the volumetric CBCT image performed using the proposed method was similar or superior to that of the sinogram inpainting-based and model-based approaches without losing morphological information locally. The quantitative analysis using NRMSD, MAD, and CNR calculations has substantiated the increased quality observed in the reconstruction images. LIMAR and NMAR exhibited better MAD values for TriTiPhantom and JawEquivPhantom, but they had lower CNR values because they lost the anatomical shape around the metal area. The performance of NMAR depends greatly on the quality of the prior image. An important step is to model a good prior image that is as close as possible to the ground truth. In the experiment with JawSimulationPhantom1 and JawSimulationPhantom2, the generation of a prior image comparable to the ground truth was achieved because simple thresholding made it possible to segment air, soft tissue, and bone easily. This led to a theoretically perfect result. In contrast, in the other two experiments that involved incomplete prior images from artifact affected images, the performance was degraded. The proposed scheme showed substantially superior results in terms of the computation time as compared with BCMAR [8]. The developed method has a great significance in that it successfully yields the analytical reconstruction structure while retaining superior performance in the quality of the iterative reconstruction-type model-based correction scheme.

Although the developed method can reduce most metal artifacts, better results can be expected if the X-ray spectrum and more attenuation coefficients of metallic materials are provided in advance. As an alternative, an acquisition method based on reconstructed CT images is also an effective option. We have proposed two refinement methods - collaborating with ADN model and applying CBHE to bone. As a post-processing, ADN is a superb partner to complement each other's drawbacks and improve the quality of results. The proposed method is useful for efficiently obtaining pairs of anatomically identical CT images with and without metal artifacts, which can be used for training in deep-learning-based MAR approaches. The application of CBHE to bone reduces the remaining artifacts more clearly than ADN. However, it requires to segment the target bone area that is not much simple than metal segmentation, and performs more reconstructions like the artifact estimation for multiple types of metallic objects.

The proposed constrained beam-hardening estimator has a few practical considerations. First, our method assumed that the accurate geometry of a metal region is given, as in other correction-based MAR methods. Although the metal segmentation is a key factor in determining the performance of the algorithm, we did not strictly consider it in this study because we focused more on how to correct for a given metal area than on how to segment the metal area. We used threshold-based segmentation to extract the metal area in the case where no reference image is given [5]. Accurate segmentation is still an open problem, and a variety of segmentation techniques [24, 39, 82, 83] can be considered. In clinical CT, various types and shapes of metallic inserts are included. Further research to extract exact geometry is necessary to deal with them. Second, although suitable alternatives for parameters are presented, additional information such as the X-ray spectrum and X-ray mass attenuation coefficients [3] may further improve performance. In the present experiments, the difference between the maximum and the minimum values of the metal region was used for β. An appropriate scaling to it was employed since the value was small relative to the ideal value of β. Third, as the constrained beam-hardening estimator was considered in a homogeneous metallic material, each type of metal should be dealt with separately. The number of metal types is directly related to the calculation time. Fourth, beam-hardening from a considerably dense target such as bone may result in streak and shadow artifacts. In the JawEquivPhantom results, residual artifacts still existed around three rods near the center owing to the metal rods and the large bone. If the bone is sufficiently large, since beam-hardening cannot be neglected, we may refine the result by adding bone segmentation in a manner similar to metal segmentation (Fig. 4.8). Fifth, as shown in Figs. 5.6 and 5.7, the BHE curve has a form that converges as the metal length increases while the proposed model has a form that does not converge and continues to diverge because of a logarithm term such as (3.12). The proposed model depending on only one parameter adjustment may have difficulties in fitting when the metal length exceeds a certain range. On the other hand, the proposed model with the appropriate choice of α

can be a good approximation of BHE for a reasonable range of 50 mm regardless of the type of metal.

In this dissertation, we have developed a novel beam-hardening estimator for MAR when using polychromatic X-rays and have validated its performance through numerous phantom studies. The method is derived from a polychromatic X-ray attenuation model with respect to the X-ray transmission length and an unknown parameter α that is identified by solving a linear optimization problem. This method enables faster MAR than existing beam-hardening correction methods. It also effectively reflects the characteristics of the beam-hardening and successfully reduces metal artifacts. We also suggest two ways of refining the proposed MAR method by reducing residual artifacts.

A natural suggestion for future research is to further improve the valid range of the proposed CBHE. Analyzing the experimental results, it can be seen that the higher the density of the material, the narrower the valid range. One possible approach is to analyze the correlation between the density of a substance and the valid range of it. An improved model could be established from the analysis and it would have more significant implications in improving dose calculation accuracy or target volume delineation.

Bibliography

[1] L. Gerward, N. Guilbert, K. B. Jensen, and H. Levring, "X-ray absorption in matter. reengineering xcom," *Radiation Physics and Chemistry*, vol. 60, no. 1-2, pp. 23–24, 2001.

[2] J. Hsieh, *Computed tomography: principles, design, artifacts, and recent advances.* SPIE Press, 2003, vol. 114.

[3] J. Hubbell and S. Seltzer, "Tables of x-ray mass attenuation coefficients and mass energy-absorption coefficients," *National Institute of Standards and Technology, Gaithersburg, MD*, 2004. [Online]. Available: http://physics.nist.gov/xaamdi

[4] M. B. G. d. Silva and E. F. Sant'Anna, "The evolution of cephalometric diagnosis in orthodontics," *Dental press journal of orthodontics*, vol. 18, no. 3, pp. 63–71, 2013.

[5] E. Meyer, R. Raupach, M. Lell, B. Schmidt, and M. Kachelrieß, "Normalized metal artifact reduction (nmar) in computed tomography," *Medical Physics*, vol. 37, no. 10, pp. 5482–5493, 2010.

[6] X. Duan, L. Zhang, Y. Xiao, J. Cheng, Z. Chen, and Y. Xing, "Metal artifact reduction in ct images by sinogram tv inpainting," in *2008 IEEE Nuclear Science Symposium Conference Record.* IEEE, 2008, pp. 4175–4177.

[7] Y. Li, X. Bao, X. Yin, Y. Chen, L. Luo, and W. Chen, "Metal artifact reduction in ct based on adaptive steering filter and nonlocal sinogram inpainting," in *2010 3rd International Conference on Biomedical Engineering and Informatics*, vol. 1. IEEE, 2010, pp. 380–383.

[8] H. S. Park, D. Hwang, and J. K. Seo, "Metal artifact reduction for polychromatic x-ray ct based on a beam-hardening corrector," *IEEE Transactions on Medical Imaging*, vol. 35, no. 2, pp. 480–487, 2015.

[9] H. Shi, Z. Yang, and S. Luo, "Reduce beam hardening artifacts of polychromatic x-ray computed tomography by an iterative approximation approach," *Journal of X-ray Science and Technology*, vol. 25, no. 3, pp. 417–428, 2017.

[10] A. C. Kak and M. Slaney, *Principles of Computerized Tomographic Imaging.* IEEE Press, 1988.

[11] R. N. Bracewell and A. Riddle, "Inversion of fan-beam scans in radio astronomy," *The Astrophysical Journal*, vol. 150, p. 427, 1967.

[12] J. Radon, "On the determination of functions from their integral values along certain manifolds," *IEEE Transactions on Medical Imaging*, vol. 5, no. 4, pp. 170–176, 1986.

[13] B. De Man, J. Nuyts, P. Dupont, G. Marchal, and P. Suetens, "Metal streak artifacts in x-ray computed tomography: a simulation study," *IEEE Transactions on Nuclear Science*, vol. 46, no. 3, pp. 691–696, 1999.

[14] J. F. Barrett and N. Keat, "Artifacts in ct: recognition and avoidance," *Radiographics*, vol. 24, no. 6, pp. 1679–1691, 2004.

[15] R. A. Brooks and G. Di Chiro, "Beam hardening in x-ray reconstructive tomography," *Physics in medicine & biology*, vol. 21, no. 3, p. 390, 1976.

[16] H. S. Park, Y. E. Chung, and J. K. Seo, "Computed tomographic beam-hardening artefacts: mathematical characterization and analysis," *Philosophical Transactions of the Royal Society A: Mathematical, Physical and Engineering Sciences*, vol. 373, no. 2043, p. 20140388, 2015.

[17] D. Giantsoudi, B. De Man, J. Verburg, A. Trofimov, Y. Jin, G. Wang, L. Gjesteby, and H. Paganetti, "Metal artifacts in computed tomography for radiation therapy planning: dosimetric effects and impact of metal artifact reduction," *Physics in Medicine & Biology*, vol. 62, no. 8, p. R49, 2017.

[18] L. Gjesteby, B. De Man, Y. Jin, H. Paganetti, J. Verburg, D. Giantsoudi, and G. Wang, "Metal artifact reduction in ct: where are we after four decades?" *IEEE Access*, vol. 4, pp. 5826–5849, 2016.

[19] G. H. Glover and N. J. Pelc, "An algorithm for the reduction of metal clip artifacts in ct reconstructions," *Medical Physics*, vol. 8, no. 6, pp. 799–807, 1981.

[20] W. A. Kalender, R. Hebel, and J. Ebersberger, "Reduction of ct artifacts caused by metallic implants." *Radiology*, vol. 164, no. 2, pp. 576–577, 1987.

[21] J. L. Prince and A. S. Willsky, "Constrained sinogram restoration for limited-angle tomography," *Optical Engineering*, vol. 29, no. 5, pp. 535–545, 1990.

[22] S. Zhao, D. Robeltson, G. Wang, B. Whiting, and K. T. Bae, "X-ray ct metal artifact reduction using wavelets: an application for imaging total hip prostheses," *IEEE Transactions on Medical Imaging*, vol. 19, no. 12, pp. 1238–1247, 2000.

[23] S. Zhao, K. T. Bae, B. Whiting, and G. Wang, "A wavelet method for metal artifact reduction with multiple metallic objects in the field of view," *Journal of X-ray Science and Technology*, vol. 10, no. 1, 2, pp. 67–76, 2002.

[24] M. Bal and L. Spies, "Metal artifact reduction in ct using tissue-class modeling and adaptive prefiltering," *Medical Physics*, vol. 33, no. 8, pp. 2852–2859, 2006.

[25] M. Bazalova, L. Beaulieu, S. Palefsky, and F. Verhaegen, "Correction of ct artifacts and its influence on monte carlo dose calculations," *Medical Physics*, vol. 34, no. 6Part1, pp. 2119–2132, 2007.

[26] A. Wong and J. Orchard, "A nonlocal-means approach to exemplar-based inpainting," in *2008 15th IEEE International Conference on Image Processing*. IEEE, 2008, pp. 2600–2603.

[27] D. Prell, Y. Kyriakou, M. Beister, and W. A. Kalender, "A novel forward projection-based metal artifact reduction method for flat-detector com-

puted tomography," *Physics in Medicine & Biology*, vol. 54, no. 21, p. 6575, 2009.

[28] W. J. Veldkamp, R. M. Joemai, A. J. van der Molen, and J. Geleijns, "Development and validation of segmentation and interpolation techniques in sinograms for metal artifact suppression in ct," *Medical Physics*, vol. 37, no. 2, pp. 620–628, 2010.

[29] C. Xu, F. Verhaegen, D. Laurendeau, S. A. Enger, and L. Beaulieu, "An algorithm for efficient metal artifact reductions in permanent seed implants," *Medical Physics*, vol. 38, no. 1, pp. 47–56, 2011.

[30] E. Meyer, R. Raupach, M. Lell, B. Schmidt, and M. Kachelrieß, "Frequency split metal artifact reduction (fsmar) in computed tomography," *Medical Physics*, vol. 39, no. 4, pp. 1904–1916, 2012.

[31] H. S. Park, J. K. Choi, K.-R. Park, K. S. Kim, S.-H. Lee, J. C. Ye, and J. K. Seo, "Metal artifact reduction in ct by identifying missing data hidden in metals," *Journal of X-ray Science and Technology*, vol. 21, no. 3, pp. 357–372, 2013.

[32] A. Mehranian, M. R. Ay, A. Rahmim, and H. Zaidi, "X-ray ct metal artifact reduction using wavelet domain L_0 sparse regularization," *IEEE Transactions on Medical Imaging*, vol. 32, no. 9, pp. 1707–1722, 2013.

[33] ——, "3d prior image constrained projection completion for x-ray ct metal artifact reduction," *IEEE Transactions on Nuclear Science*, vol. 60, no. 5, pp. 3318–3332, 2013.

[34] G. Wang, D. L. Snyder, J. A. O'Sullivan, and M. W. Vannier, "Iterative deblurring for ct metal artifact reduction," *IEEE Transactions on Medical Imaging*, vol. 15, no. 5, pp. 657–664, 1996.

[35] B. De Man, J. Nuyts, P. Dupont, G. Marchal, and P. Suetens, "Reduction of metal streak artifacts in x-ray computed tomography using a transmission maximum a posteriori algorithm," *IEEE Transactions on Nuclear Science*, vol. 47, no. 3, pp. 977–981, 2000.

[36] ——, "An iterative maximum-likelihood polychromatic algorithm for ct," *IEEE Transactions on Medical Imaging*, vol. 20, no. 10, pp. 999–1008, 2001.

[37] I. A. Elbakri and J. A. Fessler, "Statistical image reconstruction for polyenergetic x-ray computed tomography," *IEEE Transactions on Medical Imaging*, vol. 21, no. 2, pp. 89–99, 2002.

[38] C. Lemmens, D. Faul, and J. Nuyts, "Suppression of metal artifacts in ct using a reconstruction procedure that combines map and projection completion," *IEEE Transactions on Medical Imaging*, vol. 28, no. 2, pp. 250–260, 2009.

[39] J. Wang and L. Xing, "A binary image reconstruction technique for accurate determination of the shape and location of metal objects in x-ray computed tomography," *Journal of X-ray Science and Technology*, vol. 18, no. 4, pp. 403–414, 2010.

[40] F. E. Boas and D. Fleischmann, "Evaluation of two iterative techniques for reducing metal artifacts in computed tomography," *Radiology*, vol. 259, no. 3, pp. 894–902, 2011.

[41] M. Yazdi, M. A. Lari, G. Bernier, and L. Beaulieu, "An opposite view data replacement approach for reducing artifacts due to metallic dental objects," *Medical Physics*, vol. 38, no. 4, pp. 2275–2281, 2011.

[42] X. Zhang, J. Wang, and L. Xing, "Metal artifact reduction in x-ray computed tomography (ct) by constrained optimization," *Medical Physics*, vol. 38, no. 2, pp. 701–711, 2011.

[43] H. Zhang, L. Wang, L. Li, A. Cai, G. Hu, and B. Yan, "Iterative metal artifact reduction for x-ray computed tomography using unmatched projector/backprojector pairs," *Medical Physics*, vol. 43, no. 6Part1, pp. 3019–3033, 2016.

[44] S. Luo, H. Wu, Y. Sun, J. Li, G. Li, and N. Gu, "A fast beam hardening correction method incorporated in a filtered back-projection based map algorithm," *Physics in Medicine & Biology*, vol. 62, no. 5, p. 1810, 2017.

[45] Z. Chang, D. H. Ye, S. Srivastava, J.-B. Thibault, K. Sauer, and C. Bouman, "Prior-guided metal artifact reduction for iterative x-ray computed tomography," *IEEE Transactions on Medical Imaging*, vol. 38, no. 6, pp. 1532–1542, 2018.

[46] R. E. Alvarez and A. Macovski, "Energy-selective reconstructions in x-ray computerised tomography," *Physics in Medicine & Biology*, vol. 21, no. 5, p. 733, 1976.

[47] A. Coleman and M. Sinclair, "A beam-hardening correction using dual-energy computed tomography," *Physics in Medicine & Biology*, vol. 30, no. 11, p. 1251, 1985.

[48] E. Van de Casteele, D. Van Dyck, J. Sijbers, and E. Raman, "A model-based correction method for beam hardening artefacts in x-ray microtomography," *Journal of X-ray Science and Technology*, vol. 12, no. 1, pp. 43–57, 2004.

[49] L. Yu, J. A. Christner, S. Leng, J. Wang, J. G. Fletcher, and C. H. McCollough, "Virtual monochromatic imaging in dual-source dual-energy ct: radiation dose and image quality," *Medical Physics*, vol. 38, no. 12, pp. 6371–6379, 2011.

[50] L. Yu, S. Leng, and C. H. McCollough, "Dual-energy ct–based monochromatic imaging," *American Journal of Roentgenology*, vol. 199, no. 5_supplement, pp. S9–S15, 2012.

[51] H. Chen, Y. Zhang, M. K. Kalra, F. Lin, Y. Chen, P. Liao, J. Zhou, and G. Wang, "Low-dose ct with a residual encoder-decoder convolutional neural network," *IEEE Transactions on Medical Imaging*, vol. 36, no. 12, pp. 2524–2535, 2017.

[52] L. Gjesteby, Q. Yang, Y. Xi, Y. Zhou, J. Zhang, and G. Wang, "Deep learning methods to guide ct image reconstruction and reduce metal artifacts," in *Medical Imaging 2017: Physics of Medical Imaging*, vol. 10132. International Society for Optics and Photonics, 2017, p. 101322W.

[53] Y. Zhang and H. Yu, "Convolutional neural network based metal artifact reduction in x-ray computed tomography," *IEEE Transactions on Medical Imaging*, vol. 37, no. 6, pp. 1370–1381, 2018.

[54] C. Peng, B. Li, M. Li, H. Wang, Z. Zhao, B. Qiu, and D. Z. Chen, "An irregular metal trace inpainting network for x-ray ct metal artifact reduction," *Medical Physics*, 2020.

[55] X. Huang, J. Wang, F. Tang, T. Zhong, and Y. Zhang, "Metal artifact reduction on cervical ct images by deep residual learning," *Biomedical Engineering Online*, vol. 17, no. 1, p. 175, 2018.

[56] W.-A. Lin, H. Liao, C. Peng, X. Sun, J. Zhang, J. Luo, R. Chellappa, and S. K. Zhou, "Dudonet: Dual domain network for ct metal artifact reduction," in *Proceedings of the IEEE Conference on Computer Vision and Pattern Recognition*, 2019, pp. 10 512–10 521.

[57] L. Yu, Z. Zhang, X. Li, and L. Xing, "Deep sinogram completion with image prior for metal artifact reduction in ct images," *IEEE Transactions on Medical Imaging*, 2020.

[58] I. Goodfellow, J. Pouget-Abadie, M. Mirza, B. Xu, D. Warde-Farley, S. Ozair, A. Courville, and Y. Bengio, "Generative adversarial nets," *Advances in neural information processing systems*, vol. 27, pp. 2672–2680, 2014.

[59] Y. Taigman, A. Polyak, and L. Wolf, "Unsupervised cross-domain image generation," *arXiv preprint arXiv:1611.02200*, 2016.

[60] J.-Y. Zhu, T. Park, P. Isola, and A. A. Efros, "Unpaired image-to-image translation using cycle-consistent adversarial networks," in *Proceedings of the IEEE International Conference on Computer Vision*, 2017, pp. 2223–2232.

[61] X. Huang, M.-Y. Liu, S. Belongie, and J. Kautz, "Multimodal unsupervised image-to-image translation," in *Proceedings of the European Conference on Computer Vision (ECCV)*, 2018, pp. 172–189.

[62] J. Wang, Y. Zhao, J. H. Noble, and B. M. Dawant, "Conditional generative adversarial networks for metal artifact reduction in ct images of the ear," in *International Conference on Medical Image Computing and Computer-Assisted Intervention*. Springer, 2018, pp. 3–11.

[63] H.-Y. Lee, H.-Y. Tseng, J.-B. Huang, M. Singh, and M.-H. Yang, "Diverse image-to-image translation via disentangled representations," in *Proceedings of the European Conference on Computer Vision (ECCV)*, 2018, pp. 35–51.

[64] H. Liao, W.-A. Lin, S. K. Zhou, and J. Luo, "Adn: Artifact disentanglement network for unsupervised metal artifact reduction," *IEEE Transactions on Medical Imaging*, vol. 39, no. 3, pp. 634–643, 2019.

[65] M. Nakao, K. Imanishi, N. Ueda, Y. Imai, T. Kirita, and T. Matsuda, "Regularized three-dimensional generative adversarial nets for unsupervised metal artifact reduction in head and neck ct images," *IEEE Access*, vol. 8, pp. 109 453–109 465, 2020.

[66] C. Peng, B. Li, P. Liang, J. Zheng, Y. Zhang, Y. Zhang, B. Qiu, and D. Z. Chen, "A cross-domain metal trace restoring network for reducing x-ray ct metal artifacts," *IEEE Transactions on Medical Imaging*, 2020.

[67] J. Hsieh, R. C. Molthen, C. A. Dawson, and R. H. Johnson, "An iterative approach to the beam hardening correction in cone beam ct," *Medical Physics*, vol. 27, no. 1, pp. 23–29, 2000.

[68] C. H. Yan, R. T. Whalen, G. S. Beaupre, S. Y. Yen, and S. Napel, "Reconstruction algorithm for polychromatic ct imaging: application to beam hardening correction," *IEEE Transactions on Medical Imaging*, vol. 19, no. 1, pp. 1–11, 2000.

[69] Y. Kyriakou, E. Meyer, D. Prell, and M. Kachelrieß, "Empirical beam hardening correction (ebhc) for ct," *Medical Physics*, vol. 37, no. 10, pp. 5179–5187, 2010.

[70] J. M. Verburg and J. Seco, "Ct metal artifact reduction method correcting for beam hardening and missing projections," *Physics in Medicine & Biology*, vol. 57, no. 9, p. 2803, 2012.

[71] S. M. Lee, T. Bayaraa, H. Jeong, C. M. Hyun, and J. K. Seo, "A direct sinogram correction method to reduce metal-related beam-hardening in computed tomography," *IEEE Access*, vol. 7, pp. 128 828–128 836, 2019.

[72] P. P. Bruyant, "Analytic and iterative reconstruction algorithms in spect," *Journal of Nuclear Medicine*, vol. 43, no. 10, pp. 1343–1358, 2002.

[73] L. Feldkamp, L. Davis, and J. Kress, "Practical cone-beam algorithm," *Journal of the Optical Society of America A*, vol. 1, no. 6, pp. 612–619, 1984.

[74] J. Shen and T. F. Chan, "Mathematical models for local nontexture inpaintings," *SIAM Journal on Applied Mathematics*, vol. 62, no. 3, pp. 1019–1043, 2002.

[75] H. S. Park, S. M. Lee, H. P. Kim, J. K. Seo, and Y. E. Chung, "Ct sinogram-consistency learning for metal-induced beam hardening correction," *Medical Physics*, vol. 45, no. 12, pp. 5376–5384, 2018.

[76] O. Ronneberger, P. Fischer, and T. Brox, "U-net: Convolutional networks for biomedical image segmentation," in *International Conference on Medical Image Computing and Computer-Assisted Intervention.* Springer, 2015, pp. 234–241.

[77] L. Gjesteby, H. Shan, Q. Yang, Y. Xi, B. Claus, Y. Jin, B. De Man, and G. Wang, "Deep neural network for ct metal artifact reduction with a perceptual loss function," in *Proceedings of The Fifth International Conference on Image Formation in X-ray Computed Tomography*, vol. 1, 2018.

[78] P. Isola, J.-Y. Zhu, T. Zhou, and A. A. Efros, "Image-to-image translation with conditional adversarial networks," in *Proceedings of the IEEE Conference on Computer Vision and Pattern Recognition*, 2017, pp. 1125–1134.

[79] M. U. Ghani and W. C. Karl, "Fast enhanced ct metal artifact reduction using data domain deep learning," *IEEE Transactions on Computational Imaging*, vol. 6, pp. 181–193, 2019.

[80] H. Zhao, O. Gallo, I. Frosio, and J. Kautz, "Loss functions for image restoration with neural networks," *IEEE Transactions on Computational Imaging*, vol. 3, no. 1, pp. 47–57, 2016.

[81] M. A. Hegazy, M. H. Cho, M. H. Cho, and S. Y. Lee, "U-net based metal segmentation on projection domain for metal artifact reduction in dental ct," *Biomedical Engineering Letters*, vol. 9, no. 3, pp. 375–385, 2019.

[82] S. Karimi, P. Cosman, C. Wald, and H. Martz, "Segmentation of artifacts and anatomy in ct metal artifact reduction," *Medical Physics*, vol. 39, no. 10, pp. 5857–5868, 2012.

[83] H. Yu, K. Zeng, D. K. Bharkhada, G. Wang, M. T. Madsen, O. Saba, B. Policeni, M. A. Howard, and W. R. Smoker, "A segmentation-based method for metal artifact reduction," *Academic Radiology*, vol. 14, no. 4, pp. 495–504, 2007.

[84] J. Amanatides, A. Woo *et al.*, "A fast voxel traversal algorithm for ray tracing," in *Eurographics*, vol. 87, no. 3, 1987, pp. 3–10.

[85] R. L. Siddon, "Fast calculation of the exact radiological path for a three-dimensional ct array," *Medical Physics*, vol. 12, no. 2, pp. 252–255, 1985.

[86] H. Lee, B. P. Fahimian, and L. Xing, "Binary moving-blocker-based scatter correction in cone-beam computed tomography with width-truncated projections: proof of concept," *Physics in Medicine & Biology*, vol. 62, no. 6, p. 2176, 2017.

초록

빔경화는 다색 X선을 사용하고 에너지 의존적인 물질 감쇠 계수를 이용하는 CT 시스템의 특성상 불가피한 현상이며, 이는 특히 금속 영역을 포함하는 프로젝션 상의 값을 오측정하여 결과적으로 CT 영상에 허상물을 유발한다. 금속 허상물 저감화는 CT 영상에 존재하는 이러한 허상물을 제거하고 가려진 실제 정보를 복원하는 과정이다. 영상을 통한 진단과 방사선치료를 위한 계획 수립에 있어서 정확한 CT 영상을 획득하기 위해 금속 허상물의 제거는 필수적이다. 반복적인 재구성에 의한 수치적 방법에 기반을 둔 효과적인 금속 허상물 제거에 관한 최신 연구들이 발표되었으나 무거운 계산량으로 인해 임상 실습에 적용이 어려운 상황이다.

본 논문에서는 이러한 계산적인 이슈를 해결하기 위한 효율적인 빔 경화 추정 모델과 이를 이용한 금속 허상물 저감화 방법을 제안한다. 제안한 모델은 금속 물체의 기하정보와 다색 X선이 물체를 통과하면서 발생하는 빔경화의 물리적인 특성을 반영한다. 모델에 필요한 대부분의 매개변수들은 수치학적인 방법으로 교정 전의 CT 영상과 CT 시스템으로부터 추가적인 최적화 과정 없이 획득한다. 빔경화 허상물과 관련된 매개 변수 중 단 하나만 재구성 이후의 영상 단계에서 선형 최적화를 통해 탐색된다. 또한 제안한 방법으로 교정된 결과 영상에 잔존하는 허상물들을 제거하기 위한 추가적인 두가지 개선 방법을 제시한다.

다수의 시뮬레이션 데이터와 실제 데이터를 사용하여 정성적 및 정량적 비교를 통해 제안 기법의 유효성이 체계적으로 평가되었다. 제안 알고리즘은 정확성 및 견고성 측면에서 유의미한 결과를 보여주었고, 기존의 기법들에 비해 향상된 결과 영상의 품질 뿐만 아니라 임상적으로 적용할만한 빠른 수행 시간을 보여주었다. 이 연구는 CT 영상을 통한 진단과 방사능 치료의 계획 수립을 위한 정확성 향상에

유의미한 의미를 갖는다.

주요어: CT 재구성, 금속 허상물 제거, 빔 경화 현상, 다색 X선

학번: 2011-20957

Acknowledgements

관악에서의 15년 생활을 뒤돌아보며, 하나의 마침표이자 새로운 시작을 알리는 본 박사 학위 논문을 완성하는데 도움을 주신 모든 분들께 짧게나마 이 지면을 빌어 감사의 말씀을 전합니다.

가장 먼저 한 사람의 연구자이자 바른 인간으로 성장할 수 있게 지도해주신 신영길 교수님께 감사드립니다. 좋은 환경에서, 그리고 좋은 사람들과 함께 성장할 수 있었던 것은 저에게 너무나도 값진 경험이었습니다. 무엇보다 교수님의 끊임없는 열정을 곁에서 직접 볼 수 있었던 것은 저에게 더할 나위 없는 특권이었고, 그 모습을 본받아 앞으로도 더욱 정진하는 길을 걸어가도록 노력하겠습니다.

박사 학위 심사뿐만 아니라 학사, 석사, 박사 과정 동안 조언을 아낌없이 해 주신 김명수 교수님께 감사드립니다. 항상 에너지 넘치는 교수님의 모습에서 가끔씩 멈춰 있던 제 자신을 다시 움직이게 하는 원동력을 얻을 수 있었습니다. 부족했던 저의 논문을 냉철하게 판단해 주시어 보다 완성도 높은 결과를 만들 수 있게 도움을 주신 서진욱 교수님께 감사드립니다. 학위과정 내내 그리고 마지막 학위 심사까지 아낌없는 조언과 지도를 해 주신 이정진 교수님께도 감사드립니다.

저의 연구를 누구보다도 가까이서 도와 주시고 이끌어 주셨던 이호 교수님께 깊이 감사드립니다. 조금은 외로웠던 길을 걷고 있던 저에게 같은 연구 분야의 멘토로서, 그리고 선배님으로서 아낌없는 위로와 지원을 해 주셨습니다. 연구실

에 인턴으로 들어왔을 때부터 마지막까지 진심으로 아껴 주시고 지도해 주셨던 동준이 형께도 감사드립니다. 이제는 교수님으로서 새로운 출발을 하시게 된 걸 진심으로 축하 드립니다.

오랜 연구실 생활이 행복한 기억으로 남아있을 수 있는 건 모두 함께 했던 선후배님들 덕분이었습니다. 훌륭한 연구자이자 지도자의 귀감이 되어 주신 김보형 교수님, 누구보다 자신의 인생을 즐기시며 지금은 열정적인 리더의 모습을 보여주고 계시는 순형이 형, 반대로 누구보다 헌신적이시며 현실적인 조언을 아낌없이 해 주시던 오재 형, 순수하시면서도 언제나 겸손하셨던 호철이 형, 항상 유쾌하시고 마음이 잘 통하던 재형이 형, 자신과 가족 모두에게 충실하시며 행복하셨던 계현이 형, 수많은 대화를 통해 연구실에 적응하는데 큰 도움을 주셨던 성진이 형, 불타는 학구열과 자기 주도적인 삶을 보여주신 병훈이 형, 모든 주제에 능통하시며 저에게 인식의 경계를 넓혀 주신 성태 형, 열린 마음으로 항상 부족한 저를 보듬어 주시던 준혁 형, 제가 아는 중국인 중에 가장 열정이 넘치던 강호 형, 넘치는 재주만큼이나 겸손함이 가득하셨던 성철이 형, 냉철하게 연구실의 중심을 잡아 주셨던 현나 누나, 언제나 부드럽고 편안하게 대해 주시며 연구실의 대소사를 관리해주신 지혜Y 누나, 일과 삶의 균형을 철저하게 관리하시면서 그 무엇 하나에도 소홀하지 않으셨던 지혜K 누나, 생각이 누구보다도 깊고 멋진 미래를 준비하시던 세윤이 형, 조용하면서도 항상 완벽함을 추구하시는 모습이 인상적이셨던 형규 형, 묵묵히 주어진 일에 최선을 다 하시던 넓은 마음의 소유자 도현이 형, 항상 올바른 모습으로 모범을 보여주신 승환이 형, 같이 지낸 기간은 짧았지만 항상 따뜻한 모습으로 대해 주시던 영민이 형, 행복 에너지를 주변에 전파하시던 서현 누나, 모두 감사드립니다.

긴 대학원 과정 동안 고마웠던 분들이 너무도 많지만, 같이 했던 기간이 길고 또 최근일수록 아무래도 기억이 많이 남는 것 같습니다. 학부 동기이자 연구실 동기로서 많은 부분을 의지할 수 있었던 동갑내기 친구 영찬, 이제 곧 두 아이의

아빠가 되는 것을 축하하고 앞으로도 행복하길 바랍니다. 비상한 머리와 재주로 작가라는 새로운 길을 걸어가실 민규 형, 고생한 기간이 길었지만 그만큼 성숙해진 재훈, 두 분의 노력만큼 앞으로의 날들이 빛날 수 있기를 바랍니다. 한국어는 여전히 서툴지만 왠지 마음이 잘 통하던 지강이 형, 뚜렷한 자신의 가치관을 지키면서도 헌신적이셨던 지선 누나, 묵묵하시면서도 따뜻한 마음을 갖고 계셨던 동건이 형, 졸업 시기가 비슷한 동료로서 어디서나 항상 행복하시길 바랍니다. 지금은 잠시 학업을 미루고 새로운 꿈에 도전하는 용근, 석만, 좋은 결과가 있기를 진심으로 바랍니다. 넘치는 열정으로 힘차게 나아가는 민영, 성실한 만큼 예의도 바른 민경, 힘들어도 포기하지 않고 열심인 지완, 엉뚱하면서도 생각이 깊은 지오, 다양한 매력을 보유한 진규, 재능과 성실함을 두루 갖춘 민창, 앞으로의 모습이 많이 기대가 됩니다. 먼저 졸업하여 열심히 살아가고 있을 상수, 동준, 준동, 상희, 그리고 말년에 제가 연구실 외부 생활을 하게 되어 많은 도움을 주지 못했던 찬은, 현지, 강용, 주상, 상욱, 경휘, 모두에게 감사의 인사를 전합니다. 또한 같은 연구실은 아니었음에도 연구와 대학원 생활에 크게 도움을 주셨던 현주 형, 카일 형께도 깊이 감사를 드립니다.

누구보다 저의 미래를 걱정해주시고 지원해주신 부모님께 진심으로 감사드립니다. 두 분의 전폭적인 지원 아래 무사히 졸업까지 올 수 있었습니다. 또한 저의 졸업을 진심으로 응원해주신 장인어른과 장모님께도 깊은 감사의 말씀을 전합니다. 그리고 마지막으로 시작부터 함께하며 저에게 항상 큰 위로와 힘이 되어준 사랑하는 아내 근화에게 이 졸업의 영광을 바칩니다. 진심으로 고맙습니다.